

Modelling radio galaxies in the Millennium  
simulation: SKA/MeerKAT sources and CMB  
contaminants

Fidy Andriamanankasina Ramamonjisoa

A thesis submitted in partial fulfilment of the requirements for the degree

of

Magister Scientiae

in the Department of Physics, University of the Western Cape.



# Modelling radio galaxies in the Millennium simulation: SKA/MeerKAT sources and CMB contaminants

Fidy Andriamanankasina Ramamonjisoa

## Keywords

Active galactic nuclei

Cosmic microwave background

Semi-analytic model

N-body simulation

Radio luminosity function

Spectral energy distribution

Accretion efficiency

Radio mode accretion

Quasar mode accretion

Sunyaev-Zeldovich effect



## DECLARATION

I declare that *Modelling radio galaxies in the Millennium simulation: SKA/MeerKAT sources and CMB contaminants* is my own work, that it has not been submitted for any degree or examination in any other university, and that all the sources I have used or quoted have been indicated and acknowledged by complete references.

Fidy Andriamanankasina RAMAMONJISOA Date: 10 November 2009



## Abstract

### Modelling radio galaxies in the Millennium simulation: SKA/MeerKAT sources and CMB contaminants

F. A. Ramamonjisoa

MSc thesis, Department of Physics, University of the Western Cape.

We investigate the modelling of radio galaxies within a semi-analytic framework in the Millennium Simulation of the Virgo Consortium. The aim is to assess the radio sources contamination of Sunyaev-Zeldovich (SZ) signatures of clusters of galaxies in Cosmic Microwave Background (CMB) experiments. The modelling is also relevant to the Karoo Array Telescope (MeerKAT) and the Square Kilometre Array (SKA) science. The semi-analytical model consists of N-body simulation, the Millennium Run to trace the merger history of dark matter haloes within the  $\Lambda$  Cold Dark Matter ( $\Lambda$ CDM) cosmology and a follow up of the black hole accretion history and Active Galactic Nuclei (AGN) evolution. We study the growth of the supermassive black hole (SMBH) in galaxy centres and determine the black hole mass accretion conversion into radiation. We identify a model which matches observed radio luminosity function. We describe a model of observed sample of radio surveys at a given frequency and a flux density limit to obtain a model of radio luminosity function (space density of radio sources as a function of redshift) that we compare with our simulated data. We determine the redshift distribution of radio galaxies (FRI), blazars and radio quasars (FRII) in the simulation. We focus the modelling on flat spectrum population of blazars since their jets are collimated towards us and thus constitute the most potential contaminants of the CMB. We determine the spatial and density distribution of radio sources in clusters with a virial mass  $M_{\text{vir}} \geq 2 \times 10^{14} h^{-1} M_{\odot}$  and then compute the temperature fluctuations and fluxes produced by these cluster radio sources. Our main results include: the model provides a reasonable match within uncertainties with the model obtained by Dunlop & Peacock (1990) [39] using their best fit of radio luminosity function at redshift  $z \lesssim 0.3$ . The model underestimates the number of radio sources at high redshift  $z \gtrsim 1$ . Radio sources are concentrated around the centre of clusters with a maximum density at  $r \lesssim 0.1r_{200}$  where  $r_{200}$  is the radius within which the density is 200 times the

critical density. Radio sources are more concentrated in low mass clusters. The model predicts a surface density profile of radio sources with luminosity  $P \geq 10^{23} \text{ W.Hz}^{-1}$  at 1.4 GHz ( $z \lesssim 0.06$ ) in agreement with that of Lin & Mohr (2007) [58] at  $r \lesssim 0.1r_{200}$  but underestimates the density in the outskirts of the clusters. BL Lacs and FRI radio galaxies produce non negligible contamination at redshift  $z \lesssim 0.1$ . They produce a mean temperature fluctuation  $\sim 4.5 \mu\text{K}$  at redshift  $z \sim 0.01$  which can be at the same level as the kinetic SZE signal produced by the cluster. Blazars constitute potential contaminant of the thermal SZ effect at redshift  $z \sim 1.0$  and  $z \sim 1.5$  at 145 GHz where they produce a mean temperature  $300 \mu\text{K} - 350 \mu\text{K}$  for an average mass of the cluster.

November 2009



## Acknowledgements

I would like to express my gratitude to Prof. Catherine Cress who supervised this work. Her suggestions, guidance and comments are gratefully appreciated. I would like also to extend my thanks to Dr. Enrico Olivier who accepted to co-supervise this project. Special thanks are due to Prof. Patricia Whitelock and Prof. Peter Dunsby for their precious education and advice during the completion of our course work at the National Astrophysics and Space Science Programme (NASSP) at the University of Cape Town. I am very grateful to Dr Andreas Faltenbacher of the Max Planck institute for Astrophysics for his helpful assistance on the millennium database query. I would like to acknowledge the financial assistance from the South African Square Kilometre Array (SKA) project. I wish to acknowledge all people of the physics department of the University of the Western Cape (UWC) who facilitated our stay in the department. I wish to acknowledge Dr Kavilan Moodley and Dr Ilani Loubser who organised with Prof. Catherine Cress, Dr Andreas Faltenbacher and Dr Russell Johnston the journal club during our period of research at UWC. I acknowledge the South African Astronomical Observatory (SAAO) for providing us with computer facilities as a guest. I would like to extend my thanks to the Postdoctoral researchers, PhD students and all Msc students in our group for their collaboration in the discussion of our project. I acknowledge my family and friends for their support.

# Contents

<b>Title page</b>	<b>i</b>
<b>Keywords</b>	<b>ii</b>
<b>Declaration</b>	<b>iii</b>
<b>Abstract</b>	<b>iv</b>
<b>Acknowledgements</b>	<b>vi</b>
<b>Contents</b>	<b>vii</b>
<b>List of Figures</b>	<b>xi</b>
<b>List of Tables</b>	<b>xix</b>
<b>1 Introduction</b>	<b>1</b>
<b>2 Background</b>	<b>3</b>
2.1 Active galactic nuclei . . . . .	3
2.1.1 Introduction . . . . .	3
2.1.2 Radio-quiet AGN . . . . .	4
2.1.3 Radio-loud AGN . . . . .	6
2.1.4 Summary . . . . .	9



## CONTENTS

---

2.2	Unified model of AGN . . . . .	9
2.2.1	Introduction . . . . .	9
2.2.2	Radio-quiet AGN . . . . .	10
2.2.3	Radio-loud AGN . . . . .	10
2.2.4	Summary . . . . .	12
2.3	Mechanism of emission . . . . .	13
2.3.1	Synchrotron radiation . . . . .	15
2.3.2	Inverse Compton . . . . .	18
2.4	Cosmological background . . . . .	20
2.4.1	Luminosity distance . . . . .	22
2.5	Cosmic Microwave Background . . . . .	23
2.5.1	Introduction . . . . .	23
2.5.2	Sunyaev-Zeldovich effect . . . . .	24
2.5.3	Radio point source contamination . . . . .	31
2.5.4	Summary . . . . .	32
2.6	Millennium simulation . . . . .	32
2.6.1	Introduction . . . . .	32
2.6.2	Simulation description . . . . .	33
2.6.3	Haloes and merger tree construction . . . . .	34
2.6.4	Semi-analytic model of galaxy formation and evolution . . . . .	35
2.6.5	Millennium Database . . . . .	40
2.6.6	Summary . . . . .	41
2.7	AGN feedback . . . . .	42
2.7.1	Introduction . . . . .	42
2.7.2	Radio mode accretion . . . . .	42
2.7.3	Quasar mode accretion . . . . .	44



# CONTENTS

---

2.7.4	Accretion efficiency . . . . .	45
2.7.5	Summary . . . . .	49
<b>3</b>	<b>Methodology</b>	<b>51</b>
3.1	Introduction . . . . .	51
3.2	Modelling the radio mode accretion . . . . .	52
3.3	Modelling the quasar mode accretion . . . . .	54
3.4	Duty cycle and lifetime . . . . .	59
3.5	Estimation of the fraction of radio sources . . . . .	60
3.6	Spectral energy distribution . . . . .	64
3.7	Database query . . . . .	69
3.8	Redshift distribution . . . . .	72
3.9	Density profiles of radio galaxies in clusters . . . . .	74
3.10	Calculation of the temperature and fluxes of radio sources . . . . .	75
3.11	Summary . . . . .	77
<b>4</b>	<b>Results and Discussion</b>	<b>84</b>
4.1	Introduction . . . . .	84
4.2	Model of radio luminosity function . . . . .	84
4.2.1	Model RLF4 . . . . .	85
4.2.2	Model RLF5 . . . . .	87
4.3	Redshift distribution of radio galaxies and quasars . . . . .	89
4.4	Spatial distribution of radio sources . . . . .	92
4.5	Radial distribution of radio sources in clusters . . . . .	97
4.6	Temperature fluctuations and fluxes . . . . .	102
<b>5</b>	<b>Conclusion</b>	<b>107</b>



## CONTENTS

---

<b>Bibliography</b>	<b>110</b>
<b>Appendices</b>	<b>121</b>
<b>A Spectral distribution of the scattered CMB</b>	<b>121</b>
<b>B Table of temperature fluctuations and fluxes of radio sources</b>	<b>123</b>



# List of Figures

2.1	Structure of a radio galaxy. From the compact core of the radio galaxy extends away a long thin jets. Hot spots are located at the ends of the lobes. The lobes are believed to be powered by beams of high energy particles and magnetic field and the jets are the visible manifestations of the beams. The hot spots are the results of the shock of the supersonic jet when they terminate at the end of the lobes (Credit: Conway and Blanco (1994)). . . . .	7
2.2	Fanaroff-Riley I type galaxies. The left and right panels show respectively the radio structure of the FRI radio galaxy 3C 296 and the VLA map of the FRI galaxy 3C 449 (Credit: Perley, Willis and Scott (1979)). . . . .	7
2.3	Fanaroff-Riley II type galaxies. The left and right panels show respectively the radio structure of the FR II radio galaxy (Cygnus A) and the VLA map of the FR II galaxy 3C 47 (Credit: Bridle et al. (1994)). . . . .	8
2.4	Unified model of AGN. Radio galaxies and Seyfert 2 are viewed at an angle $\sim 90^\circ$ from the jet. Quasars and Seyfert 1 are viewed at an angle to the jet and blazars are viewed at an angle looking down the jet. Seyfert 1 and Seyfert 2 are RQQ and radio galaxies, quasars and blazars are RLQ (source: <a href="http://www.whatsnextnetwork.com/technology/media/active_galactic_nuclei.jpg">http : //www.whatsnextnetwork.com/technology/media/active_galactic_nuclei.jpg</a> ). . . . .	12

## LIST OF FIGURES

---

- 2.5 SZ effect in clusters. The ICM of clusters contain hot electron gas of temperature  $T \sim 10^8$  K. The scattering of the CMB photons by hot gas results in the transfer of low energy photons to higher energies causing a distortion of the CMB black body spectrum. The three frequencies shown are the Atacama Cosmology Telescope (ACT) observation frequencies. No deviation is observed at the central frequency 220 GHz (a precise calculation gives a frequency  $\sim 218$  GHz) (Credit: Verde and Spergel (2002)). . . . . 25
- 2.6 Distortion of the CMB blackbody spectrum by inverse Compton scattering. The dashed line is the initial spectrum of the background radiation and the solid line is the distorted spectrum after scattering. The intensity of radiation decreases at radio wavelengths and increases at millimetre wavelengths. There is a 'null' frequency where the spectrum shows no distortion (218 GHz). This is the characteristic spectral SZ signature of galaxy clusters. The distortion shown is for a fictional cluster thousand times more massive than a typical massive cluster (adopted from Carlstrom et al. (2002) [22]). . . . . 25
- 2.7 Distortion of the CMB blackbody spectrum. The solid line is the thermal SZE and the dashed line is the kinetic SZE. The left panel shows the intensity and the right panel the temperature brightness in the Rayleigh Jeans region of the spectrum. The SZ signature corresponds to a cluster with an electron temperature of 10 keV, a Comptonization parameter  $y = 10^{-4}$  and a peculiar velocity of  $500 \text{ km.s}^{-1}$  (adopted from Carlstrom et al. (2002) [22]). . . . . 28
- 2.8 Spectral dependence of the SZE. The  $y$  axis is the intensity change  $\Delta I$  in CMB.  $g(x)$  is the spectral dependence for the non relativistic thermal SZE and  $h(x)$  the spectral dependence for the kinetic SZE (adopted from Rephaeli (1995) [90]). . . . . 30
- 2.9 Organization of the merger tree in the Millenium Run (source: <http://www.gvo.org/MyMillennium/pages/help/HelpSingleHTML.jsp#simulation>). . . . . 36

## LIST OF FIGURES

---

2.10	The left panel shows the galaxy formation and evolution in semi-analytical models. The right panel shows the population of simulated galaxies superposed on dark-matter particles (grey-coloured) in a region of $21 \times 21 \times 8$ (Mpc. $h^{-1}$ ) <sup>3</sup> . The galaxies are represented with coloured circles which are coded in accordance with their star formation rate that increases from the sequence red, yellow, green and blue. At early times (top panel $z = 3$ ) stars are forming with only few galaxies. Later on, from $z = 3$ to $z = 0$ , more galaxies form with new stars but at the same time some of them run out of gas and they turn green, yellow and red. At the present time ( $z = 0$ ), we can see that red galaxies associated with old stars are found in the central region of the cluster and blue galaxies with blue young stars populate the outskirts of the system. This is very similar to the observations (credit: Colberg J. and Diaferio A., source: <a href="http://www.mpa-garching.mpg.de/GIF/#ref">http://www.mpa-garching.mpg.de/GIF/#ref</a> ). . . . .	40
2.11	The black hole accretion rate density $\dot{m}_{\text{BH}}$ as a function of redshift $z$ . The solid line represents the quasar mode accretion which is more efficient at late time (high redshift): it falls down rapidly for $z \leq 2$ . The dashed line is the radio mode accretion which is more efficient at low redshifts whereas its contribution to the overall black hole mass is not very significant. The quasar mode accretion is more efficient than the radio mode accretion at all times (adopted from Croton et al. (2005) [32]). . . . .	46
2.12	Radiation efficiency as a function of redshift for three quasars sample $S_1$ , $S_2$ and $S_3$ from SDSS DR1. The error bars are dominated by the uncertainty in black hole masses (adopted from Wang et al. (2006) [119]). . . . .	49
3.1	Flow chart of the model for computing the space densities of radio sources in radio mode accretion and quasar mode accretion. . . . .	58

## LIST OF FIGURES

---

- 3.2 Number density against redshift at two luminosities  $P_{2.7 \text{ GHz}} = 10^{27} \text{ WHz}^{-1}\text{sr}^{-1}$  (top panels) and  $P_{2.7 \text{ GHz}} = 10^{26} \text{ WHz}^{-1}\text{sr}^{-1}$  (bottom panels) for flat spectrum and steep spectrum radio sources. The figures show the limits to the number density allowed by the new model RLFs (mean-z data for left panels) and the new model RLFs (high-z data for right panels). We can see that there is (in average) about 10 times more steep spectrum than flat spectrum radio sources at least up to redshift  $z = 2$ .  $\Omega_o = 1$  is the matter density in De Sitter cosmology (adopted from Dunlop and Peacock (1990) [39]). . . . . 61
- 3.3 Simulations of major mergers. Each panel is  $80h^{-1}$  Mpc on a side and the time evolution is shown in the upper left corner. The blue colour corresponds to baryonic gas fraction of 20% and the red colour less than 5%. The black hole is seen as an optically bright QSO at the time  $T = 1.03$  Gyr (systems ongoing merging), 1.39 Gyr and 1.48 Gyr. The nuclear point sources shown in the figure during these three period of times represent the relative luminosities of stars and quasars (adopted from Hopkins et al. (2005) [48]). . . . . 63
- 3.4 Spectral energy distribution of radio galaxies and blazars. 3C 338 FRI radio galaxy (top left panel). BL Lacs HBL Mkn 501 (top right). Blazar Swift J1656.3-3302 (bottom left). The bottom right panel shows the average SEDs of a blazar sample binned with radio luminosity. The dashed curves are analytic approximations of the radio spectrum. They are obtained by assuming that the ratio of the two peak frequencies is constant and that the luminosity of the second peak is proportional to the radio luminosity. . . . . 65
- 3.5 The figure shows, respectively, the SEDs of the low redshift ( $z = 0.034$ ) BL Lac Mkn 501 HBL (top left panel), FRI 3C 338 ( $z = 0.0304$ ) (top right panel), mean SED of blazars (bottom left panel) and FR II (0438-435) (bottom right panel). The green solid lines are parabolic (spline cubic) fits to the low power BL Lac and FRI (high power blazar and FR II) spectrum. . . . . 66

## LIST OF FIGURES

---

3.6	Flow charts for the determination of the centres of the clusters (top panel) and the virial masses of clusters with their centre and the radio sources coordinates (bottom panel). . . . .	79
3.7	Flow chart of the programme for the calculation of the surface density of radio sources as a function of the ratios of the radial distance $r$ from the centre of the cluster to $r_{200}$ . . . . .	80
3.8	Flow chart for the calculation of the temperature fluctuations and fluxes due to radio sources in clusters. . . . .	81
3.9	Flow chart for the calculation of the virial mass of each cluster and the sum of the temperature and corresponding fluxes due to the radio sources in that cluster. . . . .	82
3.10	Flow chart for the calculation of the average temperature fluctuations and fluxes of the clusters and deviation from the mean. . . . .	83
4.1	Model of radio luminosity functions of Dunlop and Peacock (1990) [39]. The model shows the space density of flat spectrum radio galaxies and quasars as a function of redshift with flux density limit 1 mJy at 2.7 GHz. The solid red line is the model RLF5 high-z data that we use for comparison in the present work. . . . .	89
4.2	Redshift distribution of blazars of different luminosities at 2.7 GHz for a flux cut-off 1 mJy normalized at $z = 0.41$ . The model corresponding to the SED of high luminosity blazars is shown in blue steps and the model of Dunlop and Peacock (1990) [39] derived from RLF5 is displayed in red. The steps in cyan correspond to the SED of the high redshift blazar Swift J1656.3-3302 at $z \simeq 2.40$ . The green steps show the redshift distribution for the mean SED of blazars adopted in Fossati et al. (1998) [43]. . . . .	92

## LIST OF FIGURES

---

- 4.3 Spatial distribution of BL Lacs and FRI at different redshift. The left panels are the 3D distributions and the right panels are the corresponding 2D projections. BL Lacs objects are shown as red circles and FRI radio galaxies as green dots. . . . . 94
- 4.4 Spatial distribution of blazars and FRII at different redshift. The left panels are the 3D distributions and the right panels are the corresponding 2D projections. Blazars are shown as red circles and FRII radio galaxies as green dots. . . . . 95
- 4.5 Distribution of the black hole mass accretion at different redshift respectively for flat spectrum radio sources BL Lacs, blazars (left panels) and steep spectrum radio sources FRI, FRII (right panels). The rows correspond respectively to redshifts  $z = 0.01, 0.10, 1.03, 1.44$ .  $\Delta M$  ( $10^{10}h^{-1}M_{\odot}$ ) is the difference between the descendant black hole mass and the progenitor black hole mass in the timestep of the simulation. The distribution of the black hole mass accretion for FRI and FRII can be approximated by a gaussian. . . . . 96
- 4.6 Surface density profiles of radio sources and galaxies in clusters. The upper limit of clusters redshift is  $z = 0.0647$  and the lower limit of radio sources luminosity at 1.4 GHz is  $P_{\min} = 10^{23} \text{ WHz}^{-1}$ . In the left panel is shown the model of Lin and Mohr (2007) [58]. The blue solid points are the radio sources and the green hollow points are galaxies more luminous than  $M_K = -24$ . The red solid line corresponds to the best-fit total profile that includes the cluster and background. The best-fit cluster model is shown as a cyan short dashed line. The cyan dotted line is the best-fit model for the galaxies (green) total profile and the cyan long dashed line is the best-fit model for the cluster profiles. The right panel shows the surface density profile of BL Lacs modelled using the Mkn 501 template SED in red line and FRI in green line. The total surface density profile of BL Lacs and FRI radio galaxies is shown in blue line. . . . . 98



## LIST OF FIGURES

---

- 4.7 Total surface density profiles of BL Lacs and FRI radio galaxies with a flux limit  $S = 10$  mJy at 1.4 GHz. Each panel corresponds to clusters with virial radius  $R_{\text{vir}} = 1.5, 1.8, 2.1, 2.4, 2.7, 3.0$  Mpc and the profiles are shown at redshift  $z = 0.05, 0.10, 0.19, 0.30$ . The density of radio sources in clusters observed above a given flux cut-off (10 mJy), is much lower at higher redshift and they are concentrated close to the centre of the cluster at  $r \lesssim 0.1r_{200}$ . . . . . 100
- 4.8 Total surface density profiles of BL Lacs and FRI radio galaxies with a flux limit  $S = 10$  mJy at 1.4 GHz. Each panel shows the effect of the virial radius scaling at respectively redshift  $z = 0.05, 0.10, 0.19, 0.30$ . . . . . 101
- 4.9 Surface density profiles of BL Lacs and FRI radio galaxies with a flux limit  $S = 10$  mJy at 1.4 GHz for different virial mass bins of cluster radio sources  $2 \times 10^{14} h^{-1} M_{\odot} < M_{\text{vir}} < 6 \times 10^{14} h^{-1} M_{\odot}$ ,  $6 \times 10^{14} h^{-1} M_{\odot} < M_{\text{vir}} < 10^{15} h^{-1} M_{\odot}$ , and  $M_{\text{vir}} > 10^{15} h^{-1} M_{\odot}$ . Each panel corresponds respectively to the density profiles at redshift  $z = 0.05, 0.10, 0.19, 0.30$  scaled to the mean virial radius  $r_{\text{vir}} = 2.1$  Mpc ( $r_{200} \simeq 1.5$  Mpc) of the clusters in the corresponding snapshot. 102
- 4.10 Average temperatures (left panels) and fluxes (right panels) as a function of redshift for different cluster virial mass bins at respectively from top to bottom panels 145 GHz, 220 GHz and 270 GHz. The temperature fluctuations and fluxes of high luminosity blazars are shown for the redshift  $z = 0.79$  and  $z = 1.03$  where quasar mode accretion is more effective (red squares are for  $2 \times 10^{14} h^{-1} M_{\odot} < M_{\text{vir}} < 6 \times 10^{14} h^{-1} M_{\odot}$  and magenta circles are for  $6 \times 10^{14} h^{-1} M_{\odot} < M_{\text{vir}} < 10^{15} h^{-1} M_{\odot}$ ). Blue, cyan and green circles and squares are the temperature fluctuations and fluxes of low luminosity blazars (BL Lacs) that undergo radio mode accretion. Beyond  $z = 1.03$  the model underestimates the temperature and flux distributions. The errorbars are the deviations from the average temperatures and fluxes of clusters in each mass bin. . . . . 104

**LIST OF FIGURES**

---

4.11 Average temperatures (left panels) and fluxes (right panels) as a function of the redshift for cluster virial mass bins respectively from top to bottom panels  $2 \times 10^{14} h^{-1} M_{\odot} < M_{\text{vir}} < 6 \times 10^{14} h^{-1} M_{\odot}$ ,  $6 \times 10^{14} h^{-1} M_{\odot} < M_{\text{vir}} < 10^{15} h^{-1} M_{\odot}$  and  $M_{\text{vir}} > 10^{15} h^{-1} M_{\odot}$  at 145 GHz, 220 GHz and 270 GHz. For a given cluster virial mass bin the temperature fluctuations are increasing with the frequency. The deviations from the mean are smaller for the most massive clusters. The squares and circles with no dashed-lines in the top right corner of each plot are the distributions corresponding to high luminosity blazars triggered by quasar mode accretion. They are rare in massive clusters and at high redshift. . . . . 105



# List of Tables

2.1	Classification of the spectrum of radio sources according to the spectral index $\alpha$ . . . . .	18
2.2	Cosmological parameters used in the Millennium Run. . . . .	33
2.3	Information used from the table Snapshots. . . . .	41
2.4	Information used from the table DeLucia2006a. . . . .	41
2.5	Recent estimates of the radiative efficiency $\eta$ . . . . .	49
3.1	Spectral energy distribution of the low power FRI 3C 338 ( $z = 0.0304$ ). . . .	66
3.2	Spectral energy distribution of the low luminosity BL Lacs Mkn 501 HBL ( $z = 0.034$ ). . . . .	67
3.3	Spectral energy distribution of the high redshift blazar ( $z = 2.4$ ) Swift J1656.3-3302. . . . .	67
3.4	Average SED of blazars binned in radio luminosity. . . . .	68
3.5	Spectral energy distribution of the high redshift FR II radio galaxies ( $z = 2.85$ ). . . . .	68
4.1	Space densities of the model RLF4 MEAN- $z$ as a function of the redshift $z$ . . .	86
4.2	Space densities of the model RLF4 HIGH- $z$ as a function of the redshift $z$ . . .	87
4.3	Space densities of the model RLF5 MEAN- $z$ as a function of the redshift $z$ . . .	88
4.4	Space densities of the model RLF5 HIGH- $z$ as a function of the redshift $z$ . . .	89
4.5	Space density of blazars at 2.7 GHz with a flux density limit 1 mJy obtained from our model in the Millennium simulation $\Lambda$ CDM cosmology. . . . .	90

## LIST OF TABLES

---

4.6	Redshift distribution of blazars at 2.7 GHz with a flux density limit 1 mJy obtained from our model. We assume an average SED of HBL Mkn 501 in radio mode accretion and the mean SED of high luminosity blazars from Sparke and Gallagher (2007) [96] for quasar mode accretion. . . . .	91
4.7	Redshift distribution of blazars at 2.7 GHz with a flux density limit 1 mJy obtained from the model RLF5 high-z data of Dunlop and Peacock (1990) [39].	91
4.8	Temperature fluctuations and fluxes caused by BL Lacs low luminosity blazars at redshift $z = 0.48$ at 145 GHz, 220 GHz and 270 GHz. The clusters virial masses considered here are for clusters with $M_{\text{vir}} \geq 2 \times 10^{14} h^{-1} M_{\odot}$ and with radio sources temperature fluctuations at least $0.1 \mu\text{K}$ . . . . .	106
4.9	Temperature fluctuations and fluxes caused by blazars at redshift $z = 1.44$ at 145 GHz, 220 GHz and 270 GHz. The clusters virial masses shown here are for clusters with $M_{\text{vir}} \geq 2 \times 10^{14} h^{-1} M_{\odot}$ and with radio sources temperature fluctuations at least $0.1 \mu\text{K}$ . . . . .	106
B.1	Temperature fluctuations and fluxes caused by BL Lacs low luminosity blazars at redshift $z = 0.10$ at 145 GHz, 220 GHz and 270 GHz. The clusters virial masses shown here are for $M_{\text{vir}} \geq 2 \times 10^{14} h^{-1} M_{\odot}$ and with radio sources temperature fluctuations greater than $0.1 \mu\text{K}$ . . . . .	123

# Chapter 1

## Introduction

In August 1931 Jansky first discovered radio emission from the Milky Way. He found that the signal was stronger in the direction of the constellation of Sagittarius where the centre of our Galaxy lies. He published his results in 1933 (Jansky (1933) [51]). Twelve years later Reber detected one of the brightest Galactic radio sources in the constellation Cygnus (Cygnus A) (Reber (1949) [88]). Initially, it was not possible to locate the radio emission precisely using telescope but in 1949, Bolton, Stanley and Slee used interferometer to identify Virgo A and Centaurus A and established the extragalactic origin of these radio emissions (Bolton et al. (1949) [15]). Since then radio astronomers have detected hundreds of thousands of radio galaxies. Depending on the morphology, structure, orientation, beaming and luminosity of the emission radio sources can be classified differently.

Another area of research that was initiated using radio telescopes is that of the Cosmic Microwave Background (CMB). This light from the early universe was discovered in 1964 by Penzias and Wilson. One year after the publication of the paper by Penzias & Wilson (1965) [85], Howell & Shakeshaft (1966) [49] measured the temperature of the CMB at a wavelength of 20.7 cm and found the value  $2.8 \pm 0.6$  K. In the same year Roll & Wilkinson (1966) [92] found a temperature  $3.0 \pm 0.5$  K in the wavelength range 3.2 cm and Field & Hitchcock (1966) [42] found a temperature  $3.2 \pm 0.5$  K at a wavelength 0.264 cm. Since then about sixty experiments have been carried out to measure the CMB temperature. A

## Introduction

---

complete list of the CMB temperature measurements can be found in Nordberg & Smoot (1998) [74]. The first high precision CMB fluctuation measurement was carried out in late November 1989 after the launch of the satellite COsmic Background Explorer (COBE) (Bennett et al. (1992) [6], Smoot et al. (1992) [101], Wright et al. (1992) [127]). CMB is observed in all directions of the sky and was emitted about 400 000 years after the Big Bang. An anisotropy at a level of a part in 100,000 was found. The next mission was the Wilkinson Microwave Anisotropy Probe (WMAP) (e.g. Page (2000) [79]). It was designed to determine the geometry, content, and evolution of the universe via a 13 arcminute Full Width at Half Maximum (FWHM) resolution full sky map of the CMB temperature anisotropy. The fits to the WMAP power spectrum have constrained cosmological parameters like the density parameter in baryons  $\Omega_b$ , the density parameter in matter  $\Omega_m$  and the total density parameter  $\Omega_{\text{total}}$  with good accuracy. The Planck Surveyor satellite (Planck Collaboration (2006) [87]) was launched recently (14th of May 2009) and have observed over the range 30-800 GHz and have a resolution of 4 arcminutes (see <http://www.rssd.esa.int/Planck> for details). To obtain even higher resolution data on CMB fluctuations ( $\sim 1$  arcminute) the Atacama Cosmology Telescope (ACT) (Kosowsky (2004) [55]) has been built. It is a 6m telescope located in the Atacama desert in the north of Chile. It is designed to make a precise measurement of the CMB spectrum on angular scales of a degree down to an arcminute.

At high resolution ( $\sim 1$  arcminute) galaxy clusters leave an imprint in the CMB via the so called “Sunyaev Zeldovich effect” (Sunyaev & Zeldovich (1970) [110], Sunyaev & Zeldovich (1972) [111]) and this imprint can be used to detect clusters. However radio point sources (Sehgal et al. (2009) [97]) are contaminants of the signal from the cosmic microwave background that make the detection of the imprint difficult. Our goal here is to determine the spatial and flux distribution of radio sources in galaxy clusters using galaxies extracted from the Millennium simulation since they are CMB contaminants.

We provide the theoretical backgrounds needed in the project in Chapter 2. Then we describe the methodology in Chapter 3 and in Chapter 4 we present the results with the discussions.

# Chapter 2

## Background

In this chapter we give a brief overview of the background information needed for this project. The first two sections deal with active galactic nuclei and the unification model. We present also the classification of radio sources and the processes of radio emission. Then we describe the features in CMB and present the SZ effect in galaxy clusters and CMB experiments. The next section describes the Millennium simulation and the last section of the chapter is talking about AGN feedback in simulations.

### 2.1 Active galactic nuclei

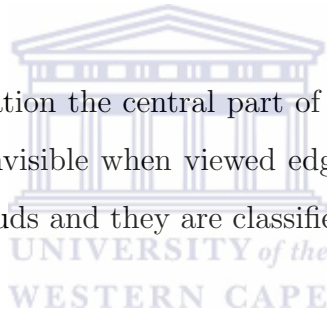
#### 2.1.1 Introduction

Active Galactic Nuclei (AGN) are extragalactic sources which can be found in the local universe and at cosmological distances. They were more abundant in the earlier universe. They are associated with the nuclei of galaxies and their emission which is often highly anisotropic, is dominated by non-stellar and non-thermal processes (Padovani (2007)[77]). AGN are very luminous in some or all wavelengths of the electromagnetic spectrum. The most important of them for our modelling is those brighter in radio wavebands. Since they are more luminous than normal galaxies they can be used to probe distant objects. Their evolution as a function of time that we know from the redshift of their spectra provides

valuable tools for constraining cosmological models. The AGN central engine is powered by a supermassive black hole which is believed to be hosted by almost all, if not all galaxies. The central black hole accretes matter from the surrounding accretion disk containing fast-moving clouds. Line emission from these clouds is broadened significantly due to the high velocities associated with orbits in a deep potential well. Clouds further from the centre emit narrower lines through the Doppler effect. The lines of broad and narrow line clouds are broadened by Doppler effect but the width depends only on the velocities. There are two types of AGN: 'Type 1' AGN and 'Type 2' AGN which can be described as follows.

**'Type 1' AGN** The emitting object is classified as 'Type 1' AGN when we can see the near-infrared to soft-X ray continuum and broad-lines. The spectrum of the accretion disk peaks around the optical-UV band.

**'Type 2' AGN** In some configuration the central part of the AGN could be obscured by absorbing material so that it is invisible when viewed edge-on. In that case we can see only the narrow-lines emitted by clouds and they are classified as 'Type 2' AGN.



We can divide AGN into radio-quiet AGN and radio-loud AGN. The radio-loud AGN are characterised by their strong radio emission while radio-quiet AGN are faint in the radio.

### 2.1.2 Radio-quiet AGN

They constitute the large majority of AGN. They have very weak radio emission which is about 1000 times fainter than in radio-loud sources. We can classify radio-quiet AGN as follows.

**Low-ionization nuclear emission line regions (LINERs)** They show emission lines from weakly ionized atoms and neutral atoms ( $O^+$ ,  $N^+$ ,  $S^+$  and  $O$ ) but the nuclear emission line from strongly ionized atoms ( $O^{++}$ ,  $Ne^{++}$  and  $He^+$ ) is very weak (Heckman (1980) [46]). We can neglect their contribution as potential AGN contaminants of the CMB since they are the



least luminous class of AGN.

*Host galaxy:* spiral galaxies and starburst galaxies.

**Ultra-luminous infrared galaxies (ULIRGs)** ULIRGs are starbursts galaxies that emit most of their light in infrared ( $L_{\text{IR}} > 10^{12}L_{\odot}$ ). It is not well known if their UV emission is only processed by star formation but at some stage of their evolution AGN may manifest as ULIRGs. They are undergoing mergers as the star formation in this starburst is triggered by major mergers. Most ULIRGs are observed at high redshift  $z > 1$  and there are few locally.

*Host galaxy:* starbursts galaxies.

**Seyfert galaxies** This type of AGN shows a spectral line emission from highly ionized gas (Sparke & Gallagher (2007) [96]). They are classified as Seyfert 1 galaxies and Seyfert 2 galaxies depending on the nature of the emission line.

- Seyfert 1 galaxies

They can show both narrow and broad emission lines. The broad component of the emission line is relatively strong and they are likely to exhibit strong soft X-ray emission.

*Host galaxy:* spiral galaxies.

- Seyfert 2 galaxies

They show narrow line emission whereas the broad component is obscured by dust or by our viewing angle with respect to the galaxy.

*Host galaxy:* spiral galaxies.

As Seyfert galaxy emission in the radio is very weak they do not constitute a potential AGN contaminant to the CMB.

**Radio-quiet quasars** They have the same characteristics as Seyfert 1 galaxies but they are more luminous and exhibit strong continuum emission line in optical and X-ray regions of the spectrum and also narrow and broad optical emission lines. This type of AGN is also

referred to as a Quasi-Stellar Object (QSO) to distinguish it from radio-loud quasars which have stronger radio emission.

### 2.1.3 Radio-loud AGN

This type of AGNs shows strong and extended radio emission. Their nucleus is also optically very bright. They are classified as follows.

**Radio galaxies** Radio images of these radio sources show a very compact component which represents an active galactic nucleus that is thought to power the central engine. Thin jets extend from the central core of the galaxy and they end at hot spots (Figure (2.1)). The lobes are seen as a large scale structure nearly symmetric placed on either side of the nucleus. The surface brightness within a lobe of a radio galaxy peaks at a well defined hot spot. Radio galaxies can show broad and narrow emission lines or narrow emission lines only. Broad-line radio galaxies (BLRG) have very broad H and He features with velocities up to 25 000 km.s<sup>-1</sup> that may include narrow emission lines. Narrow-line radio galaxies (NLRG) include forbidden lines of O, N, S, Fe and Balmer lines of He. They have line widths of the order of 1000 km.s<sup>-1</sup>. We can divide radio galaxies into FRI (Fanaroff-Riley class I) and FRII (Fanaroff-Riley class II) on the basis of the relative location of the hot spots.

- FRI objects

The distance between the hot spots of FRI sources is less than half of the largest size of the source and the power of the source at 1.4 GHz is less than 10<sup>24.5</sup> W.Hz<sup>-1</sup>. FRI type radio galaxies are relatively low power radio sources. They are brightened toward the centre and a jet can be seen on both sides of the nucleus (Figure (2.2)).

- FRII objects

The distance between the hot spots of FRII sources is more than half the largest size of the source and the power of the source at 1.4 GHz is greater than 10<sup>24.5</sup> W.Hz<sup>-1</sup>.

FRII type radio galaxies are more powerful sources of radio emission. They are edge-brightened (the outer part of the lobes are relatively bright). The jet is weak compared

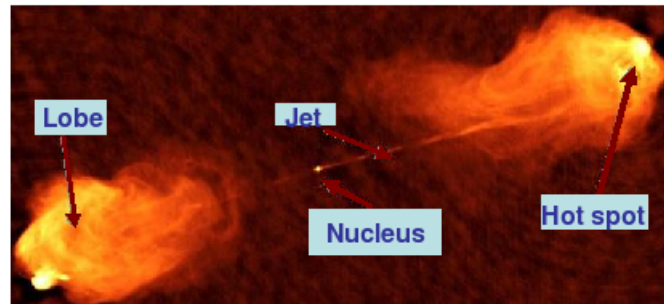


**Figure 2.1:** Structure of a radio galaxy. From the compact core of the radio galaxy extends away a long thin jets. Hot spots are located at the ends of the lobes. The lobes are believed to be powered by beams of high energy particles and magnetic field and the jets are the visible manifestations of the beams. The hot spots are the results of the shock of the supersonic jet when they terminate at the end of the lobes (Credit: Conway and Blanco (1994)).

to the lobes (Figure (2.3)).

Host galaxy: elliptical galaxies.

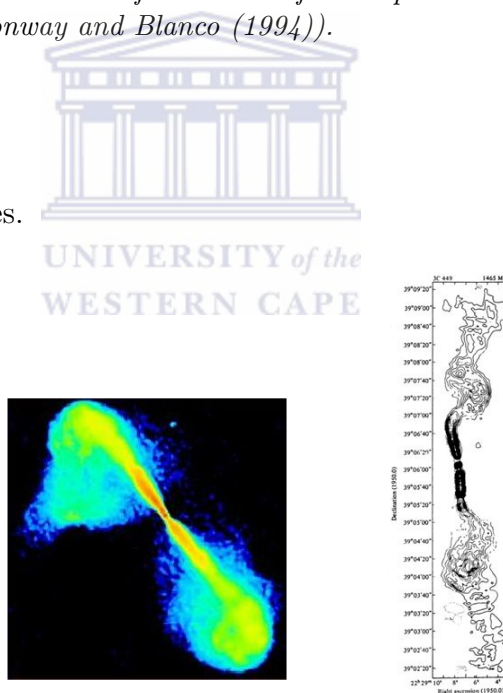


**Figure 2.2:** Fanaroff-Riley I type galaxies. The left and right panels show respectively the radio structure of the FRI radio galaxy 3C 296 and the VLA map of the FRI galaxy 3C 449 (Credit: Perley, Willis and Scott (1979)).

**Blazars** Blazars are the most luminous objects in the universe. Their emission is not regular and shows a rapid variability and high polarization. They exhibit apparent superluminal

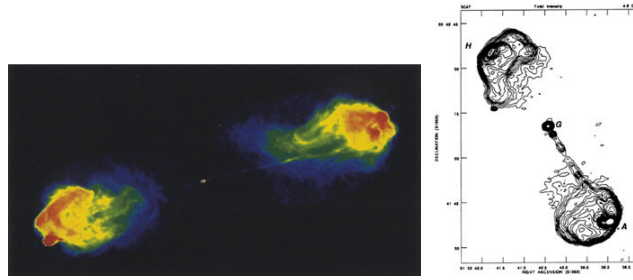


**Figure 2.3:** Fanaroff-Riley II type galaxies. The left and right panels show respectively the radio structure of the FR II radio galaxy (Cygnus A) and the VLA map of the FR II galaxy 3C 47 (Credit: Bridle et al. (1994)).

motion and a broad non thermal continuum which extends from the radio up to  $\gamma$ -rays (Urry & Padovani (1995) [116]). There are two classes of blazars: BL Lacertae (BL Lacs) objects and Optically Violent Variable (OVV) quasars.

- BL Lacs

They are considered to be low power radio galaxies similar to FRI but with jets close to our line of sight. They are almost devoid of emission lines and they are characterized by rapid variability and strong optical polarization. The spectral energy distribution of blazars shows two peaks: one at lower frequencies due to synchrotron emission and one at higher frequencies (higher energies) due to inverse Compton emission. BL Lac objects are divided into low-energy peaked (LBL) where the peak in energy is in the IR - optical bands and high-energy peaked (HBL) with a peak in the UV - X-ray bands (Padovani & Giommi (1995) [78]). The latter is used as a template SED for low luminosity blazars in our modelling.

- OVV quasars

They are characterized by a strong radio emission, rapid variability, strong polarization and the presence of broad and narrow emission lines in their spectra while the optical emission lines are absent in BL Lacs objects. In addition OVV quasars are much more luminous than BL Lacs.

*Host galaxy:* ellipticals, cD galaxies <sup>1</sup>.

<sup>1</sup>cD galaxies are elliptical galaxies which belong to bright cluster galaxy (BCG) and defined as the brightest galaxy in the cluster.

## 2.1.4 Summary

AGN can be classified into radio-quiet and radio-loud AGN. They are characterised by their luminosity which is dominant at least at the radio wavelengths and possibly at some other wavelengths. Radio-quiet AGNs are fainter than radio-loud AGNs. Thus we can neglect their contribution to the contamination of the CMB in our model. We focus our study on radio-loud AGNs which comprise FRI radio galaxies and BL Lacs for low luminosity AGN and FRII radio galaxies and blazars for high luminosity AGN.

## 2.2 Unified model of AGN

### 2.2.1 Introduction

The unified model of AGN states that the apparent difference in properties of observed AGN is due to their orientation toward us (orientation-based unified models). In the unified model AGN are assumed to have the same internal structure of the nucleus but viewed with different angle from the observer. AGN are powered by accretion of interstellar gas onto a supermassive black hole which stands at the centre of galaxies. As the gas has some rotation energy it does not directly free fall onto black hole but spirals, forming an accretion disk. As the material spirals in, jets of heated matter are ejected with relativistic speed. The AGN emit radiation in the radio, X and gamma ranges due to relativistic jet of particles and in the far-infrared range due to the dust surrounding the central region. AGN spectra show broad emission lines emitted by ionized gas. Optical and UV lines are broadened by Doppler effect. Their width is compatible with the motions of gas rotating at 1000 - 10000 Schwarzschild radii ( $1.5 \times 10^{13}$  cm for a black hole mass  $10^8 M_{\odot}$ ) from the black hole (Collin & Huré (2001) [27]). This zone is the Broad Line Region (BLR). The term comes from the broad spectral lines emitted from the diffuse low ionization of the dense clouds that have formed in this region. Moving outward further to a scale of about 100 light years there exists opaque gas and dust that surround the AGN which is referred to as an "obscuring torus" which is thick and opaque to light. Outside the torus there is a thin layer of lower density gas which is known as the Narrow Line Region (NLR), because it displays spectra which is strong in the

forbidden lines (Davies et al. (2007) [34]). We present in the following the unified theory of radio-quiet and radio-loud AGN.

### 2.2.2 Radio-quiet AGN

The unified model proposes that Seyfert 2 galaxies and Seyfert 1 galaxies are the same objects viewed from different angle. For Seyfert 1 the observer can see the active nucleus directly while for Seyfert 2 the optical continuum, X-ray continuum or the broad-line region are not visible due to an obscuring torus of dust of gas. The obscuring material around the accretion disk in Seyfert 2 galaxies is large enough to hide the broad emission lines but it is not large enough to obscure the narrow lines.

Radio emission from *radio-quiet quasars* (RQQ) is very weak so that we can neglect their contribution in this work.

### 2.2.3 Radio-loud AGN

Low luminosity FRI radio galaxies are unified with BL Lacs and high luminosity FR II radio galaxies are unified with brighter blazars (Padovani (2007) [77]) (flat spectrum radio quasars FSRQ). In the unified scheme BL Lacs are just FRI radio galaxies with jets viewed at a small angle  $\lesssim 15^\circ$ . Similarly FR II radio galaxies are the same population as the brighter blazars. Blazars are just FR II radio galaxies viewed with a small angle  $\lesssim 15^\circ$  with respect to the line of sight of the observer. Blazars and radio quasars constitute the population of *radio-loud quasars* (RLQ).

Steep spectrum radio quasars (SSRQ) as opposed to blazars (FSRQ) are viewed at angles between those of FSRQ and FR II. The radio spectral index  $\alpha_r = 0.5$  is considered as the separation between FSRQ and SSRQ. The most important for our modelling are BL Lacs at low luminosity and blazars at high luminosity: they constitute the blazar population characterized by their jets oriented toward the observer with flat radio spectra  $\alpha_r \lesssim 0.5$ .

The viewing angle  $\theta$  with respect to the line of sight of the radio source is related to the relativistic Doppler factor  $\delta$  by

$$\delta = \frac{1}{\gamma(1 - \beta \cos \theta)} \quad (2.1)$$

where

$$\gamma = \frac{1}{\sqrt{1 - \beta^2}} \quad (2.2)$$

is the Lorentz factor and  $\beta = \frac{v}{c}$  the ratio between the jet speed and the speed of light. If  $L_{\text{em}}$  is the luminosity of the emitting source in the rest frame the observed luminosity is given by (Padovani (2007) [77])

$$L_{\text{obs}} = \delta^p L_{\text{em}} \quad (2.3)$$

where  $p \simeq 2.6$  for a characteristic spectral index  $\alpha \simeq 0.8$ . For a small angle  $\theta \simeq 0^\circ$ ,  $\delta \simeq 2\gamma$  and the observed luminosity is amplified by a factor of 400 to 10,000. For typical angles  $\theta \simeq \frac{1}{\gamma}$ ,  $\delta \simeq \gamma$  and the amplification is about 100 to 1000. Thus for jets close to the line of sight of the observer the luminosity is overestimated. This is the relativistic beaming in the unified model which is produced by relativistic emitting plasma at small angle with respect to the observer. It gives rise to a strong amplification and collimation in the rest frame of the observer (see Padovani (2007) [77]). Figure (2.4) gives a brief summary of the unified theory of radio AGN based on the orientation of the jet.

The orientation of radio AGN is important in our modelling since it allows us to classify the radio sources as flat or steep spectrum. We are interested in flat spectrum populations of BL Lacs (low luminosity blazars) and high luminosity blazars which are viewed with an angle very close to our line of sight. For steep spectrum populations of FRI (low luminosity radio galaxy) and FR II (radio-loud quasars) the jets are not collimated directly toward the observer so that the power received by the telescope can be smaller than that from flat spectrum radio sources. However as they constitute the largest fraction of radio populations their flux contributions can be enough to contaminate cluster signatures in CMB experiments at the same level as flat spectrum radio galaxies and quasars. We focus mainly at this stage of the modelling on flat spectrum radio sources.

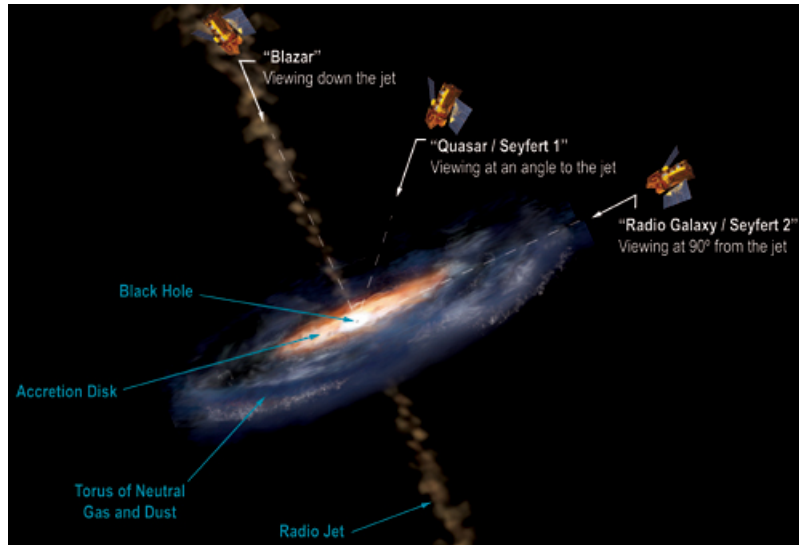


**Figure 2.4:** *Unified model of AGN. Radio galaxies and Seyfert 2 are viewed at an angle  $\sim 90^\circ$  from the jet. Quasars and Seyfert 1 are viewed at an angle looking down the jet. Seyfert 1 and Seyfert 2 are RQQ and radio galaxies, quasars and blazars are RLQ (source: [http : //www.whatsnextnetwork.com/technology/media/active\\_galactic\\_nuclei.jpg](http://www.whatsnextnetwork.com/technology/media/active_galactic_nuclei.jpg)).*

## 2.2.4 Summary

The energy output in active galaxies in at least some wavebands is dominated by non thermal emission. AGN come in different 'species'. Radio AGNs are of particular interest in our study since they can be found in the core of clusters (a few kpc). A large fraction of radio AGN are radio-quiet but the fluxes of these radio sources are not significant compared to the flux contributions of radio-loud AGN. Radio-loud AGN are located in luminous elliptical galaxies which are preferentially found in clusters (Yates et al. (1989) [130]). Radio-quiet AGN are conversely not found in regions of significant enhancement. This is consistent with the fact that they are often hosted by spiral galaxies (Boyle & Couch (1993) [17]). The most powerful AGN are blazars and since their radio fluxes at some frequencies can exceed or be in the same order as the SZE fluxes in galaxy clusters, they constitute a problem for the detection of clusters. Hence we need to model their spatial and fluxes distribution.



## 2.3 Mechanism of emission

Radiation from astrophysical sources can be characterized by different emission processes which include *black body emission* (e.g. CMB), *bremsstrahlung*, *synchrotron emission* and *compton scattering*.

When the emitting source is in thermal balance it has the characteristic of a black body spectrum and the temperature of the source is uniform. The cosmic microwave background is a blackbody of a temperature  $T \simeq 2.73$  K. We can describe the black body emission by the Planck function

$$I_\nu = \frac{2h\nu^3}{c^2} \frac{1}{e^{\frac{h\nu}{kT}} - 1} \quad (2.4)$$

where  $h = 6.626 \times 10^{-27}$  erg s is the Planck constant and  $k = 1.38 \times 10^{-16}$  erg K<sup>-1</sup>. At low radio frequencies ( $h\nu \ll kT$ ) the Planck function can be written as

$$I_\nu = \frac{2\nu^2}{c^2} kT. \quad (2.5)$$

This low frequencies regime where the particle behaves like a classical particle is called the Rayleigh-Jeans part of the spectrum.

For  $\frac{h\nu}{kT} \gg kT$  we have to consider the quantum nature of the particle to explain the observed properties of the black body spectrum. At this regime we have

$$e^{\frac{h\nu}{kT}} - 1 \simeq 1 \quad (2.6)$$

$$I_\nu = \frac{2h\nu^3}{c^2} e^{-\frac{h\nu}{kT}}. \quad (2.7)$$

This is the Wien part of the black body spectrum. We can see that when the frequency is increasing the intensity of the radiation falls off rapidly. This explains exactly the shape of the CMB black body spectrum observed in different CMB experiments.

Some astrophysical sources like HII regions which contain ionised gas caused by UV photons

from hot stars emit *bremsstrahlung* radiation. This emission is also called *free-free emission* since the electrons move between free states and not between bound states during the interaction. In this case the radiation is produced when electrons pass charged particles (protons with charge  $+Ze$ ). During the passage, the electrons emit photons losing their kinetic energy resulting in the name braking radiation or *bremsstrahlung*.

For one electron the acceleration during the interaction with a proton is not uniform and therefore it emits electromagnetic waves with different wavelengths. The corresponding wavelength range is the spectrum. The radiated power is given by the Larmor's formula

$$P = \frac{2e^2 a^2}{3c^3} \quad (2.8)$$

where  $a$  is the acceleration of the electron with charge  $e$  and  $c$  the speed of light. The interaction between the electron and proton produces a flat spectrum with a frequency cut-off  $\omega_c$ . The interaction frequency  $\omega_c$  is related to the interaction time by

$$\omega_c = \frac{1}{\Delta t} \quad (2.9)$$

$$= \frac{b}{v} \quad (2.10)$$

where  $b$ , impact parameter, is the distance of closest approach of the electron to the proton and  $v$  the speed of the electron. The expression of the intensity in the flat part of the spectrum is given by

$$I = \frac{8Z^2 e^6}{3\pi c^3 m_e^2 v^2 b^2}. \quad (2.11)$$

For a population of electrons with a thermal velocity and density distribution the total emission is called *thermal bremsstrahlung*. This is characterised by a flat spectrum up to a cut-off frequency  $\omega_c$  followed by an exponential fall-off at higher frequencies. This defines the shape of the spectrum in an optically thin region where the radiation is free to escape from the emitting region.

In star forming regions where the medium is optically thick photons do not move freely,

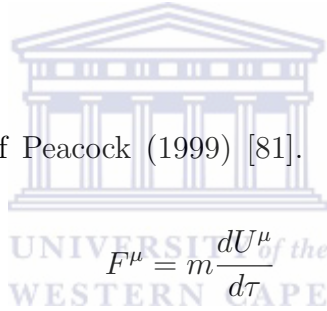
they interact with the medium and after being emitted they are absorbed again. The shape of the spectrum is fixed by the emission and absorption processes. At low frequencies the intensity of the radiation has a power law dependence in frequency  $I \propto \nu^2$  and at higher frequencies  $I \propto e^{-\frac{h\nu}{kT}}$ . In the optically thick frequency range, the emission is thus 'self-absorbed'.

More interesting for us is the emission in AGN which is associated with relativistic electrons that we are looking now in the following Section (2.3.1).

### 2.3.1 Synchrotron radiation

The *synchrotron radiation* is a radiation emitted by fast moving electrons with relativistic speed spiralling along magnetic fields. As it is important for us we treat it in more detail in this section.

Here we follow the approach of Peacock (1999) [81]. We use the relativistic equation of motion of the electron given by



$$F^\mu = m \frac{dU^\mu}{d\tau} \quad (2.12)$$

where  $F^\mu$  is the 4-force and  $U^\mu$  the 4-velocity. Using the field tensor  $F^{\mu\nu} = \partial^\mu A^\nu - \partial^\nu A^\mu$  where  $A^\mu$  is the 4-potential, the covariant expression of the equation is

$$m \frac{dU^\mu}{d\tau} = e F^{\mu\nu} U_\nu. \quad (2.13)$$

The spatial components of this equation of motion give the Lorentz force

$$\underline{\mathbb{F}} = m\gamma \underline{\ddot{x}} + (\underline{\mathbb{F}} \cdot \underline{\dot{x}}) \frac{\underline{\dot{x}}}{c^2} \quad (2.14)$$

$$= e(\underline{\mathbb{E}} + \underline{\dot{x}} \wedge \underline{\mathbb{B}}) \quad (2.15)$$

where  $\underline{\mathbb{F}}$  is the force,  $m$  the mass of electron,  $c$  the speed of light and  $\gamma$  the Lorentz factor.  $\underline{\dot{x}}$  and  $\underline{\ddot{x}}$  are respectively the velocity and acceleration of the electron in the electric field  $\underline{\mathbb{E}}$  and magnetic field  $\underline{\mathbb{B}}$ . The force acting in the electron for a purely magnetic field is  $\underline{\mathbb{F}} = \underline{\dot{x}} \wedge \underline{\mathbb{B}}$ .

This means that the force is orthogonal to the velocity and this produces an helical motion of the electron. The frequency of the giration is called *gyrofrequency* and it is related to the Larmor frequency  $\omega_L$  by

$$\omega_g = \frac{1}{\gamma} \omega_L \quad (2.16)$$

$$= \frac{eB}{\gamma m} \quad (2.17)$$

where  $m$  is the rest mass. The radiation energy per unit time in the rest frame of the electron is given by the Hertzian dipole

$$-\frac{dE}{dt} = \frac{|e\ddot{x}|}{6\pi\epsilon_0 c^3} \quad (2.18)$$

where  $\epsilon_0$  is the permittivity of vacuum. The minus sign means that the electron loses energy in the form of electromagnetic radiation. We need to transform the equation to the observer's frame. For a symmetrically radiating electron the rate of change of the momentum  $\dot{p}$  is zero so that  $\dot{E}$  is the same in all frames. To transform the acceleration we use the norm of the 4-acceleration

$$a^\mu a_\mu = -a_0^2 \quad (2.19)$$

where  $a_0$  is the acceleration in the rest frame. We have

$$a^\mu = \gamma \left( \frac{d}{dt} (\gamma, \gamma \dot{\mathbf{x}}) \right) \quad (2.20)$$

$$= (0, \gamma^2 \mathbf{a}) \quad (2.21)$$

which implies  $a_0^2 = (\gamma^2 a)^2$ . After putting all together we get the observed radiation power given by

$$P_{\text{sync}} = -\frac{dE}{dt} = 2\sigma_T \gamma^2 \beta^2 \sin^2 \theta U_{\text{mag}} c \quad (2.22)$$

where  $\sigma_T$  is the Thomson cross-section,  $\gamma$  the Lorentz factor,  $\beta = \frac{v}{c}$ ,  $\theta$  the pitch angle defined by  $\cos \theta = \mathbf{v} \cdot \mathbf{B}$  and  $U_{\text{mag}} = \frac{B^2}{2\mu_0}$  is the magnetic energy density. The spectrum of the radiation is obtained by taking the Fourier transform of the time dependent radiation. The electron energies span over a broad spectrum and the emission can be described by a delta function

where the frequency of oscillation is related to the gyrofrequency  $\nu_g$  by  $\nu = \gamma^3 \nu_g$ .

The synchrotron emissivity of the electron is defined by

$$\epsilon_\nu = 4\pi j_\nu \quad (2.23)$$

$$= -\dot{E}N(E)\frac{dE}{d\nu} \quad (2.24)$$

where  $j_\nu$  is the current density and  $N(E)$  the number of electrons emitting in the interval of energy  $[E, E + dE]$ . We assume a power law spectrum

$$N = N_0\gamma^{1-p} \quad (2.25)$$

where  $N_0$  is the total electron number density. Hence

$$N(E) = N_0(p-1)(mc^2)^{p-1}E^{-p} \quad (2.26)$$

$$\epsilon_\nu \simeq N_0(p-1)\frac{\mu_0 c e^3}{18\pi m}\left(\frac{e}{m}\right)^{\frac{p-1}{2}}B^{\frac{p+1}{2}}\nu^{\frac{1-p}{2}}. \quad (2.27)$$

We assume that the radiation is isotropic and we get  $\langle \sin^2 \theta \rangle = \frac{2}{3}$ .

The synchrotron emissivity formula defines the *spectral index* as

$$\epsilon_\nu \propto \nu^{-\alpha} \quad (2.28)$$

where  $\nu$  is the frequency of emission and  $\alpha = \frac{p-1}{2}$  the spectral index of the spectrum.

A detailed derivation of the synchrotron emissivity can be found in Rybicki & Lightman (1979) [93]. A more exact expression of the emissivity is

$$\epsilon_\nu = 2.14 \times 10^{-30}(p-1)N_0 a(\alpha) \left(\frac{B}{100 \text{ nT}}\right)^{1+\alpha} \left(\frac{\nu}{4 \text{ kHz}}\right)^{-\alpha} \text{ W.Hz}^{-1} \quad (2.29)$$

where  $a(\alpha) \simeq 0.08$  for spectral indices between 0.5 and 1. The formula holds for optically thin region where there is insufficient material to re-absorb the radiation emitted by the population of electrons.

This is in particular the main mechanism of emission in radio AGN and depending on the value of the spectral index  $\alpha$  we classify them as flat spectrum or steep spectrum radio sources. Most radio galaxies and quasars have a spectral index with a mean value  $\alpha \sim 0.8$  and they are called steep spectrum radio sources. We summarize in Table (2.1) the classification of the spectrum of the radio sources according to the spectral index by assuming the relation  $\epsilon_\nu \propto \nu^{-\alpha}$ .

**Table 2.1:** *Classification of the spectrum of radio sources according to the spectral index  $\alpha$ .*

Spectral index $\alpha$	Radio spectrum
$\alpha \geq 1.2$	ultra steep spectrum
$0.5 \leq \alpha \leq 1$	steep spectrum
$0 \leq \alpha \leq 0.5$	flat spectrum
$\alpha < 0$	inverted spectrum

The values of the spectral index for extended radio sources are  $0.5 < \alpha < 1.3$ . Over a wide range of frequencies the spectral index is nearly equal to 0.8 with a dispersion of 0.15. Radio sources with spectral index  $\alpha \lesssim 0.5$  are very compact and their flat spectrum is the result of self-absorption (Kellermann & Owen (1988) [54]).

In general the radio spectrum of radio galaxies and quasars ( $\nu F_\nu$  as a function of the frequency  $\nu$  where  $F_\nu$  is the flux density of the emitting source) show two peaks. The first peak is due to the synchrotron emission and the second peak corresponds to the inverse Compton radiation that we describe in the following Section (2.3.2).

### 2.3.2 Inverse Compton

The Thomson scattering of a photon by an electron at rest applies to low energy photons ( $h\nu \ll m_e c^2$ ). If the photon energy is comparable or greater than the electron energy the process is called *Compton scattering*.

In the case that the electron is moving fast (an ultrarelativistic electron), energy is trans-

ferred to the photons and the process is called *inverse Compton scattering* which is one of the dominant mechanism of emission in high energy astrophysics.

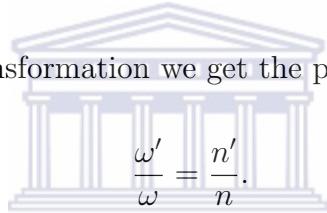
As in the case of the synchrotron emission the radiation energy rate or power  $\dot{E}$  is invariant. We consider photons moving in the lab frame at an angle  $\theta$  with respect to the velocity of electrons with a density  $n$ . The expression of the 4-current is

$$J^\mu = nc(1, \cos \theta). \quad (2.30)$$

Hence the density in the frame of the electron is

$$n' = n \gamma(1 - \beta \cos \theta) \quad (2.31)$$

and using the 4-wavevector transformation we get the photons frequency  $\omega'$  from



$$\frac{\omega'}{\omega} = \frac{n'}{n}. \quad (2.32)$$

The power of the radiation is then

$$-\dot{E} = nc\sigma_T\hbar\omega\gamma^2(1 - \beta \cos \theta)^2. \quad (2.33)$$

The total number density of photons  $n_{\text{tot}}$  is obtained by integrating over the isotropic photon distribution and the energy loss per unit time is given by

$$-\dot{E} = c\sigma_T\gamma^2\left(1 + \frac{\beta^2}{3}\right)U_{\text{rad}} \quad (2.34)$$

where  $U_{\text{rad}} = n_{\text{tot}}\hbar\omega$  is the energy density of photons. As the electron scatters photons at the same rate in the lab and rest frames for an isotropic distribution of the photons the rate of the energy loss is  $c\sigma_T U_{\text{rad}}$  (Peacock (1999) [81]). Then the final equation of the inverse Compton scattering is

$$-\dot{E}_{\text{inc}} = \frac{4}{3}\sigma_T\gamma^2\beta^2U_{\text{rad}} c. \quad (2.35)$$

The average increase in energy is expressed by

$$\left\langle \frac{\nu'}{\nu} \right\rangle = \gamma^2 \left( 1 + \frac{\beta^2}{3} \right). \quad (2.36)$$

If  $\gamma \gg 1$ , then  $\nu \propto \gamma^2$  and the spectrum has the same form as for synchrotron radiation.

Inverse Compton scattering is an important process for high-resolution CMB experiments as low energy CMB photons can be upscattered to higher frequencies by electrons in the hot intergalactic gas present in clusters of galaxies (the intracluster medium, ICM).

## 2.4 Cosmological background

We now introduce some cosmological concept that we will use in the modelling of radio sources. We describe the expansion of the universe with the scale factor  $a(t)$  which is related to the redshift  $z$  by:

$$z(t) = \frac{1}{a(t) - 1}. \quad (2.37)$$

The current expansion rate is  $H_0 = 100 h \text{ km}^{-1} \text{ s}^{-1} \text{ Mpc}^{-1}$ .  $H_0$  is called the Hubble constant and  $h$  the Hubble parameter.

Let consider for now the Einstein field equation of the general relativity:

$$R_{\mu\nu} - \frac{1}{2}g_{\mu\nu}R + g_{\mu\nu}\Lambda = \frac{8\pi G}{c^4}T_{\mu\nu} \quad (2.38)$$

where  $R_{\mu\nu}$  is the Ricci tensor,  $g_{\mu\nu}$  the metric tensor,  $R$  the scalar curvature,  $\Lambda$  the cosmological constant,  $T_{\mu\nu}$  the stress-energy tensor,  $G$  the gravitational constant and  $c$  the speed of light. This equation relates sixteen symmetric tensors and each of them has ten independent components so that the Einstein field equation is reduced to six independent components.

The most important of them are the Friedmann equation (00 component of the tensor):

$$H^2 = \left( \frac{\dot{a}}{a} \right)^2 = \frac{8\pi G}{3}\rho - k\frac{c^2}{a^2} + \frac{\Lambda c^2}{3}. \quad (2.39)$$



The equation (2.39) contains all contributions from matter, radiation and vacuum. For a 'flat' universe  $k = 0$  corresponds a *critical density*  $\rho_c$  given by

$$\rho_c = \frac{3H^2}{8\pi G}. \quad (2.40)$$

A universe is closed if the density is above the critical density  $\rho_c$  and is open for a lower density  $\rho < \rho_c$ . Current observations show that our universe is nearly flat.

The cosmological model is expressed in terms of homogeneous and isotropic line element defined by the scale factor and the spatial curvature. We can determine distance, volume and time as a function of redshift using the Robertson-Walker (RW) metric defined by the line element

$$ds^2 = c^2 dt^2 - a(t)^2 \left[ \frac{dr^2}{1 - kr^2} + r^2 (d\theta^2 + \sin^2 \theta d\phi^2) \right] \quad (2.41)$$

where  $k$  is the spatial curvature and  $(r, \theta, \phi)$  the comoving coordinate. Distances, volumes and times in the universe cannot be observed directly. They are defined from their relationship with observed quantities. We determine distances and volumes from the path of a photon as it travels through the universe. The trajectories of the photons are, by definition, null geodesics  $ds^2 = 0$ . We consider a radial trajectory  $d\theta = d\phi = 0$ . We obtain from the RW line element

$$cdt = \frac{a(t)dr}{\sqrt{1 - kr^2}}. \quad (2.42)$$

By integrating between the path of the photon which is emitted at  $(t = t_1, r = 0)$  and received at  $(t = t_0, r)$ , we have

$$\int_{t_1}^{t_0} \frac{c}{a(t)} dt = \int_0^r \frac{dr'}{\sqrt{1 - kr'^2}}. \quad (2.43)$$

The coordinate radius between the source and the observer is defined by

$$S(r) = \int_0^r \frac{dr}{\sqrt{1 - kr^2}}. \quad (2.44)$$

The integration of the above formula gives

$$= \sin(r) \text{ for } k = +1, \quad (2.45)$$

$$S(r) = r \text{ for } k = 0, \quad (2.46)$$

$$= \sinh(r) \text{ for } k = -1. \quad (2.47)$$

The physical radius which gives the separation between the source and the observer is  $a(t) S(r)$ .

### 2.4.1 Luminosity distance

The *luminosity distance* is defined by

$$d_L = \sqrt{\frac{L_{\text{bol}}}{4\pi F_{\text{bol}}}} \quad (2.48)$$

where  $L_{\text{bol}}$  is the bolometric luminosity and  $F_{\text{bol}}$  the observed bolometric flux of the object. The photon from the object reaches us after travelling a radial distance  $a_0 S(r)$  and is distributed over a surface area  $4\pi(a_0 S(r))^2$ . We need two additional factors.

- As the energy of the photon decreases proportionally to the redshift we have

$$h\nu_0 = \frac{h\nu_e}{1+z}. \quad (2.49)$$

- The rate of the reception of photons decreases by a factor  $1+z$  as  $\frac{\Delta t_0}{\Delta t_e} = \frac{a_0}{a_e} = 1+z$ .

Hence the flux is given by

$$F_{\text{bol}} = \frac{L_{\text{bol}}}{4\pi(a_0 S(r))^2(1+z)^2} \quad (2.50)$$

where

$$d_L = (a_0 S(r))(1+z) \quad (2.51)$$

is the luminosity distance.

## 2.5 Cosmic Microwave Background

### 2.5.1 Introduction

We review in this section some features of the Cosmic Microwave Background (CMB) radiation. CMB is a form of radiation observed in all directions of the sky which is a consequence of the hot Big Bang. It was discovered in 1964 by Penzias and Wilson. Using a radio telescope they detected a faint background glow that filled isotropically the region of the sky. As the radiation emitted peaked in the microwave part of the spectrum it was called CMB. The Big Bang model predicts that the CMB has a blackbody spectrum with a temperature about 2.725 K. The peak in frequency is at 160.2 GHz. Inflationary cosmology predicts also that there should be small-scale perturbations in temperature across the sky. It is isotropic to about one part in 100 000 and the root mean square variations are 18  $\mu\text{K}$  (Wright (2004) [128]). The theory of inflation predicts that the universe underwent an exponential growth  $10^{-37}$  seconds after the Big Bang and followed by a symmetry breaking. This was a transitional phase that brought the universe from a random state to a more ordered state: formation of the elementary particles and the four fundamental interactions: gravitation, electromagnetic, strong and weak interactions. After  $10^{-6}$  s the universe was composed by a plasma of electrons, baryons (neutron and proton) and photons. These particles underwent electromagnetic interactions through Thomson cross-section which is given by:

$$\sigma_{\text{T}} = \frac{8\pi}{3} \left( \frac{e^2}{mc^2} \right)^2 \quad (2.52)$$

$$\simeq 6.65 \times 10^{-25} \left( \frac{m_e}{m} \right)^2, \quad (2.53)$$

where  $m$  is the mass of the generic particle,  $e$  the electron charge and  $c$  the speed of light. For electrons the Thomson cross-section is  $\sigma_{\text{T}} = 6.65 \times 10^{-25} \text{ cm}^2$ . Plasma cooled down as the universe expanded and at the final stage of the plasma epoch electrons and protons combined to form hydrogen. This is the recombination epoch at an approximate redshift  $z_{\text{rec}} \simeq 1100$

when the universe was about 379 000 years old. The temperature at recombination was about 3600 K (Liddle (2003) [57]). Then began the era of neutral matter as the photons scattered freely through the universe: this was the time of decoupling between matter and radiation. The CMB photons that we observe today come from the surface of last scattering where the decoupling occurred about 379 000 years after the Big Bang.

## 2.5.2 Sunyaev-Zeldovich effect

### Introduction

The *Sunyaev-Zeldovich (SZ) effect* was first predicted by Sunyaev & Zeldovich in 1970 (Sunyaev & Zeldovich (1970) [110], Sunyaev & Zeldovich (1972) [111]). It produces secondary anisotropies of the CMB radiation due to the scattering of CMB photons by free electrons. The primary anisotropies in the CMB are due to the non-uniformity of the matter and radiation just before the Universe cooled to form transparent atoms (Feroz et al. (2008) [41]). This is observed for example in galaxy clusters where the intracluster medium (ICM) contains hot electrons: the blackbody spectrum of the microwave background radiation is distorted through the clusters and it can be used to detect these objects (Figure (2.5)). The effect is independent of redshift and therefore we can detect very distant clusters as easily as closer ones. For this reason the SZ Effect (SZE) is an important tool for observational cosmology. The CMB photons interact with the electrons through inverse Compton scattering where the photons gain energy from the hot electrons within the ICM of galaxy clusters. This results in the upscattering of low energy photons to higher frequencies so that we lose lower frequency photons and gain higher frequencies photons. At radio wavelengths we see a 'hole' in the CMB and at millimetre wavelengths we see a bright patch (Figure (2.6)). The magnitude of the effect is  $\lesssim 1$  mK for an energetic electron passing through the centre of a massive cluster (Carlstrom et al. (2002) [22]).

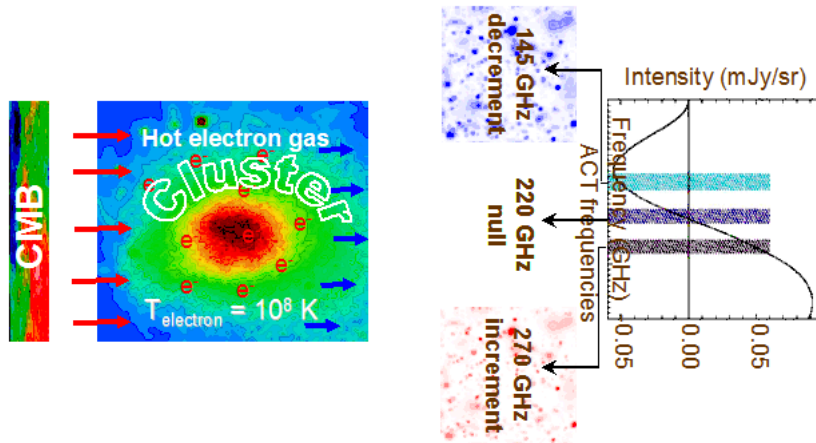


**Figure 2.5:** SZ effect in clusters. The ICM of clusters contain hot electron gas of temperature  $T \sim 10^8 \text{ K}$ . The scattering of the CMB photons by hot gas results in the transfer of low energy photons to higher energies causing a distortion of the CMB black body spectrum. The three frequencies shown are the Atacama Cosmology Telescope (ACT) observation frequencies. No deviation is observed at the central frequency 220 GHz (a precise calculation gives a frequency  $\sim 218 \text{ GHz}$ ) (Credit: Verde and Spergel (2002)).

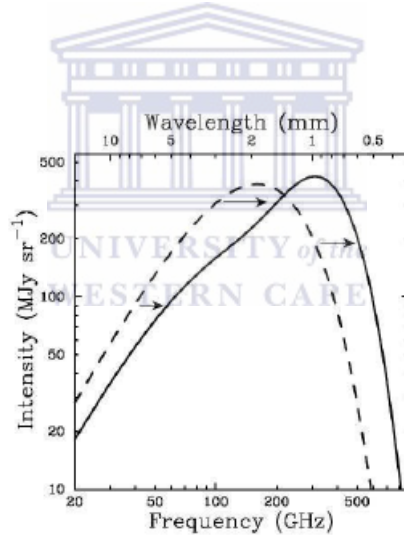


**Figure 2.6:** Distortion of the CMB blackbody spectrum by inverse Compton scattering. The dashed line is the initial spectrum of the background radiation and the solid line is the distorted spectrum after scattering. The intensity of radiation decreases at radio wavelengths and increases at millimetre wavelengths. There is a 'null' frequency where the spectrum shows no distortion (218 GHz). This is the characteristic spectral SZ signature of galaxy clusters. The distortion shown is for a fictional cluster thousand times more massive than a typical massive cluster (adopted from Carlstrom et al. (2002) [22]).

Over the last decade more than 50 clusters have been detected using the SZ effect at redshift up to one. The next generation instruments like Planck (Planck collaboration (2006) [87])

and ACT (Kosowsky (2004) [55]) or those being planned will be more efficient. Such surveys should find about  $10^4$  clusters. As we can probe the deep universe at high redshift with the SZ surveys of clusters, it allows us to view the growth of large scale structure. We can determine cosmological parameters by combining for example SZE with the observation of X-ray emission in galaxy clusters, lensing by the cluster potential and optical galaxy velocity dispersion measurements (Carlstrom et al. (2002) [22]). We can measure using a sample of galaxy clusters at high redshift the angular diameter distance that is sensitive to cosmological parameters and the redshift as well. In addition we can constrain the fraction of gas mass in clusters by combining SZE and X-ray measurements and this can be used to get an estimate of the density of matter  $\Omega_m$  in the universe. SZE provides a tool for measurements of the number density of clusters as a function of redshift. As the evolution in cosmic time of the cluster density depends on the underlying cosmology, it can be used to constrain the equation of state of dark energy. This shows us the importance of the SZE survey of galaxy clusters and the necessity of working out the contamination of the SZ signatures by point sources which make the detection of clusters more difficult. Our task is to track the radio sources while the infrared sources also constitute a source of contamination. For a given SZE survey, the mass of the cluster will set the detection limit and not the redshift. This is because the SZE is a distortion of the CMB: it is affected by dimming with redshift but the ratio of the magnitude of the SZE to the CMB is not. The SZE is a redshift independent measurement of the intracluster gas column density weighted by temperature which is the pressure integrated along the line of sight. The SZE flux is proportional to the temperature-weighted mass and inversely proportional to the square of the angular diameter distance (Carlstrom et al. (2002) [22]).

### Thermal SZ effect

We now describe the SZ effect caused by hot thermal electrons in the ICM of galaxy clusters. The photons of CMB are scattered by the fast moving electrons in any direction. The frequency of photons changes because of Doppler shift and they gain energy from the hot gas electrons. We determine the spectral distribution of the scattered CMB photons which is described in Appendix (A).

The distortion of the spectrum is proportional to the electron temperature  $T_e$  if the velocity distribution of the electrons is isotropic. The photons gain energy from the hot gas in the ICM without change in the photon number. This results in the transfer of the photons from the R-J part of the spectrum to the Wien side. The changes in spectral intensity and temperature expressed in equations (A.5) and (A.8) of Appendix (A) are valid for the nonrelativistic limit. However at high frequencies we have to do some relativistic corrections.

We can predict the change in temperature from the thermal effect from the determinations of X-ray gas density, temperature and radial profiles. In the R-J side of the spectrum this change is about 0.1 to 1 mK which is in agreement with measurements (Birkinshaw (1990) [11]).



### Thermal SZ effect from galaxy clusters

The gas temperature in galaxy clusters is  $10^7 - 10^8$  K. For massive clusters, the measured gas temperature is around  $kT_e \simeq 10$  keV (Mushotzky & Scharf (1997) [72], Allen & Fabian (1998) [2]). The cluster mass scales with the temperature as  $T_e \propto M^{\frac{2}{3}}$  (Carlstrom et al. (2002) [22]). For very massive clusters the temperature of the hot gas is very high so that the electrons are moving at a relativistic speed. In this case we need to make relativistic corrections to the SZE. For galaxy clusters the temperature  $kT_e \lesssim 15$  keV. The corrections due to relativistic effects are of order of few percent in the R-J part of the spectrum for a massive cluster of temperature  $kT_e \simeq 10$  keV ( $\frac{kT_e}{mc^2} \simeq 0.02$ ).

The SZE signal is an integrated pressure. To find a cluster in an SZ survey we need to integrate over the solid angle of the cluster the SZ signal in order to obtain the sum of all of the electrons in the cluster weighted by temperature (Carlstrom et al. (2002) [22]). The Comptonization parameter  $y$  is the integral of the gas pressure along the line of sight  $l$  through the cluster and the total thermal energy of the cluster is proportional to the integral of the Comptonization parameter  $y$  over the solid angle  $d\Omega = \frac{dA}{D_A^2}$  of the cluster where  $D_A$  is

the angular diameter distance. We have

$$\int y d\Omega = \frac{\sigma_T}{mc^2} \int n_e k T_e dl d\Omega \propto \frac{1}{D_A^2} \int n_e T_e dV \quad (2.54)$$

where  $dV = dAdl$  is an element of the comoving volume (Feroz et al. (2008) [41]). Hence the integral of the Comptonization parameter which is the integrated SZ surface brightness is

$$\int y d\Omega \propto \frac{\langle T_e \rangle}{D_A^2} \int n_e dV \propto \frac{M^{\frac{5}{3}}}{D_A^2} \quad (2.55)$$

since  $\langle T_e \rangle \propto M^{\frac{2}{3}}$  where  $M$  is the total mass of the cluster. This relation means that the SZ brightness is proportional to the total mass of the cluster where we assume that the gas mass is proportional to the cluster mass:  $M_g = f_g M$  ( $f_g$  is the gas mass fraction).

We show in Figure (2.7) the distortion of the CMB by the SZE. The kinetic SZ effect which we describe in the next section is also shown in the figure for later comparison.

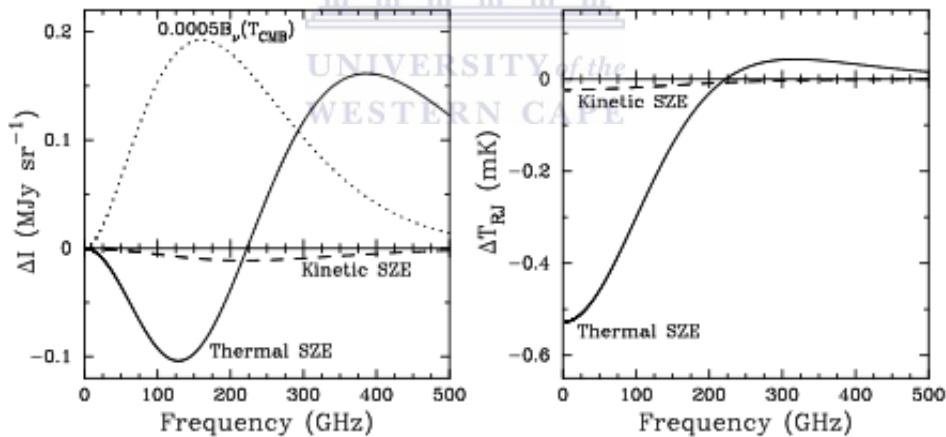


**Figure 2.7:** Distortion of the CMB blackbody spectrum. The solid line is the thermal SZE and the dashed line is the kinetic SZE. The left panel shows the intensity and the right panel the temperature brightness in the Rayleigh Jeans region of the spectrum. The SZ signature corresponds to a cluster with an electron temperature of 10 keV, a Comptonization parameter  $y = 10^{-4}$  and a peculiar velocity of  $500 \text{ km.s}^{-1}$  (adopted from Carlstrom et al. (2002) [22]).

We can summarize the features of the thermal SZ as follows.

- The thermal SZE is proportional to the cluster pressure integrated along the line of



sight producing a distortion of the CMB of  $\sim 1$  mK.

- The brightness of the SZ signal is independent of redshift (equation (2.55)).
- The SZE signature shows a characteristic decrease in the CMB intensity at lower frequencies  $\lesssim 218$  GHz and an increase at higher frequencies (Carlstrom et al. (2002) [22]).
- The integrated SZ signal is proportional to the total mass of the cluster which fixes the mass threshold that can be detected by the SZE survey.

### Kinetic SZ effect

Sunyaev & Zeldovich (1972) [111] noted that when the cluster is moving with a peculiar velocity with respect to the CMB rest frame there will be an additional distortion due to Doppler effect. The peculiar velocity of the cluster projected along the line of sight produces a distortion of the CMB which is known as the kinetic SZE. The kinematic change in intensity is given by Sunyaev & Zeldovich (1980) [112]

$$\Delta I_{\text{k}} = -i_{\text{o}} h(x) \frac{V_{\text{r}}}{c} \tau \quad (2.56)$$

where

$$h(x) = \frac{x^4 e^x}{(e^x - 1)^2}, \quad (2.57)$$

$V_{\text{r}}$  is the peculiar velocity along the line of sight and  $\tau$  the optical depth to Compton scattering (Rephaeli (1995) [90]) where

$$\tau = \sigma_{\text{T}} \int n_{\text{e}} dl. \quad (2.58)$$

$V_{\text{r}}$  is positive for a receding cluster and negative for approaching cluster. Unlike the thermal SZ effect the kinetic temperature change is independent of frequency and in the non-relativistic limit is given by

$$\Delta T_{\text{k}} = -T_{\text{CMB}} \frac{V_{\text{r}}}{c} \tau. \quad (2.59)$$

The emergent spectrum of the kinetic SZ can be described by a Planck function but with different temperature. Equation (2.59) shows that the temperature change is lower for a

receding cluster  $V_r > 0$  and higher for approaching cluster ( $V_r < 0$ ) (Carlstrom et al. (2002) [22], Sunyaev & Zeldovich 1972 [111], Phillips (1995) [86], Birkinshaw (1999) [12]).

Figure (2.8) shows the spectral dependence of the intensity for the non relativistic thermal SZE and the kinetic SZE.

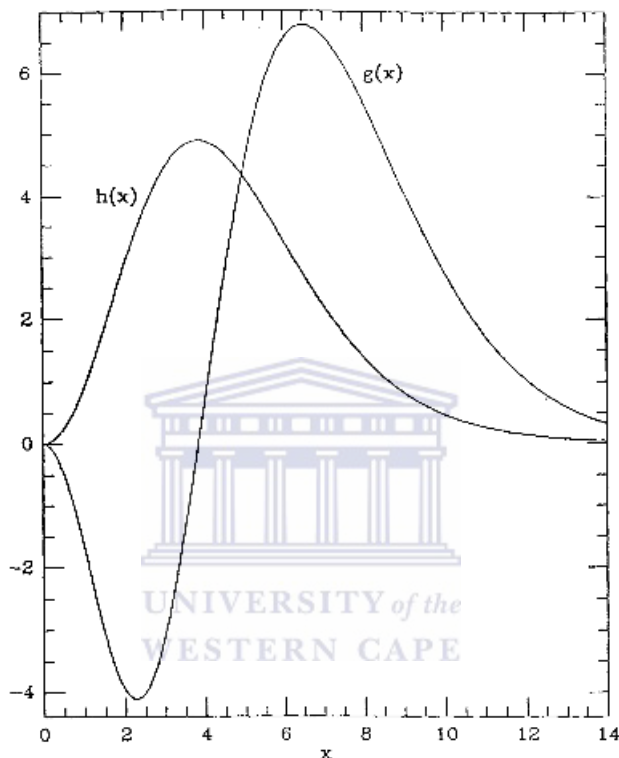


**Figure 2.8:** Spectral dependence of the SZE. The  $y$  axis is the intensity change  $\Delta I$  in CMB.  $g(x)$  is the spectral dependence for the non relativistic thermal SZE and  $h(x)$  the spectral dependence for the kinetic SZE (adopted from Rephaeli (1995) [90]).

### 2.5.3 Radio point source contamination

Sehgal et al. (2009) [97] modelled radio point sources similarly to the treatment of the subject by Wilman et al. (2008) [125] that we can summarize as follow. In their model Wilman et al. (2008) [125] use a 'semi-empirical' simulation of the extragalactic radio continuum sky. 'Semi-empirical' means that the simulated sources are obtained by sampling the observed radio continuum luminosity functions. The simulation covers a sky area of  $20 \times 20 \text{ deg}^2$  which corresponds to the plausible upper limit to the field of view of the future aperture array like the Square Kilometre Array. The redshift goes up to  $z = 20$  with flux density limits of 10 nJ at 151 MHz, 610 MHz, 1.4 GHz, 4.86 GHz and 18 GHz. They consider five source types: radio-quiet AGN, radio-loud AGN of the FRI and FRII classes and star-forming galaxies which comprise quiescent or 'normal' late-type galaxies and more luminous and compact starburst galaxies. Unlike Wilman et al. (2008) [125], Sehgal et al. (2009) [97] do not consider radio-quiet AGNs and star-forming galaxies in the model. This has a negligible effect in the simulation since they simulate the microwave sky at flux limits  $\gtrsim 0.1 \text{ mJy}$ . Sehgal et al. (2009) [97] create a halo occupation distribution and radio luminosity distribution for radio sources at 151 MHz to match the 151 MHz radio luminosity function (RLF) at  $z \sim 0.1$ . The RLF gives the number density of radio sources as a function of redshift. They chose this low frequency 151 MHz because the biases due to orientation effect is much smaller at low frequencies and the RLF is dominated by the steep spectrum lobes. After obtaining the match with the 151 MHz RLF at low redshifts, the radio sources are divided into two populations: low power FRIs with mild redshift evolution and high power FRIIs with strong redshift evolution, and the RLF at 151 MHz at high redshift is matched to observations. They follow Wilman et al. (2008) [125] and Jackson & Wall (1999) [50] and use a relativistic beaming model to separate the contributions to the total flux at 151 MHz from the compact core and the extended lobes and adjust the shape of the radio core SED to match source counts at  $\nu \gg 151 \text{ MHz}$  where the core dominates (Lin et al. (2009), in prep). In the simulation dark matter particles are evolved in a periodic box using the Tree-Particle-Mesh (TPM) N-body code (Bode & Ostriker (2003) [13]). The comoving length of the box is  $1000 h^{-1} \text{ Mpc}$  and the particle mass is  $6.82 \times 10^{10} h^{-1} M_{\odot}$ .

### 2.5.4 Summary

We reviewed in this section that the CMB, a relic radiation from the hot Big Bang emitted from the surface of last scattering, is a black body radiation with a temperature  $T = 2.726 \pm 0.010$  K (best-fit of COBE measurement with 95% confidence, Cole & Lucchin (2002) [26]). This spectral characteristics of the CMB can be used to detect the presence of clusters in our line of sight by studying the distortion of the CMB spectrum caused by hot electrons in the ICM. This distortion is explained by the SZ effect which is a very powerful cosmological probe of galaxy clusters since it is redshift independent. The SZ effect is characterised by two types of distortion: the thermal distortion caused by CMB photons scattering off hot intra-cluster electrons and in addition a kinetic distortion if the cluster is moving with respect to the CMB rest frame. The thermal effect is more significant at low frequency but the kinetic effect tends to be maximum at the frequency at which the thermal effect is null. In our modelling we use the three frequencies 145 GHz, 220 GHz and 270 GHz of ACT, since key science for this telescope is finding clusters using the SZ effect.

## 2.6 Millennium simulation

### 2.6.1 Introduction

In this section we describe the Millennium Run (Springel et al. (2005) [106]) presently known as the largest simulation of the formation of cosmic structure. It is a part of a programme of the Virgo Consortium which is an international group of astrophysicists from Germany, the UK, Canada and USA (Springel et al. (2005) [107]). The Millennium Run was completed in 2004 at the Max Planck Society's supercomputing centre in Garching, Germany. The simulation uses  $N = 2160^3$  dark matter particles of mass  $8.6 \times 10^8 h^{-1} M_{\odot}$  to trace the evolution of the dark matter distribution in a cubic region of the Universe. The periodic comoving box has a size  $500 h^{-1}$  Mpc on a side. The volume is large enough to include rare objects but it is small enough that the halos of all luminous galaxies brighter

than  $0.1 L_\star^2$  are resolved with at least 100 particles (Springel et al. (2005) [107]). The evolution of dark matter particles is followed from redshift  $z = 127$  to  $z = 0$ . The cosmology is a flat  $\Lambda$ CDM model. The cosmological parameters used are shown in Table (2.2). The units of density is the critical density  $\rho_c = \frac{3H_0^2}{8\pi G}$ .

**Table 2.2:** *Cosmological parameters used in the Millennium Run.*

Parameter	Description	Value
$\Omega_{\text{dm}}$	dark matter density	0.205
$\Omega_{\text{b}}$	baryon density	0.045
$\Omega_{\text{m}} = \Omega_{\text{dm}} + \Omega_{\text{b}}$	total matter density	0.25
$\Omega_{\Lambda}$	dark energy density	0.75
$n_s$	spectral index of the primordial power spectrum	1
$\sigma_8$	mass density fluctuation within a sphere of radius $8 h^{-1}$ Mpc extrapolated to $z = 0$	0.9
$h$	Hubble parameter in units $100 \text{ km s}^{-1} \text{ Mpc}^{-1}$	0.73

The simulation was carried out by V. Springel (Max Planck Institut für Astrophysik (MPA)) using a special version of the GADGET-2 code. Data is available online using SQL queries (<http://www.g-vo.org/Millennium>). A small subset ( $\frac{1}{512}$ ) of the data (known as the milli-Millennium data) is available without registration. The volume of the milli-Millennium box is about  $\frac{1}{512}$  times the volume of the Millennium box with 19,683,000 particles. It has the same resolution and uses the same cosmology as the Millennium Run. The Millennium Run simulation used in this work was carried out by the Virgo Supercomputing Consortium at the Computing Centre of the Max Planck Society in Garching, Germany (Springel et al. (2005) [107]).

## 2.6.2 Simulation description

As described in Croton et al. (2005) [32] the Millennium simulation uses a version of the GADGET-2 code (Springel (2005) [104]). The code is optimised to fit the 1 TB distributed

<sup>2</sup> $L_\star$  is the characteristic luminosity in the Schechter luminosity function which is about -20.9 mag in V-band.

memory of the IBM p690 parallel computer of the Computer Centre of the Max-Planck Society. The algorithm considers only gravitational interaction forces between particles and the method used is the 'TreePM' (Xu (1995) [129], Bode et al. (2000) [14] and Bagla (2002) [3]). This method is a combination of a 'tree' algorithm (Barnes & Hut (1986) [4]) and a Fourier transform particle-mesh method (Hockney & Eastwood (1981) [47]). The spatial resolution  $5 h^{-1}$  kpc (Plummer-equivalent) is available every where in the simulation volume achieving a dynamic range of  $10^5$  in 3D. The code ran in parallel with 512 processors requiring about 350 000 processor hours of CPU time or 28 days of wall-clock time (Croton et al. (2005) [32], Springel et al. (2005) [107]).

The particle data were output and stored at 64 times (64 snapshots), 60 of which are spaced regularly in the logarithm of the expansion factor between  $z = 20$  and  $z = 0$  allowing the construction of trees detailing how each dark matter halo at  $z = 0$  was built up through mergers and accretion. It is expressed by

$$\log(1 + z_n) = \frac{n(n+35)}{4200} \quad (2.60)$$

between  $z = 20$  and  $z = 0$ . This constitutes 60 snapshots and the four additional outputs correspond to  $z = 30, 50, 80$  and  $127$ . The simulation started at  $z = 127$  and evolved to the present using a leapfrog integration scheme with individual and adaptive timesteps with up to 11 000 timesteps for each particle. The stored particle data at 64 output times from the Millennium Run have a total volume of about 20 Tbytes. This allowed the construction of hierarchical merger trees for tens of millions of halos and for the subhaloes within these halos. Once the merger trees history is established we can follow the galaxy formation and evolution using a semi-analytical model that we will describe in Section (2.6.4).

### 2.6.3 Haloes and merger tree construction

The merging history trees are used in post-processing to simulate the baryonic processes related to the galaxies formation and evolution. The post-processing of the Millennium

simulation data proceeds in two steps: determination of friends-of-friends (FOF) <sup>3</sup> groups and running an algorithm that decomposes each FOF group in a set of gravitationally bound (sub)haloes. Croton et al. (2005) [32] use in post-processing an improved version of the SUBFIND algorithm of Springel et al. (2001) [108]. For further details see (Croton et al. (2005) [32]) and the Millennium simulation documentation at <http://www.gvo.org/MyMillennium/pages/help/HelpSingleHTML.jsp#simulation>.

We use a spherical-overdensity approach to compute the virial mass of each FOF halo. The centre is determined by the minimum gravitational potential within the group. The boundary is at the radius within which the mean overdensity is 200 times the critical density. The virial mass is then given by

$$M_{\text{vir}} = \frac{100}{G} H^2(z) R_{\text{vir}}^3 = \frac{V_{\text{vir}}^3}{10 G H(z)} \quad (2.61)$$

where  $H(z)$  is the Hubble constant at  $z$ ,  $R_{\text{vir}}$  the virial radius and  $V_{\text{vir}}$  the virial velocity. There are  $17.7 \times 10^6$  FOF groups at  $z = 0$  and a maximum of  $19.8 \times 10^6$  at  $z = 1.4$  when groups were more abundant. At  $z = 0$ , the groups contain  $18.2 \times 10^6$  subhaloes and the largest FOF group contains 2328 subhaloes. The FOF groups contain at least 20 particles. We can now build merging trees to characterise the evolution of structure. For each halo there can be more than one progenitor but there is only one descendant. The entire merger tree is obtained by defining a unique descendant for each halo and subhalo. We show in Figure (2.9) the organization of the merger tree in the Millennium Run.

## 2.6.4 Semi-analytic model of galaxy formation and evolution

The semi-analytic model is a simplified simulation of galaxy formation and evolution. In the model, star formation and the associated feedback processes are parameterised with simple analytic physical models. The resulting differential equations describe the cooling processes in gas, star formation, supernovae and AGN feedback, growth of supermassive black holes

---

<sup>3</sup>FOF groups are equivalence classes where any pair of two particles is placed into the same group if their mutual separation is less than 0.2 of the mean particle separation (Davis et al. (1985) [35]).

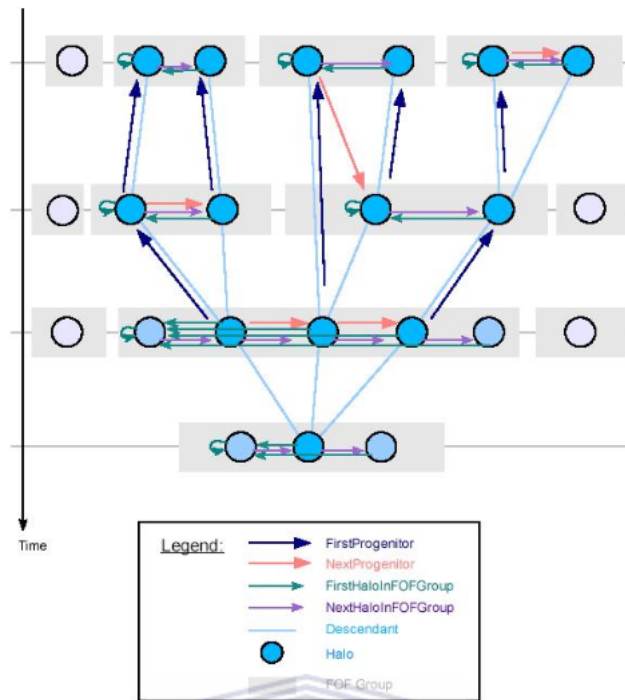


**Figure 2.9:** Organization of the merger tree in the Millennium Run (source: <http://www.gvo.org/MyMillennium/pages/help/HelpSingleHTML.jsp#simulation>).

and reionization from UV background. One can model as well galaxy morphology transformation shaped by galaxy mergers, galaxy metal enrichment processes and the effect of dust extinction (Kauffmann et al. (1999) [53]).

We now describe as in Croton et al. (2005) [32] the baryonic physics of the formation and evolution of galaxies in a particular model. As the model operates on the stored database of merger trees the effects of parameter variations within the model can be explored with a little computational expense. The simulation and the post-processing at earlier stages do not need to be repeated. We review in the following the modelling of the gas cooling, black hole growth and galaxy morphology that are directly relevant to our project. More details in the modelling of star formation, supernovae feedback, reionization, metal enrichment and dust obscuration can be found in Croton et al. (2005) [32].



## Gas cooling

We follow the description of the gas infall and cooling set out by White & Frenk (1991) [121] and adapted for implementation on N-body simulations by Springel et al. (2001) [108] and De Lucia et al. (2004) [37].

The model assumes that dark matter halo collapses under gravity and the cosmic baryons collapse with it. The baryons are in the form of diffuse gas but later in time they include gas in different phases. They can also be in the form of stars and include heavy elements. The evolution of the infalling gas is a function of redshift and the depth of the halo potential (Silk (1977) [100], Rees et al. (1977) [89], Binney (1977) [9] and White & Rees (1978) [122]). The processes of how gas cools in halos depend on the mass of the systems and the time episode.

- At late times and in massive systems the gas shock heats to the *virial temperature*<sup>4</sup> which results in the formation of a quasi-static hot atmosphere that extends to the *virial radius*<sup>5</sup>.
- At early times and in lower mass systems the infalling gas shocks as well to the virial temperature but since its cooling time is relatively short a quasi-static hot atmosphere cannot form. The shock of the gas occurs at smaller radii and gas cools rapidly onto the central region of the halo and forms a disk of cold gas. If the disk is gravitationally unstable it can lead to star formation.

The cooling time of the gas  $t_{\text{cool}}$  is defined as the ratio of its specific thermal energy to the cooling rate per unit volume:

$$t_{\text{cool}} = \frac{3}{2} \frac{\bar{\mu} m_{\text{p}} kT}{\rho_{\text{g}}(r)\Lambda(T, Z)} \quad (2.62)$$

where  $\bar{\mu} m_{\text{p}}$  is the mean particle mass,  $k$  the Boltzmann constant,  $\rho_{\text{g}}(r)$  the hot gas density and  $\Lambda(T, Z)$  the cooling function which depends on the temperature  $T$  and the gas metallicity

<sup>4</sup>The *virial temperature* is the temperature of the system at which the virial theorem holds. It states that during the collapse of gas mass system under gravity half of the gravitational energy is converted into thermal energy.

<sup>5</sup>The *virial radius* is the radius of the halo within which the virial equilibrium holds. It is often approximated by the radius  $r_{200}$  within which the mean density is at least 200 times the critical density  $\rho_{\text{c}} = \frac{3H^2}{8\pi G}$ .

$Z$ . In the model the temperature of the infalling gas after shock is assumed to be the virial temperature of the halo given by

$$T = 35.9 \left( \frac{V_{\text{vir}}}{1 \text{ km s}^{-1}} \right)^2 \text{ K.} \quad (2.63)$$

The static hot gas atmosphere is assumed to have an isothermal distribution

$$\rho_{\text{g}}(r) = \frac{m_{\text{hot}}}{4\pi R_{\text{vir}} r^2} \quad (2.64)$$

where  $m_{\text{hot}}$  is the total hot gas mass in the halo that extends to its virial radius  $R_{\text{vir}}$ . We now estimate the cooling rate of the hot gas onto the centre of the halo by defining the cooling radius  $r_{\text{cool}}$ . This is defined as the radius at which the cooling time is equal to a suitably defined age for the halo. White & Frenk (1991) [121] assume that this age is equal to the Hubble time  $t_{\text{H}}$ <sup>6</sup>. Cole et al. (2000) [25] assume that this time is equal to the time scale during which the main progenitor last doubled its mass. Somerville & Primack (1999) [103] assume that the cooling time is the time interval since the last major merger.

Here we follow the definition given by Springel et al. (2001) [108] and De Lucia et al. (2004) [37]. The cooling radius is the point where the local cooling time is equal to the halo dynamical time

$$t_{\text{d}} = \frac{R_{\text{vir}}}{V_{\text{vir}}} \quad (2.65)$$

$$= \frac{0.1}{H(z)} \quad (2.66)$$

which is smaller (by a factor of 3) than the Hubble time  $t_{\text{H}}$ . This results in smaller radii and smaller cooling rates if compared to White & Frenk (1991) [121]. The choice is however justified by a good agreement between the predicted amount of condensed gas in galaxy haloes and the amount which is actually condensed in the high resolution Smoothed Particle Hydrodynamic (SPH) simulations of Yoshida et al. (2002) [131].

---

<sup>6</sup>The *Hubble time* is an estimate of the maximum age of the universe. If we assume  $H = 73 \text{ km s}^{-1} \text{ Mpc}^{-1}$ ,  $t_{\text{H}} \simeq \frac{1}{H} \simeq 13.7 \text{ Gyr}$ .

The cooling rate takes the following form through a continuity equation using the above definition:

$$\dot{m}_{\text{cool}} = 4\pi\rho_{\text{g}}(r_{\text{cool}}) r_{\text{cool}}^2 \dot{r}_{\text{cool}}. \quad (2.67)$$

This is a good approximation to the rate at which gas falls onto the centre, obtained by Bertschinger (1989) [8] in his similarity solution for a cooling flow. Then the cooling rate can be written as

$$\dot{m}_{\text{cool}} = 0.5m_{\text{hot}} \frac{r_{\text{cool}}V_{\text{vir}}}{R_{\text{vir}}^2}. \quad (2.68)$$

This equation is valid when  $r_{\text{cool}} < R_{\text{vir}}$ . This condition set by White & Frenk (1991) [121] separates the static hot halo regime from the rapid cooling regime.

A rapid cooling regime occurs if the cooling radius is outside the virial radius ( $r_{\text{cool}} > R_{\text{vir}}$ ). In this case the post-shock gas cools in less than one sound crossing time. At large radius, infall simulations show that the accretion shock moves inwards since the gas pressure is not enough to support the accretion shock. The post-shock gas cools rapidly onto the central disk so that the mass contained in the post-shock hot gas atmosphere decreases while the temperature of the post-shock gas increases. This results in a rapid accretion of infalling material onto the central disk of the halo. The formation and evolution of galaxies in semi-analytic models are shown in Figure (2.10).

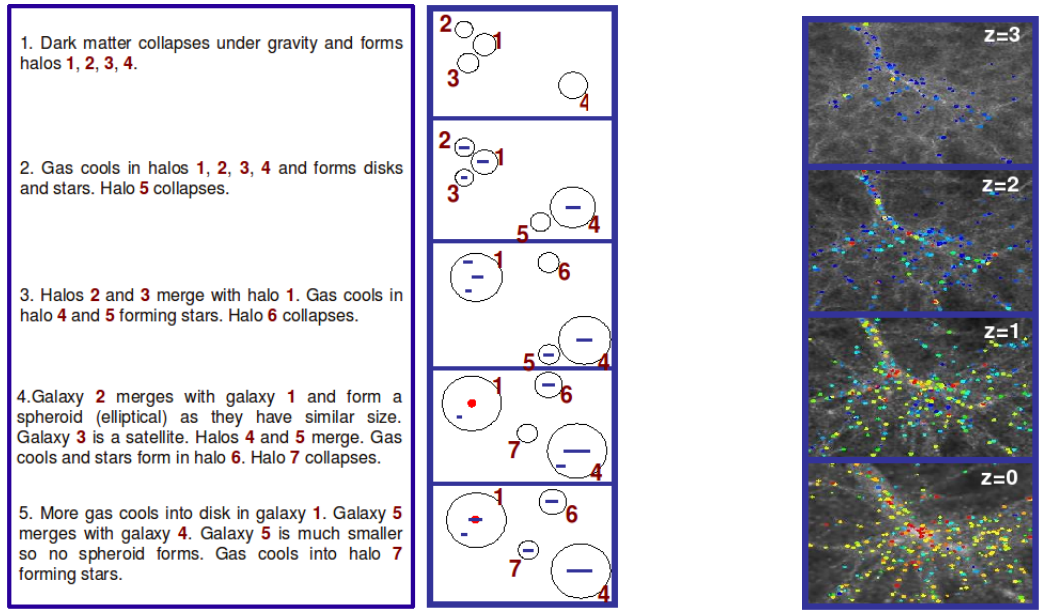


**Figure 2.10:** The left panel shows the galaxy formation and evolution in semi-analytical models. The right panel shows the population of simulated galaxies superposed on dark-matter particles (grey-coloured) in a region of  $21 \times 21 \times 8 \text{ (Mpc} \cdot h^{-1})^3$ . The galaxies are represented with coloured circles which are coded in accordance with their star formation rate that increases from the sequence red, yellow, green and blue. At early times (top panel  $z = 3$ ) stars are forming with only few galaxies. Later on, from  $z = 3$  to  $z = 0$ , more galaxies form with new stars but at the same time some of them run out of gas and they turn green, yellow and red. At the present time ( $z = 0$ ), we can see that red galaxies associated with old stars are found in the central region of the cluster and blue galaxies with blue young stars populate the outskirts of the system. This is very similar to the observations (credit: Colberg J. and Diaferio A., source: <http://www.mpa-garching.mpg.de/GIF/#ref>).

## 2.6.5 Millennium Database

### Snapshots

The information about the snapshot is stored in this table and the relation that links the redshifts with the lookback times. Instead of considering the redshift of the galaxies that we are interested in we extracted their properties by using the corresponding snapshot which facilitates their identification. For this we need to know the redshift at which the snapshot given by the column `snapnum` corresponds to. We give in Table (2.3) the properties that we used for the table `Snapshots`.

**Table 2.3:** *Information used from the table Snapshots.*

Column	Type	Description
snapnum	integer	The order of the snapshot from 0 to 63 ( $z = 0$ )
$z$	double	The redshift in full precision
lookBackTime	float	The lookback time in $10^9$ years

### DeLucia2006a

We used the database MPAGalaxies which stores the output of the Millennium simulation's MPA halo merger trees. We extracted the galaxy and halo properties from the table DeLucia2006a which is shown in Table (2.4). The table DeLucia2006a contains the result of the L-Galaxies<sup>7</sup> run on the Millennium merger trees. The parameters used are the same as in the Millennium Run described in DeLucia and Blaizot (2006) [36].

**Table 2.4:** *Information used from the table DeLucia2006a.*

Column	Unit	Description
galaxyId		Id of the galaxy
fofId		Id of the sub-halo at the centre of FOF this galaxy resides in
subhaloId		Id of the sub-halo this galaxy resides in
stellarMass	$10^{10}h^{-1}M_{\odot}$	Mass in stars
blackHoleMass	$10^{10}h^{-1}M_{\odot}$	Mass of the central black hole
centralMvir	$10^{10}h^{-1}M_{\odot}$	Virial mass of the background (FOF) halo containing this galaxy
$x$	1/h Mpc	$x$ -component position
$y$	1/h Mpc	$y$ -component position
$z$	1/h Mpc	$z$ -component position

### 2.6.6 Summary

The Millennium simulation was built to study the interactions of particles under the influence of gravitational force. It assumes dark matter particles with zero pressure. The formation

<sup>7</sup>L-Galaxies is the name of the semi-analytical algorithm used at MPA.

and evolution of galaxies can be simulated with the dark matter structures using semi-analytic models. The history of galaxy mergers can be traced by constructing a merger tree. The database stores essential information about the properties of galaxies and halos and we can make a query to get the parameters that we need such as the black hole mass, the position of the galaxies and eventually the virial mass of the halo hosting the galaxy. This can be done by using a Structured Query Language (SQL).

## 2.7 AGN feedback

### 2.7.1 Introduction

In this section we present a model for the growth of black holes in galaxies as it is described in Croton et al (2005) [32]. We review the different accretion modes in AGN feedback and identify the types of active nuclei triggered by each mode of accretion onto the supermassive black hole. Then we discuss how efficient the energy production is by considering the accretion efficiency parameter which also controls the rate of black hole mass change. We give some estimates of the accretion efficiency obtained from observations while the exact determination of its value remains uncertain due to its dependency on the luminosity of the host galaxy, the redshift, the mass and eventually the spin of the black hole.

### 2.7.2 Radio mode accretion

The *radio mode accretion* is the result of the accretion of hot gas onto the central supermassive black hole. It occurs after the formation of a static hot halo around the galaxy that hosts the black hole. Assuming a continual and quiescent accretion, the radio mode accretion can be described by:

$$\dot{m}_{\text{BH,R}} = \kappa_{\text{AGN}} \left( \frac{m_{\text{BH}}}{10^8 M_{\odot}} \right) \left( \frac{f_{\text{hot}}}{0.1} \right) \left( \frac{V_{\text{vir}}}{200 \text{ kms}^{-1}} \right)^3. \quad (2.69)$$

In the above equation  $m_{\text{BH}}$  is the mass of the black hole,  $f_{\text{hot}}$  the fraction of the total halo mass in the form of hot gas and  $V_{\text{vir}}$  is the virial velocity of the halo which is proportional

to the square root of the virial temperature  $T_{\text{vir}}$  ( $V_{\text{vir}} \propto T_{\text{vir}}^{\frac{1}{2}}$ ). The free parameter  $\kappa_{\text{AGN}}$  is used to control the accretion efficiency. A value  $\kappa_{\text{AGN}} = 6 \times 10^{-6} M_{\odot} \text{ yr}^{-1}$  can reproduce precisely the turnover at the bright end of the galaxy luminosity function (Croton et al (2005) [32]). We can see from equation (2.69) that the mass accretion rate is proportional to the black hole mass and the fraction of hot gas mass from the halo which is much significant compared to the amount of accreting hot gas mass coming from the disk surrounding the black hole and the bulge of the galaxy. The term  $f_{\text{hot}} V_{\text{vir}}^3 t_{\text{H}}$  where  $t_{\text{H}}$  is the Hubble time, is proportional to the total mass of hot gas. Hence the above given formula is the product of the mass of the hot gas and the black hole mass multiplied by a constant efficiency and divided by the Hubble time  $t_{\text{H}}$ . Basically  $\dot{m}_{\text{BH,R}}$  depends little on the fraction  $f_{\text{hot}}$  since it is approximately constant for  $V_{\text{vir}} \geq 150 \text{ km s}^{-1}$ . In our modelling we need to understand when each mode of AGN feedback becomes important. For the radio mode accretion, as described in Croton et al (2005) [32], it is assumed that the feedback injects enough energy in the surrounding medium to reduce or eventually quench cooling flows. This energy can be expressed as a mechanical heating which is generated by the black hole accretion. It is given by:

$$L_{\text{BH}} = \eta \dot{m}_{\text{BH}} c^2, \quad (2.70)$$

$\eta$  is the efficiency with which mass is assumed to produce energy near the event horizon and  $c$  the speed of light. The injection of this heating energy produces an infall rate of the cooling as follows:

$$\dot{m}'_{\text{cool}} = \dot{m}_{\text{cool}} - \frac{L_{\text{BH}}}{\frac{1}{2} V_{\text{vir}}^2} \quad (2.71)$$

where  $\dot{m}_{\text{cool}}$  is the cooling rate within a halo that contains hot gas atmosphere. It is given by:

$$\dot{m}_{\text{cool}} = 0.5 m_{\text{hot}} \frac{r_{\text{cool}} V_{\text{vir}}}{R_{\text{vir}}^2}. \quad (2.72)$$

The cooling radius  $r_{\text{cool}}$  is defined as the radius at which the local cooling time is for example equal to the Hubble time  $t_{\text{H}}$  (halo dynamical time). This time according to White & Frenk (1991) [121], is a suitable age for the halo.  $m_{\text{hot}}$  is the mass of the total hot gas associated with the halo. This hot gas mass is assumed to extend to its virial radius  $R_{\text{vir}}$ . The infall

rate  $\dot{m}_{\text{cool}}$  is supposed to be positive at all times. We have:

$$\dot{m}_{\text{cool}} \sim f_{\text{hot}}^{\frac{3}{2}} \Lambda(V_{\text{vir}})^{\frac{1}{2}} V_{\text{vir}}^2 t_{\text{H}}^{-\frac{1}{2}} \quad (2.73)$$

and

$$\dot{m}_{\text{heat}} = \frac{2L_{\text{BH}}}{V_{\text{vir}}^2} \sim m_{\text{BH}} f_{\text{hot}} V_{\text{vir}}. \quad (2.74)$$

Hence

$$\frac{\dot{m}_{\text{heat}}}{\dot{m}_{\text{cool}}} \sim \frac{m_{\text{BH}} t_{\text{H}}^{\frac{1}{2}}}{f_{\text{hot}}^{\frac{1}{2}} \Lambda(V_{\text{vir}})^{\frac{1}{2}} V_{\text{vir}}}. \quad (2.75)$$

This means that radio mode accretion is effective in suppressing cooling flow at late times (low redshift) and for massive black holes. We model FRI-type radio galaxies using radio mode accretion. These low-luminosity sources are triggered by hot gas accretion onto the central black hole but with low accretion efficiency ( $\leq 10^{-5}$ ).

### 2.7.3 Quasar mode accretion

The *quasar mode accretion* is the result of the merging of galaxies and also the accretion of cold disk gas (Croton et al. (2005) [32]). The black hole is modelled as the sum of progenitor masses neglecting the losses from gravitational waves. We assume that the accreting gas mass during the merging of the galaxies is proportional to the total cold gas present in the system. The accretion efficiency during this process is lower for systems with lower mass and for unequal mergers. The amount of gas mass during the accretion can be expressed as:

$$\Delta m_{\text{BH,Q}} = \frac{f'_{\text{BH}} m_{\text{cold}}}{1 + \left(\frac{280 \text{ km s}^{-1}}{V_{\text{vir}}}\right)^2} \quad (2.76)$$

where

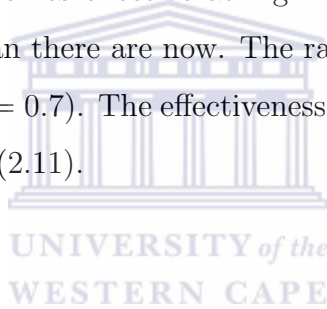
$$f'_{\text{BH}} = f_{\text{BH}} \frac{m_{\text{sat}}}{m_{\text{central}}}. \quad (2.77)$$

The constant  $f_{\text{BH}} \simeq 0.03$  is chosen to reproduce the observed local  $m_{\text{BH}}-m_{\text{bulge}}$  relation (Magorrian et al. (1998) [60], Marconi et al. (2003) [62]). Major merger is defined by having at least two progenitors of mass greater than 0.2 times the descendant mass. Black hole accretion is allowed during major and minor mergers. The contribution of minor mergers is



small because of the term  $\frac{m_{\text{sat}}}{m_{\text{central}}}$  so the accretion of major mergers is the dominant mode of growth of the central black hole in quasar mode accretion. In our model, we apply the quasar mode accretion to blazars and FR II radio galaxies. Flat spectrum sources (eg. high luminosity blazars) are considered to be the same objects as steep spectrum sources just viewed along the line of sight. The average accretion efficiency is taken to be 0.1 but according to the literature (Marulli et al. (2008) [65]) it probably depends on the black hole mass, its luminosity and also the redshift. Our model does not include radiative feedback from optical, UV and X-ray AGN as well as feedback associated with starbursts and supernovae. A more detailed treatment of black hole growth and a build-up of its population can be found in Springel et al. (2005) [106].

The quasar mode accretion becomes effective at high redshift ( $z \geq 1$ ) because there were more mergers at early times than there are now. The radio mode accretion is more efficient at low redshift (at least up to  $z = 0.7$ ). The effectiveness of the black hole growth at different redshift is illustrated in Figure (2.11).



## 2.7.4 Accretion efficiency

### Introduction

Our modelling requires understanding of the accretion of matter onto the supermassive black hole in the centre of galaxies. When matter falls onto a black hole of a radius  $R$  it gains kinetic energy (KE) in exchange for potential energy. If  $m$  is the accreting mass falling from infinity to a distance  $r$  from the black hole centre the potential energy of the mass is transformed into KE as:

$$\frac{1}{2}mv^2 = \frac{GMm}{r} \quad (2.78)$$

where  $v$  is the velocity of the infalling material of mass  $m$ ,  $M$  the mass of the central black hole and  $G$  the gravitational constant. When the mass hits the accretion disk near the black hole the kinetic energy is dissipated into heat and appears in some form of radiation. As

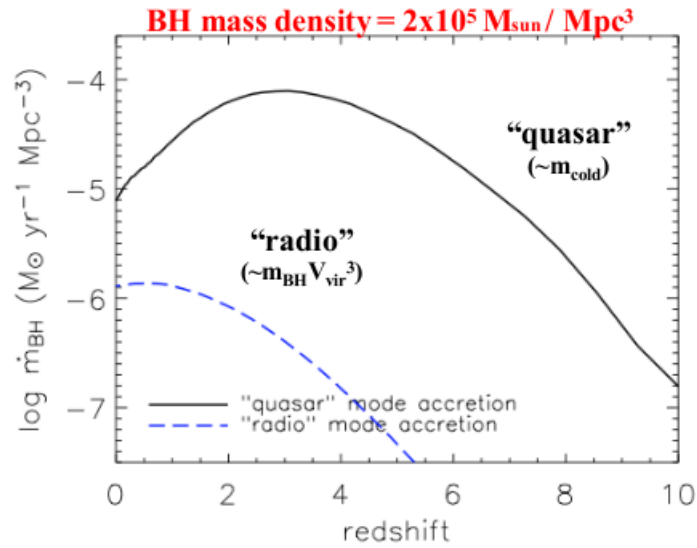


**Figure 2.11:** The black hole accretion rate density  $\dot{m}_{\text{BH}}$  as a function of redshift  $z$ . The solid line represents the quasar mode accretion which is more efficient at late time (high redshift): it falls down rapidly for  $z \leq 2$ . The dashed line is the radio mode accretion which is more efficient at low redshifts whereas its contribution to the overall black hole mass is not very significant. The quasar mode accretion is more efficient than the radio mode accretion at all times (adopted from Croton et al. (2005) [32]).

the accretion rate is  $\frac{dm}{dt}$  the KE of the mass is converted into heating energy at a rate  $\frac{1}{2} \frac{dm}{dt} v^2$  which is defined as the luminosity of the heating source  $L$ .  $v$  is given by:

$$v = \sqrt{\frac{2GM}{R}}. \quad (2.79)$$

Hence

$$L = \frac{1}{2} \frac{dm}{dt} v^2 \quad (2.80)$$

$$= \frac{GM}{R} \frac{dm}{dt}. \quad (2.81)$$

We can express the luminosity  $L$  using the Schwarzschild radius of the black hole  $r_g$  given by:

$$r_g = 2 \frac{GM}{c^2}. \quad (2.82)$$

Then we get

$$L = \frac{1}{2} \frac{dm}{dt} c^2 \frac{r_g}{R} \quad (2.83)$$

$$L = \eta \frac{dm}{dt} c^2 \quad (2.84)$$

The parameter  $\eta$  is called *radiative efficiency* which is considered to be the efficiency of the conversion of the rest mass energy into radiation. Here we note the distinction between the radiative efficiency  $\eta$  and the *accretion efficiency*  $\varepsilon$  that we introduce in our modelling.

The accretion efficiency  $\varepsilon = \varepsilon(a)$  represents the maximum of potential energy that can be extracted, per unit rest mass energy from the matter that accretes onto the black hole (Merloni & Heinz (2008) [68]) where  $a$  is the spin of the black hole.  $\varepsilon(a)$  depends on the inner boundary condition of the accretion flow and is a function of the black hole spin  $a$  in the classical no-torque case (Novikov & Thorne (1973) [75]).  $\varepsilon(a)$  is ranging from  $\varepsilon(a = 0) \simeq 0.057$  for Schwarzschild non-spinning black holes to  $\varepsilon(a = 1) \simeq 0.42$  for Kerr black holes with maximal rotation.

The radiative efficiency  $\eta = \frac{L_{\text{bol}}}{\dot{M}c^2}$  depends on the accretion efficiency and the nature of the accretion flow. In our model  $\eta$  is related to  $\varepsilon$  by

$$\eta = \frac{\varepsilon}{1 - \varepsilon}. \quad (2.85)$$

### Eddington luminosity

We define now the Eddington luminosity in relation to the bolometric luminosity. We assume that a luminous object like a hot star has a mass to luminosity ratio  $\frac{M}{L}$ . If we consider a small mass of ionised matter near the central source at the distance  $r$  of its centre the radiation pressure force outward on the cloud is given by

$$F_{\text{rad}} = \frac{m\kappa L}{4\pi r^2 c} \quad (2.86)$$

where  $\kappa$  is the mass absorption coefficient (cross-section per unit mass) of the ionised cloud. The same mass of cloud experiences an inward force due to the gravitation:

$$F_{\text{grav}} = G \frac{mM}{r^2}. \quad (2.87)$$

The Eddington luminosity is the luminosity where the two forces balance.

$$L_{\text{Edd}} = \frac{4\pi GcM}{\kappa}. \quad (2.88)$$

Hence beyond this luminosity limit the central mass ejects material spontaneously and the cloud is blown away by the radiation pressure. The Eddington factor is defined as the ratio of the bolometric luminosity to the Eddington luminosity:

$$f_{\text{Edd}} = \frac{L_{\text{bol}}}{L_{\text{Edd}}}. \quad (2.89)$$

The accretion efficiency and the Eddington factor are the most important parameters that influence our simulation model. However they are not yet well constrained by observations. The range of the radiative accretion efficiency  $\eta$  for example is from 0.01 in a standard radiatively efficient thin disk to  $10^{-11}$  for a spherically symmetric accretion from a low density medium (Shakura & Sunyaev (1973) [98], Shapiro (1973) [99], Meszaros (1975) [69], Soltan (1982) [102], Yu & Tremaine (2002) [133]). As discussed in Kurosawa et al. (2009) [56] a radiative accretion efficiency  $\eta = 0.1$  is assumed and fixed by many authors (Springel et al. (2005) [105], Di Matteo (2005) [38], Booth & Schaye (2009) [16], Shakura & Sunyaev (1973) [98], Soltan (1982) [102]). Thorne (1974) [114] assumed that in an accretion model with a thin disk and a rapidly rotating black hole  $\eta \sim 0.2$ .

We give in Table (2.5) some range of the radiative efficiency  $\eta$  obtained from some recent observations. We can see in Figure(2.12) that the radiative efficiency depends essentially on the source. Here Wang et al. (2006) [119] consider a sample of three quasars from the Sloan Digital Sky Survey Data Release 1 (SDSS DR1). It shows that the same type of radio quasars can have different radiative accretion efficiency at a given cosmic time because of

**Table 2.5:** Recent estimates of the radiative efficiency  $\eta$ .

Radiative efficiency $\eta$	Reference
0.7	Martínez-Sansigre & Taylor (2009) [63]
0.30 – 0.35	Wang et al. (2006) [119]
0.16	Yu & Lu (2008) [132]
0.15	Elvis et al. (2002) [40]
$\sim 0.1$ or $\sim 0.2$	Yu & Tremaine (2002) [133]
$\sim 0.08$ for $M_{\text{BH}} < 10^8 M_{\odot}$ and $\gtrsim 0.18$ for $M_{\text{BH}} \gtrsim 10^9 M_{\odot}$	Cao & Li (2006) [20]

the difference of their luminosity, black hole mass and spin.

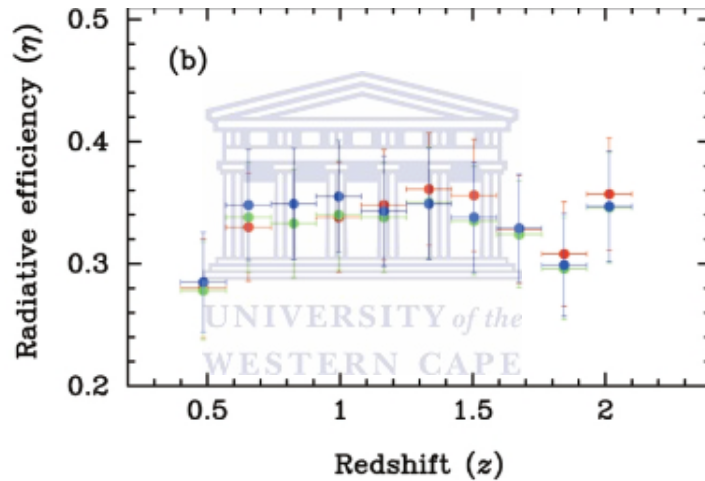


**Figure 2.12:** Radiation efficiency as a function of redshift for three quasars sample  $S_1$ ,  $S_2$  and  $S_3$  from SDSS DR1. The error bars are dominated by the uncertainty in black hole masses (adopted from Wang et al. (2006) [119]).

### 2.7.5 Summary

We have seen in this section that radio mode accretion is efficient at low redshift and for massive black holes ( $M \geq 10^8 M_{\odot}$ ). In our model the population of low luminosity FRI and BL Lacs are triggered by this mode when static hot gas halos form around the host galaxy. They undergo radiatively inefficient accretion. At high redshift ( $z \gtrsim 1$ ) the quasar mode accretion is the dominant mechanism of black hole growth when the central black hole

accretes sufficient cold gas mass induced by mergers. The population of high luminosity FR II and blazars are triggered by this mode. In our model we take the standard accretion efficiency  $\varepsilon = 0.1$  at all redshift (Marulli et al. (2008) [65]) in quasar mode accretion since this parameter is not yet well constrained. It is important to notice however that some dynamical model (Croton (2006) [31]) suggests an accretion efficiency that increases with redshift and Mo et al. (1998) [71] provided a physical justification of this assumption.



# Chapter 3

## Methodology

### 3.1 Introduction

We now introduce the modelling of the radio emission from AGN using galaxies extracted from the Millennium box. For consistency with the Millennium simulation we adopt the following flat cosmology model with  $h=H_0/100 \text{ km/s/Mpc}=0.73$  (Hubble parameter),  $\Omega_m = 0.25$  (density of matter) and  $\Omega_\Lambda = 0.75$  (density of dark energy). We use the output of the model of the DeLucia2006a catalogue for the simulation. In their model De Lucia and Blaizot (De Lucia & Blaizot (2006) [36]) assumed that for each merger the black hole (BH) accretes mass instantaneously and the BH seed masses are set to zero. We add to their model a follow up of the BH mass accretion rate and its conversion to radiation (Marulli et al. (2007) [64], Marulli et al. (2008) [65]).

We compute the space density of AGN radio sources as a function of redshift in the Millennium volume and compare the results with observations. In practice, we compare our results with models which fit recent observations.

We model flat spectrum as well as steep spectrum radio sources but we focus mainly our attention on flat spectrum BL Lacs and brighter blazars since they are the most important sources of radio contamination of the CMB. This is due to the particular orientation of their

jets which are close to our line of sight.

### 3.2 Modelling the radio mode accretion

The radio mode accretion is effective at low redshift ( $z < 1$ ). We determined the number density of FRI radio galaxies (steep spectrum) and BL Lacs (flat spectrum) up to the average redshift  $z=1.03$  using the method described in this section.

In the Croton et al. (2005) [32] model of radio mode accretion, large galaxies with a significant fraction of hot gas in their halos generate feedback, the idea being that AGN activity could be initiated by the gas accreting onto the central black hole and the resulting FRI-type jets would then heat the surrounding gas. Here, we model FRI-type radio galaxies with somewhat different picture in mind: we assume that any growth in the central black hole mass will generate radio emission, but we assume that the radio emission is "switched on" with a duty cycle which we estimate from observations. The radio luminosity is tied to the amount of mass accreted onto the black hole within a given snapshot time and typically the luminosities are so low that they fall well below the flux density cutoff of interest.

For all galaxies in the Millennium box at a redshift  $z_1$  we extract the corresponding progenitors at later redshift  $z_2$ . We determine the black hole mass accretion rate between the two snapshots (at  $z_1$  and  $z_2$ ) which is given by:

$$\frac{dM_{\text{BH}}}{dt} = \frac{M_{\text{BH}}(\text{descendant}) - M_{\text{BH}}(\text{progenitor})}{t_1 - t_2} \quad (3.1)$$

where  $M_{\text{BH}}(\text{descendant})$  is the descendant black hole mass at  $z_1$  and  $M_{\text{BH}}(\text{progenitor})$  its progenitor at  $z_2$  in the merger tree,  $t_1$  and  $t_2$  the lookback times corresponding to the redshifts  $z_1$  and  $z_2$  that we can extract from the table of Snapshots. This accretion rate  $\dot{M}_{\text{BH}}$  is related to the total bolometric luminosity as:

$$L_{\text{bol}} = \frac{\varepsilon}{1 - \varepsilon} \dot{M}_{\text{BH}} c^2 \quad (3.2)$$



where  $\varepsilon$  is the accretion efficiency and  $c$  the speed of light. The value of  $\varepsilon$  is not yet well constrained since it depends on the redshift, luminosity and the mass of the central black hole. We know from some observations (Cao (2003) [19], Kurosawa et al. (2009) [56]) that the accretion is relatively inefficient for low luminosity radio galaxies (FRI) and low luminosity blazars (BL Lacs) so that  $\varepsilon$  is very small ( $\varepsilon \leq 10^{-4}$ ). We derive the luminosity in the radio band from the bolometric luminosity by assuming that a fraction  $f_{\nu_o}$  of the bolometric luminosity is converted to radio luminosity  $L_{\nu_o}$ :

$$L_{\nu_o} = f_{\nu_o} L_{\text{bol}} \quad (3.3)$$

where the fraction  $f_{\nu_o}$  can be obtained from the spectral energy distribution (SED) of the radio galaxies. The expression of  $f_{\nu_o}$  is given by:

$$f_{\nu_o} = \frac{\int_{\nu_o - \frac{\Delta\nu}{2}}^{\nu_o + \frac{\Delta\nu}{2}} \frac{\nu L_\nu}{\nu} d\nu}{\int_{\nu_{\min}}^{\nu_{\max}} \frac{\nu L_\nu}{\nu} d\nu} \quad (3.4)$$

where  $\Delta\nu$  is the bandwidth of the survey centred at the frequency  $\nu_o$  and  $\nu_{\min}$ ,  $\nu_{\max}$  are respectively the minimum and maximum frequency read in the SED of the source and  $L_\nu$  the luminosity at the frequency  $\nu$ . The luminosity  $L_{\nu_o}$  is related to the flux density of the radio source  $S$  by:

$$L_{\nu_o} = f_{\nu_o} L_{\text{bol}} \quad (3.5)$$

$$= 4\pi \Delta\nu d_L^2 S \quad (3.6)$$

where  $d_L$  is the luminosity distance of the radio source at the redshift  $z$ . Hence we obtain

$$f_{\nu_o} L_{\text{bol}} = 4\pi \Delta\nu d_L^2 S \quad (3.7)$$

$$f_{\nu_o} \frac{\varepsilon}{1 - \varepsilon} \dot{M}_{\text{BHC}} c^2 = 4\pi \Delta\nu d_L^2 S \quad (3.8)$$

$$S = \frac{\varepsilon}{1 - \varepsilon} \frac{f_{\nu_o} \dot{M}_{\text{BHC}} c^2}{4\pi \Delta\nu d_L^2} \quad (3.9)$$

Now we count the radio galaxies above a given flux cut-off,  $S_{\text{cut}}$ , that satisfy the following condition:

$$S > S_{\text{cut}} \quad (3.10)$$

$$\dot{M}_{\text{BH}} > \frac{(1 - \varepsilon) 4\pi \Delta\nu d_L^2 S_{\text{cut}}}{\varepsilon c^2 f_{\nu_o}}. \quad (3.11)$$

To test the model we choose a small enough flux cut-off  $S_{\text{cut}} = 1$  mJy to include fainter sources in the simulation. We count only the radio sources inside the sphere centered on the Millennium box at the mean redshift  $z$  of the redshifts  $z_1$  and  $z_2$  of the snapshots. The comoving volume of this sphere is given by:

$$V = \frac{4}{3}\pi r_{\text{sphere}}^3 \quad (3.12)$$

where  $r_{\text{sphere}}$  is the radius of the sphere. From there we can compute the space density as:

$$\rho = \frac{\text{number of radio sources}}{V}. \quad (3.13)$$

### 3.3 Modelling the quasar mode accretion

As we have seen in the chapter of AGN feedback (Section (2.7)), quasar mode accretion is more efficient at high redshift ( $z > 1$ ) where galaxies undergo more frequently major mergers. In this case the galaxy in the box has at least two progenitors of stellar mass greater than 0.2 times the descendant stellar mass. When we compute the black hole mass accretion rate, we use the following formula:

$$\frac{dM_{\text{BH}}}{dt} = \frac{M_{\text{BH}}(\text{descendant}) - M_{\text{BH}}(\text{max})}{t_1 - t_2} \quad (3.14)$$

where  $M_{\text{BH}}(\text{max})$  is the maximum of the two progenitor black hole masses. Then we repeat the same procedures as in the radio mode accretion for the calculation of the space density of quasars (steep spectrum) and blazars (flat spectrum radio quasars FSRQ). We give a summary of the method below.

- Choose radio mode accretion or quasar mode accretion.
- Introduce the cosmological model. For the Millennium simulation the parameters used are those given in Table (2.2) of Section (2.6.4).
- Take the average redshift  $z$  of the galaxies between the two snapshots where the black hole rate should be computed. The redshifts at the two snapshots will give the corresponding lookback time.
- Assign a random number between 0 and 100 to decide if an AGN is in a radio-loud phase. We use this random number to obtain the percentage of radio-loud sources which can be estimated from the duty cycle (Section (3.4)) of radio galaxies and quasars. It corresponds to the fraction of BL Lacs (flat spectrum) and FRI radio galaxies (steep spectrum) at lower luminosity, and blazars (flat spectrum) and FRII radio quasars (steep spectrum) at higher luminosity in the simulation.
- Set the flux cut-off  $S_{\text{cut}}$  or luminosity cut-off  $L_{\text{cut}}$  of the radio sources.
- Choose the value of the accretion efficiency  $\varepsilon(z, L, M_{\text{BH}})$  which depends on the redshift  $z$ , the luminosity of the black hole  $L$  and the black hole mass  $M_{\text{BH}}$ .
- Choose the SED of the source: BL Lacs, FRI (average power), blazars (average SED, low power and high power blazars), FRII, low redshift or high redshift radio-loud quasars and radio-quiet quasars. The template SED that we chose are:
  - HBL Mkn 421 at  $z = 0.031$  and HBL Mkn 501 at  $z = 0.034$  for BL Lacs objects.
  - FRI 3C 338 at  $z = 0.0304$ .
  - Average SED of blazars, low and high power blazars from Sparke & Gallagher (2007) [96].
  - RLQ (low and high redshift  $z$ ) and RQQ. We can neglect the contribution of RQQ since they are not significant for the contamination of SZ signals.

- Choose the frequency of the observation  $\nu_o$ : 151 MHz, 1.4 GHz, 2.7 GHz, 20 GHz, 30 GHz, 145 GHz, 220 GHz and 270 GHz. The frequencies 151 MHz, 20 GHz and 30 GHz are not currently used in our model but they were introduced in the code for a future perspective on the work as these frequencies are often used in some literatures which deal with the simulation of radio sources (e.g. Lin & Mohr (2007) [58], Sehgal et al. (2009) [97]).

- Compute the fraction of the converted radio luminosity using the formula:

$$f_{\nu_o} = \frac{\int_{\nu_o - \frac{\Delta\nu}{2}}^{\nu_o + \frac{\Delta\nu}{2}} \frac{\nu L_\nu}{\nu} d\nu}{\int_{\nu_{\min}}^{\nu_{\max}} \frac{\nu L_\nu}{\nu} d\nu}.$$

- Compute the comoving volume of the sphere  $V$ :

$$V = \frac{4}{3} \pi r_{\text{sphere}}^3 \quad (3.15)$$

where  $r_{\text{sphere}} = 250h^{-1}$  Mpc is the radius of the sphere within the Millennium box at the redshift  $z$  ( $h$  is the Hubble parameter).

- Compute the distance  $r$  of the galaxy from the centre of the previous sphere  $x_c$ ,  $y_c$  and  $z_c$  with the formula:

$$r = \sqrt{(x - x_c)^2 + (y - y_c)^2 + (z - z_c)^2}. \quad (3.16)$$

- If the galaxy is inside the sphere ( $r < 250$  Mpc), we proceed to the next step.
- Otherwise we compute the distance  $r$  of the next galaxy and repeat the above test.

- Compute the black hole mass accretion rate given by the following formula:

$$BH_{\text{accr}} = \frac{1 - \varepsilon}{\varepsilon} \frac{4\pi d_L^2 \Delta\nu S_{\text{cut}}}{c^2 f_{\nu_o}}. \quad (3.17)$$

- We compare it with the accretion rate  $\dot{M}_{\text{BH}}$  between two snapshots at redshifts  $z_1$  and

$z_2$ :

$$\dot{M}_{\text{BH}} = \frac{dM_{\text{BH}}}{dt} \quad (3.18)$$

$$= \frac{M_{\text{BH}}(z_1) - M_{\text{BH}}(z_2)}{t(z_1) - t(z_2)}. \quad (3.19)$$

- If  $\dot{M}_{\text{BH}} > BH_{\text{accr}}$ , then we count this radio source and give its position  $x, y, z$  in the sphere.
  - Otherwise compute the distance  $r$  for the next galaxy and repeat the same procedure until the last galaxy in the Millennium box.
- Compute the space density of the radio sources using the formula:

$$\rho = \frac{\text{number of radio sources}}{V}. \quad (3.20)$$

To make the comparison of the model with the best fit model of observed data we compute the redshift distribution  $\frac{dn}{dz}$  of radio galaxies and blazars as a function of the redshift  $z$  which is independent of the cosmology. It is given by:

$$\frac{dn}{dz} = \frac{dn}{dV} \frac{dV}{dz} \quad (3.21)$$

$$= \rho \frac{dV}{dz} \quad (3.22)$$

where  $\rho$  is the space density of the radio sources in the simulation and  $V$  the comoving volume.

$$\left(\frac{dn}{dz}\right)_{\Lambda\text{CDM}} = \left(\frac{dn}{dz}\right)_{\text{DeSitter}}. \quad (3.23)$$

We wrote the code corresponding to the flow chart in Figure (3.1) mainly in Fortran 77 whereas it contains some instructions in Fortran 90 since we use the compiler gfortran 95.

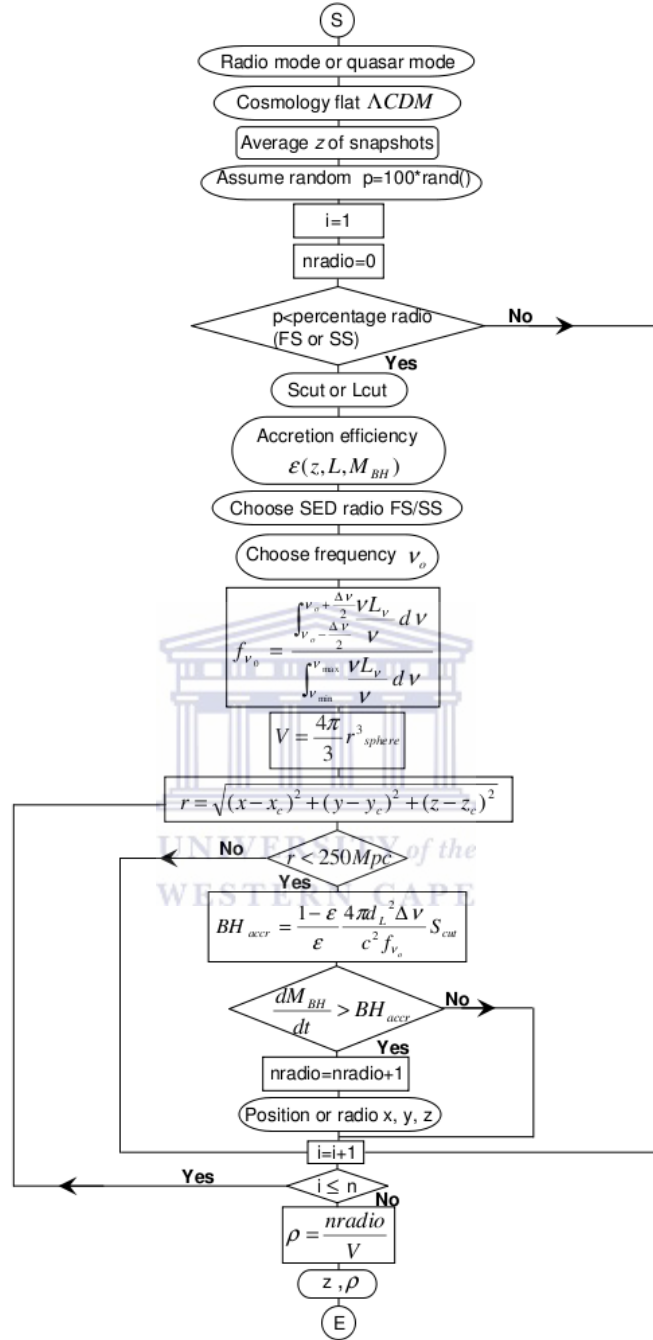


Figure 3.1: Flow chart of the model for computing the space densities of radio sources in radio mode accretion and quasar mode accretion.

We now describe in the following Section (3.4) the duty cycle of radio sources that we need for the calculation of the fraction of radio sources in our model.

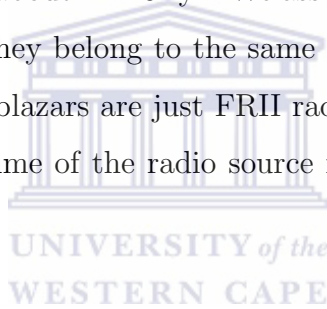
### 3.4 Duty cycle and lifetime

We have seen that we need to introduce in the model the fraction of galaxies that exhibits radio emission. For this we have to consider the notion of duty cycle and lifetime of AGN that we describe in the following.

The *duty cycle* is defined as the ratio (dimensionless) of the time of radio active to the sum of the time active and dormant. FRI and FRII radio galaxies are believed to live at most some tens of millions of year (Mack et al. (1998) [59], Kaiser (2000) [52]). The estimation of the ages are done by measuring the curvature in radio spectra caused by radiative energy losses of the higher energy electrons during the lifetime of the sources (Alexander et al. (1987) [1]). Radio sources have an important role in the heating of the ICM of clusters. This requires some balance between the duty cycle of repeated radio activity and heating efficiency as a function of the luminosity of the source (Worrall (2008) [126]). The duty cycle can be determined by searching a repeated radio activity in each source. Radio sources known as GHz-Peaked Spectrum (GPS) and Compact Steep Spectrum (CSS) are believed to be young. GPS and CSS radio sources are powerfull compact radio sources with peaks respectively near 1 GHz and 100 MHz. The GPS radio sources are contained within the extent of the narrow line region ( $< 1$  kpc) but CSS radio sources are contained within the host galaxy ( $< 15$  kpc). Sometimes their growth is stunted by the external medium (O' Dea (1998) [76]). Sources like the Compact Symmetric Object (CSO) are relatively young with ages less than  $10^4$  years (Conway (2002) [28]). CSO are radio sources which exhibit HI absorption toward the central parsecs (Peck & Taylor (2002) [82]). Since it is not common to see GPS sources with extended radio emission, it was argued (Stanghellini et al. (2005) [109]) that the periods between sustained activity are at least ten times longer than the lifetime of radio emission from the earlier activity. This is consistent with the time between FRIIs activity about  $5 \times 10^8$  yr and 1 Gyr. The latter estimation is done by cross correlating

optical and radio catalog coupled with an average source lifetime of  $1.5 \times 10^7$  yr obtained from the modelling of projected source lengths (Bird et al. (2008) [10]).

Parma et al. (1999) [80] discuss in their paper that the ages of FRIs are about  $10^7$  to  $10^8$  yr, and it is about 5 to 10 times larger than the ages of FRII radio galaxies. By assuming an average lifetime of  $1.5 \times 10^7$  yr for FRII (Bird et al. (2008) [10]), this gives us lifetimes between  $7.5 \times 10^7$  yr and  $1.5 \times 10^8$  yr for FRI. Here we compare their estimates with other studies since the results of the model will depend strongly on the choice of this parameter. At lower redshifts FRIs dominate the population of radio sources where they are likely triggered by the radio mode accretion. Miller et al. (2003) [70] suggest that at  $0.05 \leq z \leq 0.95$  the fraction of galaxies that show AGN signature may be as high as 40% which corresponds to a lifetime about  $2 \times 10^8$  yr. We assume the same duty cycles for blazars and FRII radio galaxies since they belong to the same population of radio sources (unified model of AGN, Section (2.2)): blazars are just FRII radio galaxies viewed along the line of sight of the observer. The lifetime of the radio source is independent of the orientation of the jet.



### 3.5 Estimation of the fraction of radio sources

We now determine the expected fraction of radio galaxies and quasars in the simulation by using the duty cycle and lifetime of these radio sources. In the study we estimate the fraction of both flat spectrum (BL Lacs, blazars) and steep spectrum (FRI and FRII) radio sources. The fraction gives the number of radio sources with respect to the number of galaxy in the simulation at a given redshift which is the average redshift of the snapshots. We need this fraction to estimate the number of galaxies that are radio active.

#### Fraction of radio galaxies in the radio mode accretion model

The average lifetime estimate of FRI (Miller et al. (2003) [70]) is about  $2 \times 10^8$  yr = 0.2 Gyr. Since the average time step in the simulation is about 0.3 Gyr the fraction of AGN in the



Millennium box that should be identified as FRI radio galaxies is  $\frac{0.2 \text{ Gyr}}{0.3 \text{ Gyr}} = 0.66 \simeq 70\%$ . Dunlop & Peacock (1990) [39] discuss the number of steep spectrum and flat spectrum radio galaxies and quasars. From their model of RLF (Figure (3.2)) we can see that there are about 10 times more steep spectrum than flat spectrum radio sources. This means that the expected flat spectrum BL Lacs in the simulation is about  $70\% \times \frac{1}{10} = 7\%$  (precisely  $0.66 \times \frac{1}{10} = 66\% \times \frac{1}{10} = 6.6\%$ ). We use this fraction in the model to compute the number density of low luminosity flat spectrum blazars (BL Lacs).

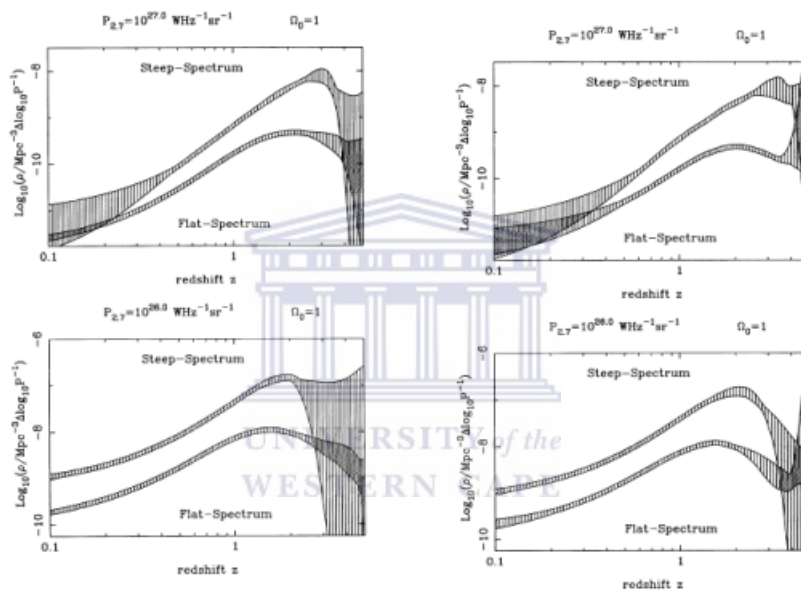


**Figure 3.2:** Number density against redshift at two luminosities  $P_{2.7 \text{ GHz}} = 10^{27} \text{ WHz}^{-1} \text{sr}^{-1}$  (top panels) and  $P_{2.7 \text{ GHz}} = 10^{26} \text{ WHz}^{-1} \text{sr}^{-1}$  (bottom panels) for flat spectrum and steep spectrum radio sources. The figures show the limits to the number density allowed by the new model RLFs (mean- $z$  data for left panels) and the new model RLFs (high- $z$  data for right panels). We can see that there is (in average) about 10 times more steep spectrum than flat spectrum radio sources at least up to redshift  $z = 2$ .  $\Omega_0 = 1$  is the matter density in De Sitter cosmology (adopted from Dunlop and Peacock (1990) [39]).

### Fraction of quasars in the quasar mode accretion model

In the quasar mode accretion we use the simulation of major mergers by Hopkins et al. (2005) [48] to estimate how many radio sources we expect in the time step of the Millennium simulation. They state that the major merger systems are bright QSOs (Figure (3.3)) between the time  $T=1.39$  Gyr and  $T=1.48$  Gyr (Hopkins et al. (2005) [48]). This gives an estimate of the average lifetime of the systems to be  $1.48-1.39=0.09 \simeq 0.1$  Gyr. The average time step in the Millennium simulation is  $t \simeq 0.3$  Gyr. This implies that only a fraction  $\frac{T}{t} = \frac{0.1}{0.3} \simeq 30\%$  of the major mergers picked out from the simulation in quasar mode accretion should be in a QSO phase. The radio AGN phase is the stage of black hole growth when it produces radio activities. It is much shorter than the whole AGN phase. The AGN phase lasts 0.1 Gyr while the radio-loud high luminosity phase lasts only about  $3 \times 10^7$  yr = 0.03 Gyr<sup>1</sup>. Then in the timestep of 0.3 Gyr only  $\frac{0.03 \text{ Gyr}}{0.3 \text{ Gyr}} = 10\%$  of AGN are in radio phase. This fraction includes steep spectrum and flat spectrum sources. There are about 10 times as many steep spectrum sources as flat (Dunlop & Peacock (1990) [39]) suggesting that only  $30\% \times \frac{10}{100} = 3\%$  of the major mergers identified in the timestep (between two snapshots) of the Millennium simulation are radio luminous flat spectrum AGN. This includes radio, infrared, optical and X-ray AGN. This gives us a fraction of  $3\% \times \frac{10}{100} = 0.3\%$  blazars. As this fraction is central to our modelling we compare it with estimations from other studies. Bird et al. (2008) [10] argue for example that the average FR II lifetimes are about  $1.5 \times 10^7$  yr with a duty cycle of about 0.02 (that corresponds to  $8 \times 10^8$  yr time off). Then the expected percentage of FR II radio galaxies in the simulation is  $\frac{0.015 \text{ Gyr}}{0.3 \text{ Gyr}} = 5\%$ . As FR II quasars are steep spectrum and they are about 10 times more than flat spectrum the percentage of flat spectrum blazars in our simulation should be  $5\% \times \frac{1}{10} = 0.5\%$ .

In the quasar mode accretion we adopt the average percentage of 0.5% for the fraction of major mergers identified as brighter blazars.

---

<sup>1</sup>Some recent determination from the 2dF QSO survey gives a life time of quasar between  $4 \times 10^6$  yr and  $6 \times 10^8$  yr (Croom et al. (2005) [30]).

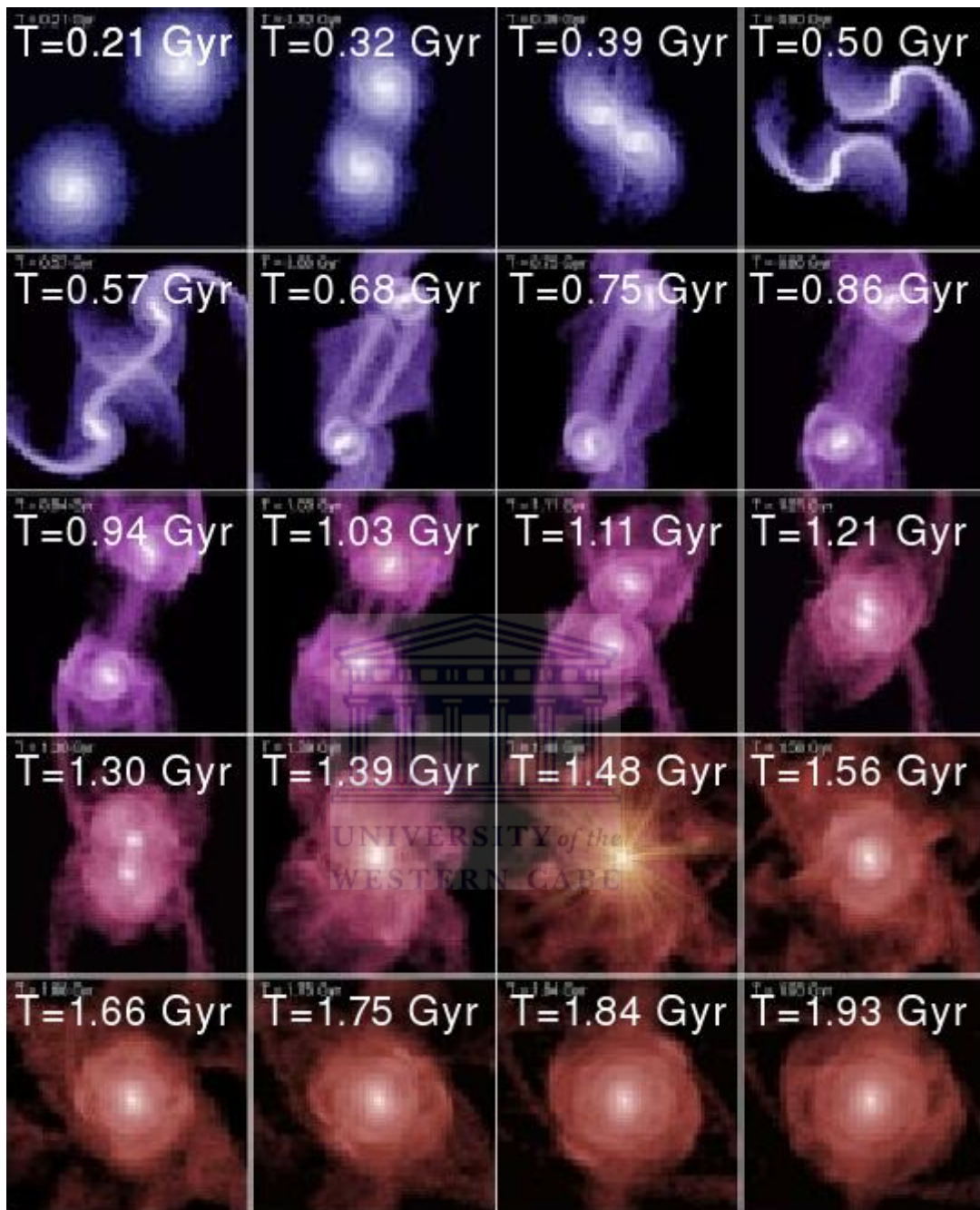


**Figure 3.3:** Simulations of major mergers. Each panel is  $80h^{-1}$  Mpc on a side and the time evolution is shown in the upper left corner. The blue colour corresponds to baryonic gas fraction of 20% and the red colour less than 5%. The black hole is seen as an optically bright QSO at the time  $T = 1.03$  Gyr (systems ongoing merging), 1.39 Gyr and 1.48 Gyr. The nuclear point sources shown in the figure during these three period of times represent the relative luminosities of stars and quasars (adopted from Hopkins et al. (2005) [48]).

### 3.6 Spectral energy distribution

To compute the fraction of the bolometric luminosity of the galaxies that is converted to radio luminosity we use the average SED of the radio galaxies, quasars and blazars and then apply the following formula

$$f_{\nu_o} = \frac{\int_{\nu_o - \frac{\Delta\nu}{2}}^{\nu_o + \frac{\Delta\nu}{2}} \frac{\nu L_\nu}{\nu} d\nu}{\int_{\nu_{\min}}^{\nu_{\max}} \frac{\nu L_\nu}{\nu} d\nu}. \quad (3.24)$$

The spectral energy distribution of the radio source gives the variation of  $\nu L_\nu$  or  $\nu F_\nu$  as a function of the frequency  $\nu$  where  $L_\nu$  and  $F_\nu$  are respectively the luminosity and the flux density of the source at the frequency  $\nu$ . They are provided in table or figure from the literature. We obtain an analytical expression of  $L_\nu$  or  $F_\nu$  as a function of  $\nu$  by using a numerical interpolation on the table. After getting the expression of the luminosity  $L_\nu$  or the flux density  $F_\nu$  as a function of the frequency  $\nu$ , we perform a numerical integration of the formula (3.24) where  $\nu_o$  is the frequency of the observation with a bandwidth  $\Delta\nu$ . The luminosity or flux interpolation was done by a fitting with gnuplot and the integration with *Mathematica*. The resulting fractions are introduced directly in the code that is used to model the radio mode accretion and quasar mode accretion.

The SEDs used are taken from different sources in the literatures and they are chosen at different redshift and different luminosities to see how they affect the model. For example for the same type of radio source (e.g. blazar) we run the simulation for different luminosities and then compare the results. We show in Figure (3.4) the SEDs of FRI radio galaxies and BL Lacs.

For the radio mode accretion the radio galaxy 3C 338 at redshift  $z = 0.0304$  was chosen from Trussoni et al. (2002) [115] to represent the mean SED of low power FRI radio galaxies. HBL Mkn 501 at  $z = 0.034$  taken from Costamante & Ghisellini (2002) [29] represents the radio spectrum for BL Lacs objects. The reason of this choice is that we know some information about the accretion rate of this blazar which is very low (Cao (2003) [19]).

For the quasar mode accretion ( $z \geq 1$ ) we have used the SEDs of the high redshift radio-loud quasar 0438-435 ( $z = 2.85$ ) from Bechtold et al. (1994) [5] for steep spectrum FR II radio galaxies. For flat spectrum blazars we adopted the following SEDs: mean SED of blazars binned in radio luminosity taken from Fossati et al. (1998) [43] and the high redshift blazar Swift J1656.3-3302 ( $z = 2.40$ ) from Masetti et al. (2008) [66]. They are shown in Figure (3.4).

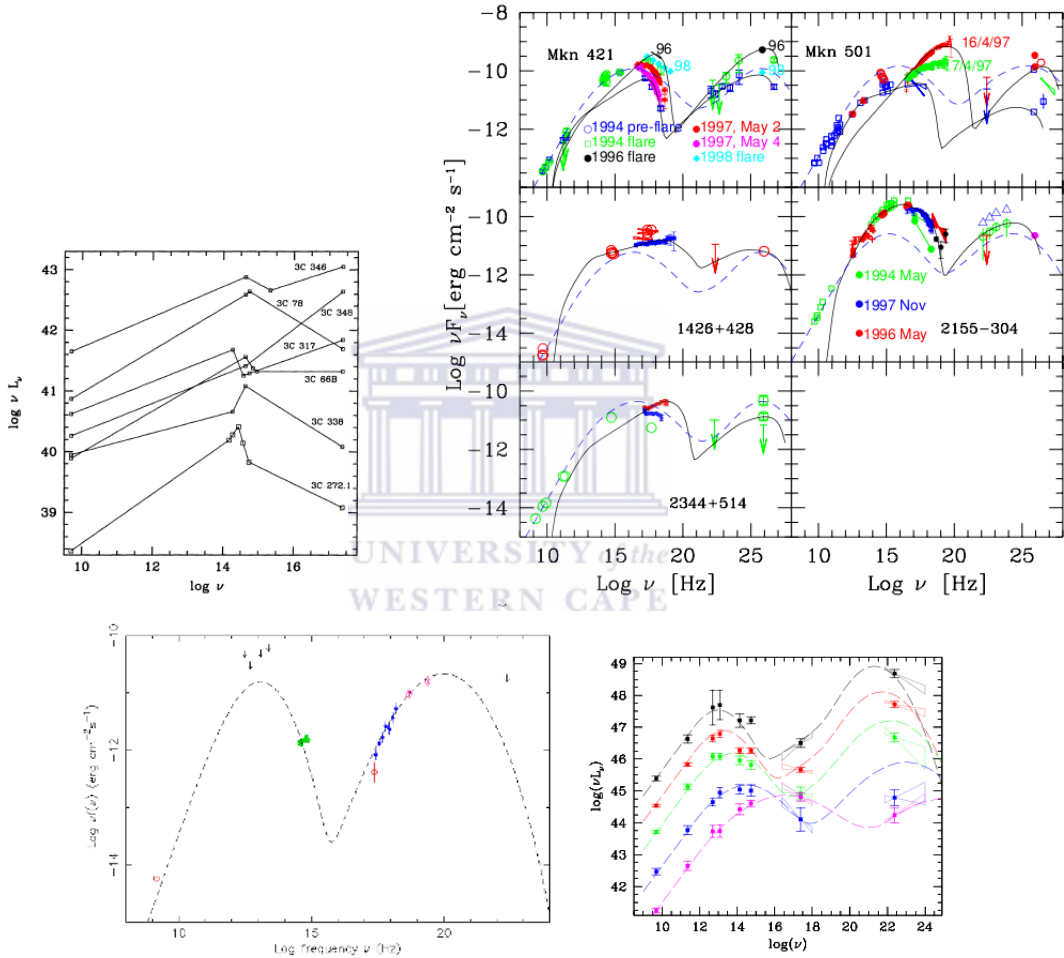


**Figure 3.4:** Spectral energy distribution of radio galaxies and blazars. 3C 338 FRI radio galaxy (top left panel). BL Lacs HBL Mkn 501 (top right). Blazar Swift J1656.3-3302 (bottom left). The bottom right panel shows the average SEDs of a blazar sample binned with radio luminosity. The dashed curves are analytic approximations of the radio spectrum. They are obtained by assuming that the ratio of the two peak frequencies is constant and that the luminosity of the second peak is proportional to the radio luminosity.

The SEDs corresponding to the above radio sources are given in Tables (3.1), (3.2), (3.3),

(3.4) and (3.5). The main SEDs used for the modelling are shown in Figure (3.5). We used spline interpolation (parabolic and cubic) to fit the SEDs. The integration of the spectrum using the formula (3.24) was done with *Mathematica*. The fitting of the SEDs obtained by the spline interpolation is shown in Figure (3.5).

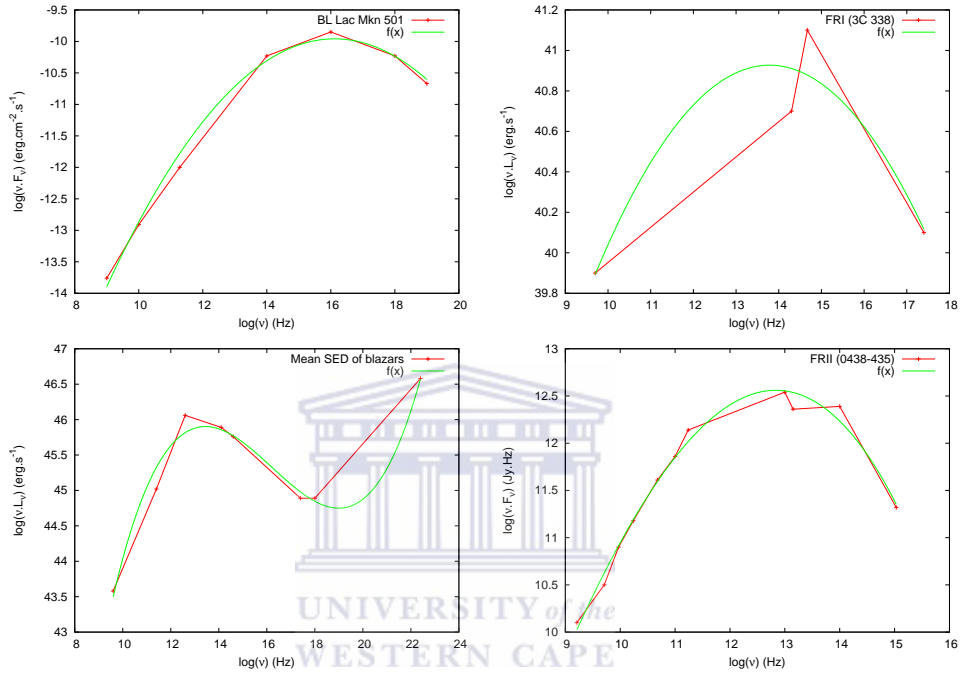


**Figure 3.5:** The figure shows, respectively, the SEDs of the low redshift ( $z = 0.034$ ) BL Lac Mkn 501 HBL (top left panel), FRI 3C 338 ( $z = 0.0304$ ) (top right panel), mean SED of blazars (bottom left panel) and FRII (0438-435) (bottom right panel). The green solid lines are parabolic (spline cubic) fits to the low power BL Lac and FRI (high power blazar and FRII) spectrum.

**Table 3.1:** Spectral energy distribution of the low power FRI 3C 338 ( $z = 0.0304$ ).

$\log(\nu)$ (Hz)	$\log(\nu L_\nu)$ (erg s $^{-1}$ )
9.7	39.9
14.3	40.7
14.7	41.1
17.4	40.1

**Table 3.2:** *Spectral energy distribution of the low luminosity BL Lacs Mkn 501 HBL ( $z = 0.034$ ).*

$\log(\nu)$ (Hz)	$\log(\nu F_\nu)$ ( $\text{erg cm}^{-2}\text{s}^{-1}$ )
9.0	-13.8
10.0	-12.9
11.3	-12.0
14.0	-10.3
16.0	-9.9
18.0	-10.2
19.0	-10.7

**Table 3.3:** *Spectral energy distribution of the high redshift blazar ( $z = 2.4$ ) Swift J1656.3-3302.*

$\log(\nu)$ (Hz)	$\log(\nu F_\nu)$ ( $\text{erg cm}^{-2}\text{s}^{-1}$ )
9.0	-14.8
9.6	-14.0
10.0	-13.5
10.3	-13.0
11.2	-12.0
12.0	-11.2
13.0	-10.8
14.0	-11.1
15.0	-12.4
15.3	-13.0
16.0	-13.5
16.4	-13.0
17.0	-12.4
18.0	-11.5
19.0	-10.9
20.0	-10.7

**Table 3.4:** *Average SED of blazars binned in radio luminosity.*

$\log(\nu)$ (Hz)	$\log(\nu L_\nu)$ ( $\text{erg s}^{-1}$ )
9.6	43.6
11.4	45.0
12.6	46.1
14.1	45.9
14.6	45.8
17.4	44.9
18.0	44.9
22.4	46.6

**Table 3.5:** *Spectral energy distribution of the high redshift FR II radio galaxies ( $z = 2.85$ ).*

$\log(\nu)$ (Hz)	$\log(\nu F_\nu)$ (JyHz)
9.2	10.1
9.7	10.5
10.0	10.9
10.2	11.2
10.7	11.6
11.0	11.9
11.2	12.1
13.0	12.5
13.2	12.4
14.0	12.4
15.0	11.3

The SEDs used are individually different. For a particular AGN we expect higher number density of FRI radio galaxies compared to BL Lacs for low luminosity AGN and higher number density of FR II radio galaxies compared to blazars for high luminosity AGN. This is due to the orientation effect of the AGN: BL Lacs and brighter blazars are just FRI and FR II radio galaxies viewed toward the observer so that there are more FRI/FR II radio galaxies than BL Lacs/brighter blazars in the simulation volume. For an AGN (e.g. blazar) at different redshift, the number density is increasing with redshift since AGNs were more abundant in the early time.



### 3.7 Database query

We present in this section the queries used for obtaining the galaxies and their properties in the Millennium simulation. For the galaxies needed for the modelling we have to use the full volume of the Millennium since we compute the number density of radio sources. The milli-Millennium simulation gives only a limited number of galaxies in a volume which is approximately 512 times smaller so that the determination of the space density is not always possible at the different redshift of the snapshots. We worked on the MPAGalaxies database that stores the results of the MPA semi-analytical model of galaxy formation and evolution.

For the radio mode accretion we extracted from the table DeLucia2006a all galaxies identified at a given snapshot 1 and find the progenitors of all the galaxies at snapshot 2 ( $\text{snapnum } 1 < \text{snapnum } 2$ ). The count of galaxies gives a few million galaxies which requires a query time longer than the query timeout of the SQL database. This lead us to split in different files the results of the query. We broke up the simulation box into 512 region and downloaded information for each section independently using a shell script (see below). As we are interested in the black hole mass accretion rates we consider two successive snapshots which give us a timestep. We present in the following the query for the radio mode accretion. It shows the example of how we obtained all galaxies at the snapshot 63 ( $\text{snapnum}=63$ ) and their progenitors at the snapshot 62 and the results are stored in the files `radio63.1.csv`, `radio63.2.csv` up to `radio.512.csv`. We apply the same query for getting the galaxies in the halos by adding a condition on the property *centralMvir* which gives the virial mass of the central background halo containing this galaxy. Basically we run our query for every snapshot.

```
#!/bin/bash
for i in `seq 1 512`;
do
    j=$((i-1))
    m=$i
    if [ $i -lt 10 ]; then m=0$i
    fi
```

```

    if [ $i -lt 100 ]; then m=0$m
    fi
    n=$j
    if [ $n -lt 10 ]; then n=0$n
    fi
    if [ $n -lt 100 ]; then n=0$n
    fi

wget --http-user=framamonjisoa --http-passwd=mypassword -O
data/radio63.$m.csv "http://www.g-vo.org/MyMillennium3?
action=doQuery&SQL=
select des.galaxyId as descendant_Id,
prog.galaxyId, des.fofId, des.centralMvir,
des.blackHoleMass as descendant_blackHoleMass,
prog.blackHoleMass,
prog.x, prog.y, prog.z from
MPAGalaxies..DeLucia2006a des,
MPAGalaxies..DeLucia2006a prog
where prog.blackholemass > 0
and prog.descendantID = des.GalaxyID
and des.SubHaloID between 630"$n"00000000
and 630"$m"00000000-1 order by des.galaxyID asc"
done
exit 0

```

For the quasar mode accretion we considered the galaxies that have undergone major mergers defined as galaxies that have at least two progenitors with stellar masses greater than 0.2 times the descendant stellar mass in the merger tree. As the count of galaxies gives about few thousand galaxies the query was carried out directly on the browser.

In both radio mode accretion and quasar mode accretion we are mainly interested in the properties such as the *descendant black hole mass*, the *progenitor black hole mass* and the

*coordinates of the galaxies* and eventually the *virial mass of the halo* containing the galaxy in the case of galaxy clusters. The example of query for obtaining major mergers at the snapshot 62 of galaxies identified at snapshot 63 (redshift  $z = 0$ ) is given below.

```

select des.galaxyId as descendant_Id,
       des.fofId,
       des.centralMvir,
       P1.galaxyId as p1_id,
       P2.galaxyId as p2_id,
       des.blackHoleMass as descendant_blackHoleMass,
       P1.blackHoleMass as P1blackHoleMass,
       P1.x as x1, P1.y as y1, P1.z as z1,
       P2.blackHoleMass as P2blackHoleMass,
       P2.x as x2, P2.y as y2, P2.z as z2,
       des.stellarMass as des_mass,
       P1.stellarMass as p1_mass,
       P2.stellarMass as p2_mass
from MPAGalaxies..DeLucia2006a P1,
     MPAGalaxies..DeLucia2006a P2,
     MPAGalaxies..DeLucia2006a des
where P1.snapnum=P2.snapnum
and des.snapnum=63
and P1.galaxyId< P2.galaxyId
and P1.descendantId = des.galaxyId
and P2.descendantId = des.galaxyId
and P1.stellarMass >= .2*des.stellarMass
and P2.stellarMass >= .2*des.stellarMass
and P1.galaxyId between des.galaxyId and des.lastprogenitorId
and P2.galaxyId between des.galaxyId and des.lastprogenitorId
and P1.snapnum=62
and des.blackHoleMass>0

```

```
order by des.galaxyId asc
```

### 3.8 Redshift distribution

The redshift distribution of the radio sources gives the number of radio sources per redshift bin as a function of redshift in the simulation. We use this redshift distribution instead of the number density to compare with the observations since it is independent of the adopted cosmology as described in Dunlop & Peacock (1990) [39]. We obtain the redshift distribution by multiplying the number density ( $\frac{dn}{dV}$ ) given by the simulation with the derivative of the comoving volume  $V$  with respect to the redshift ( $\frac{dV}{dz}$ ).

The RLF of Dunlop & Peacock (1990) [39] was obtained from a sample of data at 2.7 GHz with a flux density limit 100 mJy (Parkes selected regions). They give five different formulations of the model of RLF. Waddington et al. (2001) [118] claim that the model number four and five of radio luminosity function (RLF4 and RLF5) of Dunlop & Peacock (1990) [39] provide a good match with the Leiden-Berkeley Deep Survey (LBDS, Waddington et al. (2001) [118]) at 1.4 GHz with a flux density limit 1 mJy. This flux density limit 1 mJy at 1.4 GHz can be translated to the corresponding flux density limit at 2.7 GHz by using the relation:

$$S \propto \nu^{-\alpha} \tag{3.25}$$

where  $\nu \simeq 0.8$  is the average spectral index of radio sources and  $\nu$  the frequency of the observation. Hence:

$$S_{(2.7 \text{ GHz})_{lim}} = \left(\frac{2.7}{1.4}\right)^{-0.8} (1 \text{ mJy}) \tag{3.26}$$

$$= 0.6 \text{ mJy}. \tag{3.27}$$

This explain our choice of  $S_{\text{cut}} = 0.6 \simeq 1$  mJy at 2.7 GHz in our simulation. In addition Brookes et al. (2008) [18] found that the model RL4 and RLF5 provide the best description of the Combined EIS-NVSS Survey of Radio Sources (CENSORS, Brookes et al. (2008) [18]) data at 1.4 GHz selected from the NRAO VLA Sky Survey (NVSS, Brookes et al. (2008) [18]) complete to a flux density limit 7.2 mJy. However it is important to note that they found a less good match with the data than found by Waddington et al. (Brookes et al. (2008) [18], Waddington et al. (2001) [118]).

We now describe the calculation of the redshift distribution of the radio sources assuming that the dominant mode of accretion in BL Lacs objects and FRI radio galaxies is the radio mode accretion and that brighter blazars and FRII radio quasars are triggered by the quasar mode accretion. Our simulation gives the number density of the radio AGN as a function of redshift in the  $\Lambda$ CDM cosmology with the cosmological parameters defined in the Millennium simulation.

The integration of the radio luminosity function of Dunlop & Peacock (1990) [39] gives the number density against redshift of flat spectrum radio galaxies and quasars in De Sitter cosmology. So we use the redshift distribution for comparison. We calculate the redshift distribution of radio sources in our model using the formula

$$\left(\frac{dn}{dz}\right)_{\text{simul}} = \left(\frac{dn}{dV}\right)_{\text{simul}} \left(\frac{dV}{dz}\right)_{\Lambda\text{CDM}} \quad (3.28)$$

where  $\left(\frac{dn}{dV}\right)_{\text{simul}}$  is the number density obtained by our simulation and  $\left(\frac{dV}{dz}\right)_{\Lambda\text{CDM}}$  the derivative of the comoving volume against the redshift in the  $\Lambda$ CDM cosmology. This was done by using a cosmological calculator. Using the same procedure we compute the redshift distribution in De Sitter cosmology adopted by Dunlop & Peacock (1990) [39] with the following formula

$$\left(\frac{dn}{dz}\right)_{\text{DP}} = \left(\frac{dn}{dV}\right)_{\text{DP}} \left(\frac{dV}{dz}\right)_{\text{DeSitter}} \quad (3.29)$$

where  $\left(\frac{dn}{dV}\right)_{\text{DP}}$  is the number density obtained from the integration of the RLF of Dunlop & Peacock (1990) [39] and  $\left(\frac{dV}{dz}\right)_{\text{DeSitter}}$  the derivative of the comoving volume  $V(z)$  in that

cosmology. The redshift distribution is binned with redshift and as the number of spectroscopically observed radio sources at high redshift is limited we choose a wide bin. We adopted  $\Delta z = 0.4$  and used an interpolation to obtain the intermediate values of the number density at the binned redshifts.

### 3.9 Density profiles of radio galaxies in clusters

We now can use the model to simulate the properties and distribution of radio sources in a cluster-like environment which is important for the galaxy clusters surveys. In this section we explain the method we used for the calculation of the surface density of radio sources as a function of the radial distance  $r$  from the centre of the cluster. This gives the projected number density of the radio sources in units of  $\text{Mpc}^{-2}$  as a function of the radial distance from the centre of the cluster. The signals from radio sources within a cluster are added to give the total contribution of the signals.

First we extract from the Millennium simulation all galaxies identified at a redshift  $z_1$  (snapnum 1) and their progenitors at redshift  $z_2 > z_1$  (snapnum 2 < snapnum 1) in massive halos with a virial mass  $M_{\text{vir}} \geq 2 \times 10^{14} h^{-1} M_{\odot}$  (mass detection limit of the ACT). This is done by using the corresponding snapshots. Then we use our model to estimate the number of FRI and FRII radio galaxies and blazars. As we look at the radial distribution of the radio sources we need to determine the centre of each cluster in the box of our snapshot. We did this by taking the coordinates of all galaxies in each cluster and then computing the barycentre. By doing this we obtain a good approximation of the location of the centres of the clusters since we have more galaxies than radio sources in the simulation. This was done by the code *cluster\_centre.f*. The corresponding flow chart is shown in Figure (3.6) top panel. To facilitate the calculation of the distance of radio galaxies from the centre of each cluster we wrote the code *radio\_centre.f* which outputs the virial mass of each cluster, the centre of this cluster and the position of the radio sources. The flow chart of the programme is shown in Figure (3.6) bottom panel. Finally we compute the surface density profile of the radio sources with another code *surf\_dens.f* that we show the corresponding flow chart in

Figure (3.7). To do this we stacked the data as follows: we scale the clusters with a given virial radius and compute the resulting surface density  $\Sigma$ . Precisely we calculate the surface densities for different values of the virial radii defined by the cluster virial masses. This is necessary because clusters have very different sizes that depend on the virial mass of the cluster as given by the relation (Fujita & Takahara (1999) [44])

$$r_{\text{vir}} = 259 \left( \frac{M_{\text{vir}}}{10^{12} M_{\odot}} \right)^{\frac{1}{3}} \text{ kpc} \quad (3.30)$$

where the virial radius  $r_{\text{vir}}$  is the size scale defined by the cluster mass. The size of the clusters in our simulation ranges from about 1.7 Mpc to 3.8 Mpc. Therefore we use different scaling by the virial radius for the calculation of the surface density which is given by the following relation:

$$\Sigma = \frac{\text{number\_radio}}{\pi r^2} \quad (3.31)$$

where *number\_radio* is the number of the radio galaxies or blazars within the radius  $r$  from the centre of the cluster scaled with the virial radius  $r_{\text{vir}}$ .

### 3.10 Calculation of the temperature and fluxes of radio sources

After we get the information about the positions and concentrations of radio sources in clusters we need to know the fluctuations caused by these radio AGN. Here we explain the method we used to compute the temperature fluctuations and the fluxes. Since we aim to compare our results to data from the ACT survey we consider only clusters with a virial mass  $\geq 2 \times 10^{14} h^{-1} M_{\odot}$  which is the limiting mass of the ACT (Kosowsky (2004) [55]). We look at a given cluster with a given redshift (mean redshift of the snapshots) in the simulation and as we know the distribution of the radio sources we can compute the fluctuations caused by these radio galaxies. We proceed the same for all clusters in our snapshot. In each snapshot of the simulation we take the mean temperature fluctuations and fluxes of the radio sources in the clusters and then compute the deviation from the mean.

We use the same method described in the modelling of the space density of radio sources

(Section (3.2)) to compute the black hole mass accretion rate. After this we get the bolometric luminosity and the converted radio luminosity of the source at each frequency of ACT (145 GHz, 220 GHz, 270 GHz) using equations (3.2) and (3.3). Then we can compute the flux using the following equation:

$$S = \frac{L}{4\pi d_L^2 \Delta\nu} \quad (3.32)$$

where  $d_L$  is the luminosity distance at the mean redshift of the snapshots between which we compute the black hole mass accretion rate,  $L$  the radio luminosity and  $\Delta\nu$  the frequency bandwidth of the observation. We compute the temperature fluctuation from radio sources by converting the flux density  $S_\nu$  to CMB temperature units using the following formula (Scannapieco et al. (2008) [94])

$$\Delta T = \left(\frac{dB_\nu}{dT}\right)^{-1} \frac{S_\nu}{\theta_{\text{FWHM}}^2} \quad (3.33)$$

$$= 1 \mu\text{K} \left(\frac{1 \text{ arcmin}}{\theta_{\text{FWHM}}}\right)^2 \frac{S_\nu}{0.0084 \text{ mJy}} \frac{(e^x - 1)^2}{x^4 e^x} \quad (3.34)$$

where  $B_\nu$  is the Planck function,  $\theta_{\text{FWHM}}$  the beam size at full width at half maximum (resolution in arcminute) and

$$x = \frac{h\nu}{kT_{\text{CMB}}} \simeq \frac{\nu \text{ (GHz)}}{56.8} \quad (3.35)$$

(Scott & White (1999) [95]).

We get as an output the virial mass of all clusters and the corresponding temperature and fluxes. We wrote the fortran code *SZ.f* to compute the fluctuations and we show in Figure (3.8) the flow chart of the programme.

The next step is now to sum up the contribution of the radio galaxies and quasars in the same cluster in the temperature fluctuations and fluxes. This is done by another code *Mvir\_sum.f* which gives as an output the virial mass of each cluster and the sum of the temperature and the corresponding fluxes. We show the flow chart of this code in Figure (3.9). The last step is to compute the mean temperature fluctuations and fluxes of the clusters which is done by another code *fluc\_mean.f*. We use the output file from the code *Mvir\_sum.f* as an input



in the code *fluc\_mean.f*. The corresponding flow chart is in Figure (3.10). It gives also the standard deviation from the mean temperature and fluxes.

### 3.11 Summary

We have seen in this chapter how to compute the space density of radio galaxies and quasars as a function of redshift in the two types of accretion: radio mode accretion and quasar mode accretion. The redshift distribution of radio sources depends strongly on the choice of the accretion efficiency (as we will discuss later in the results) and the SED (radio galaxies having different luminosities) and eventually the black hole masses. We can summarize the input parameters as follows:

- Radio mode accretion

- We assume that  $\sim 7\%$  of the galaxies in each snapshot (up to  $z \simeq 0.7$ ) of the simulation are BL Lacs. We assume an accretion efficiency of  $\varepsilon \simeq 10^{-4}$  which corresponds to the observed one of HBL Mkn 501.

- $66\%$  ( $\simeq 70\%$ ) is the fraction of FRI radio galaxies in the simulation and  $66\% \times \frac{1}{10} = 6.6\% \simeq 7\%$  (Section(3.5)) the fraction of flat spectrum low luminosity BL Lacs. This gives about  $66\% - 6.6\% \simeq 60\%$  of the galaxies as been steep spectrum FRI. We take an average luminosity of FRI with the example of 3C 338 with an accretion efficiency  $\varepsilon \simeq 10^{-5}$ .

- Quasar mode accretion

- We assume that  $0.5\%$  of major mergers are blazars at  $z \gtrsim 1$ . We use the standard accretion efficiency  $\varepsilon \simeq 0.1$ .

- This corresponds to  $5 - 0.5 = 4.5\%$  of major mergers as been FRII radio-loud quasars. We consider the case of RLQ with low and high redshift SED.

We chose the accretion efficiencies for BL Lacs and FRI to better match the observed redshift distribution of the radio sources and besides referred to respectively Costamante (2002) [29] and Kurosawa et al. (2009) [56]. Using this model we compute the temperature fluctuations and fluxes due to radio galaxies and quasars present in galaxy clusters. In this way we can estimate the contamination caused by these radio sources by comparing their values with the cluster SZ signals. The cluster is difficult to detect in the SZ surveys if the fluctuation caused by the radio sources is of the order or greater than the cluster SZ signals.



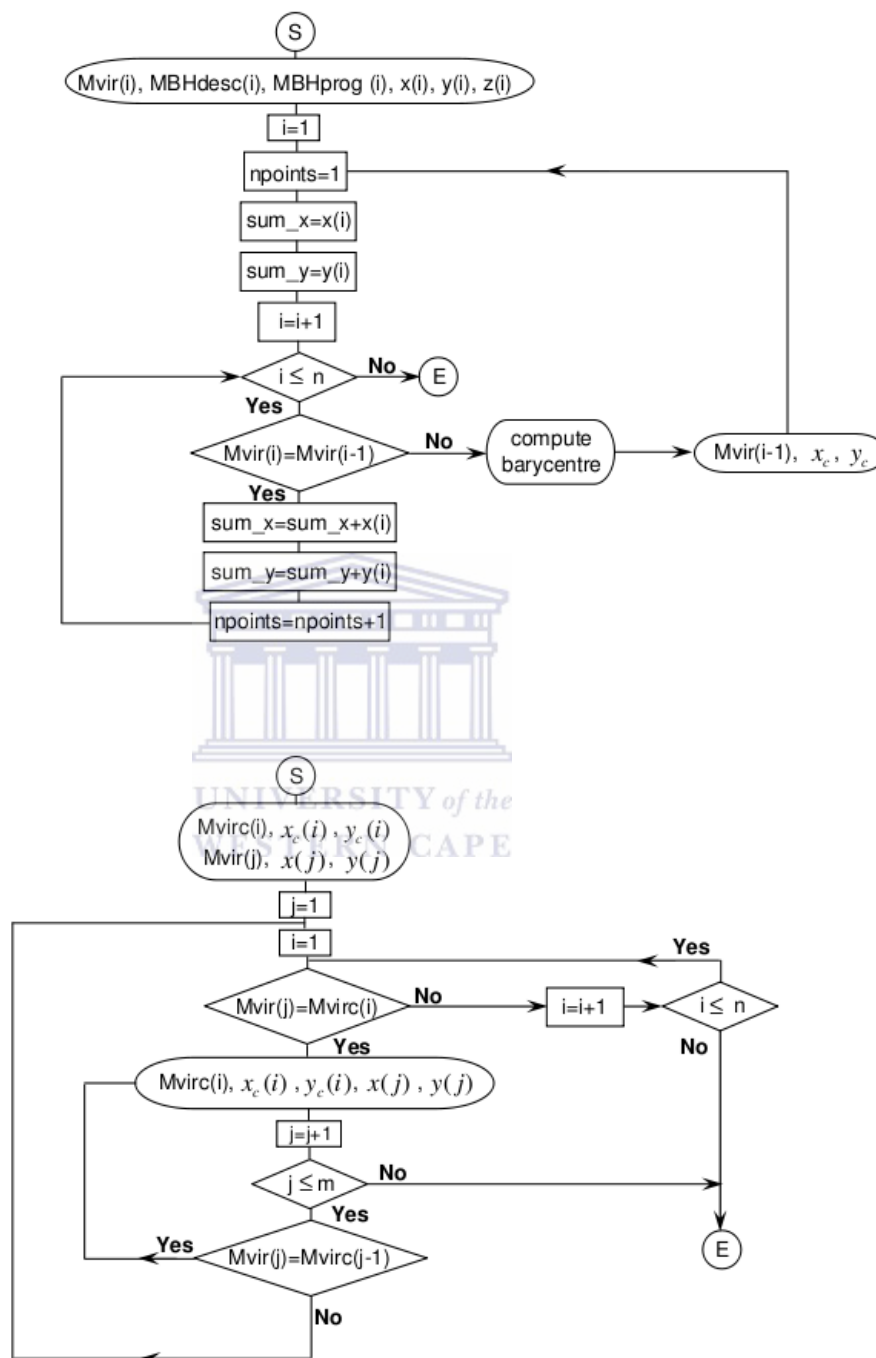


**Figure 3.6:** Flow charts for the determination of the centres of the clusters (top panel) and the virial masses of clusters with their centre and the radio sources coordinates (bottom panel).

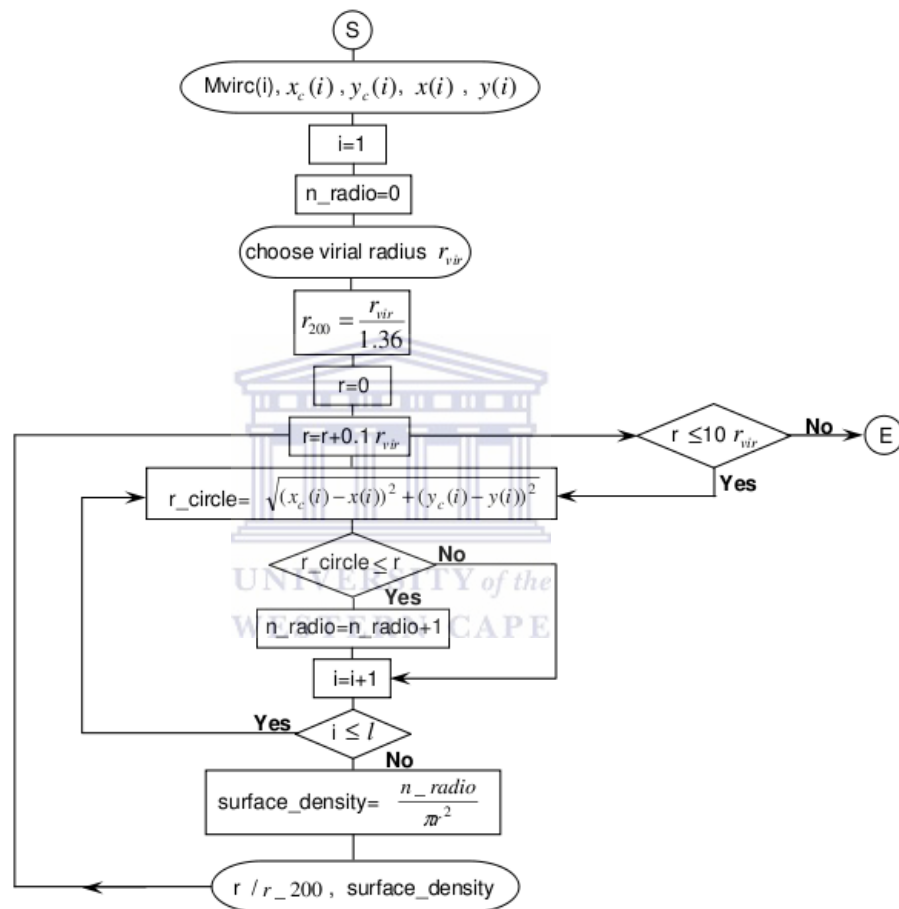


**Figure 3.7:** Flow chart of the programme for the calculation of the surface density of radio sources as a function of the ratios of the radial distance  $r$  from the centre of the cluster to  $r_{200}$ .

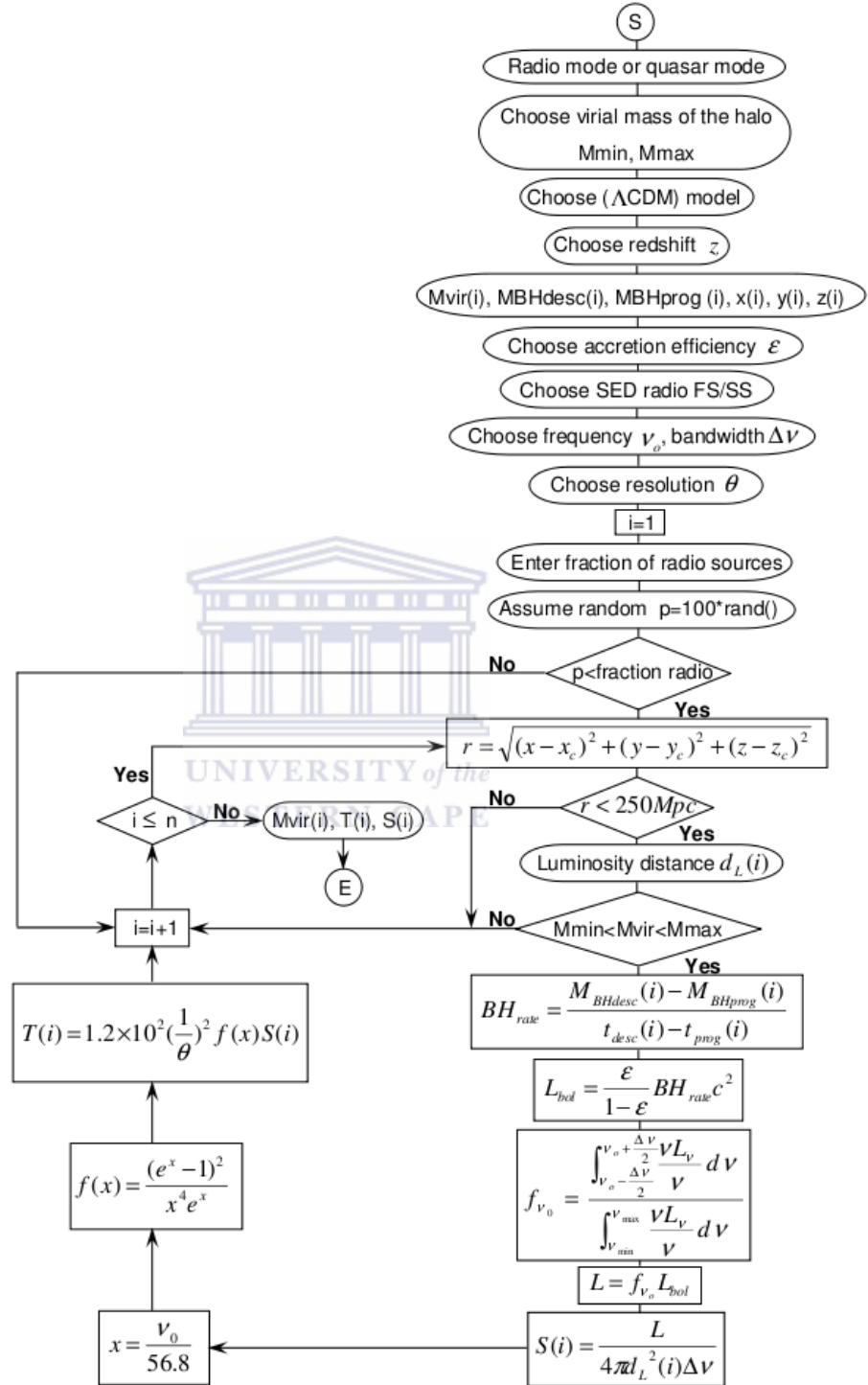


**Figure 3.8:** Flow chart for the calculation of the temperature fluctuations and fluxes due to radio sources in clusters.

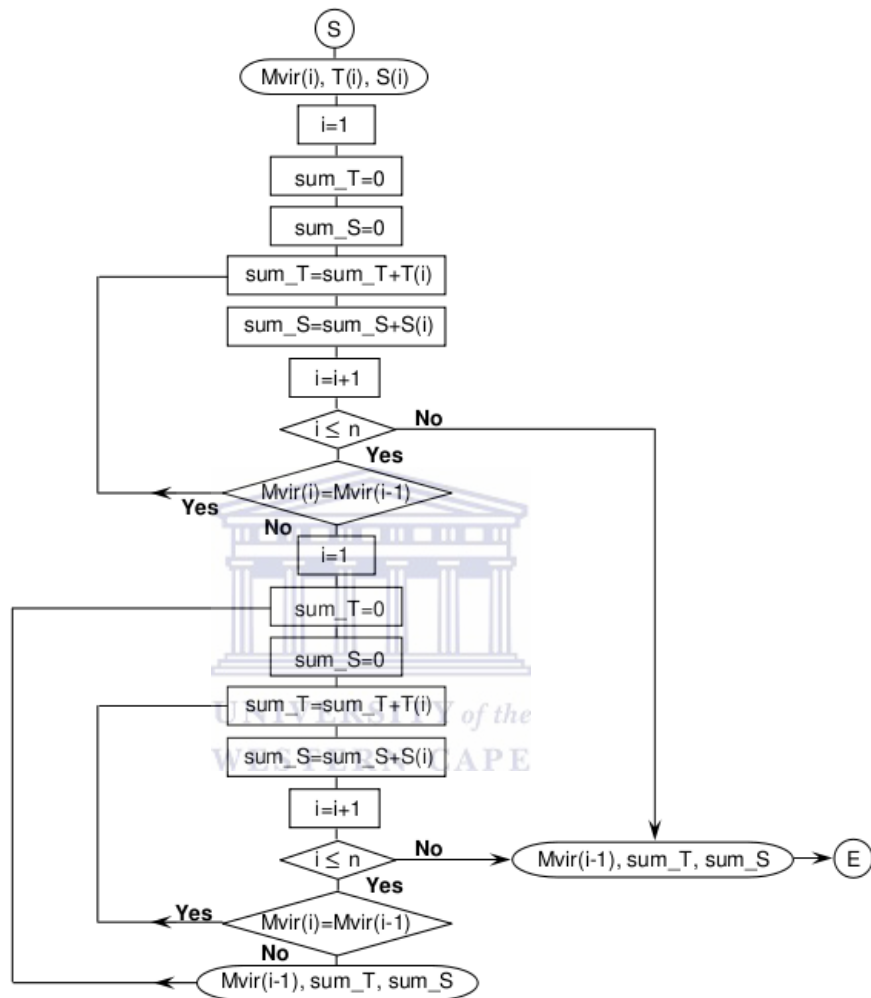


**Figure 3.9:** Flow chart for the calculation of the virial mass of each cluster and the sum of the temperature and corresponding fluxes due to the radio sources in that cluster.

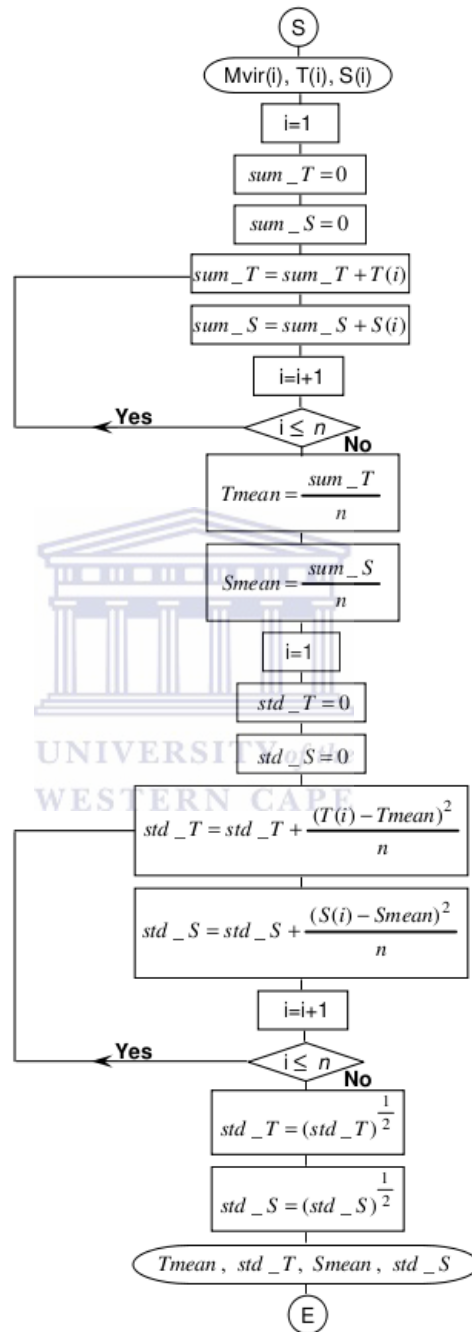


**Figure 3.10:** Flow chart for the calculation of the average temperature fluctuations and fluxes of the clusters and deviation from the mean.

# Chapter 4

## Results and Discussion

### 4.1 Introduction

In this chapter we present the results of our model. We start with the derivation of the best fit of the radio luminosity function as described by Dunlop & Peacock (1990) [39]. Then we describe the fitting of the SED that is used to compute the fraction of the bolometric luminosity converted into radio luminosity. The space densities against redshift are computed for a flux cut-off 1 mJy at 2.7 GHz that we compare with Dunlop & Peacock (1990) [39]. The queries used for obtaining the galaxies and major mergers at different snapshots are also given. After this we describe the spatial distribution of radio sources at different redshift then compute the surface density of radio sources as a function of radial distance and in the next section we compute the temperature fluctuations and fluxes of radio sources against redshift using the three observing frequencies of the ACT.

### 4.2 Model of radio luminosity function

We aim our study, as we state in Section (3.1), at the radio sources viewed with a small inclination angle toward us. We consider the flat spectrum model of RLF4 and RLF5 which are described as the model four and five of RLF in Dunlop & Peacock (1990) [39]. RLF4 and RLF5 provide the best fit of the Leiden-Berkeley Deep Survey (LBDS) Hercules sample



of mJy radio sources at 1.4 GHz (Waddington et al. (2001) [118]) and the Combined EIS-NVSS Survey Of Radio Sources (CENSORS) complete to a flux density of 7.2 mJy at 1.4 GHz (Brookes et al. (2008) [18]). In their study Dunlop & Peacock (1990) [39] model flat spectrum as well as steep spectrum quasars and radio galaxies. In our model flat spectrum corresponds to BL Lacs (FRI type radio galaxies with small inclination angle) and brighter blazars (FRII type radio galaxies with small inclination angle). We present in the following the integration of the RLF4 and RLF5 flat spectrum model.

### 4.2.1 Model RLF4

RLF4 and RLF5 models were determined using the following series expansion:

$$\log_{10}(\rho) = \sum_{i=0}^n \sum_{j=0}^{n-i} A_{ij} x^i(P) y^j(z). \quad (4.1)$$

In this formula  $\rho$  represents the space density of radio sources which depends on the redshift  $z$  and the luminosity (radio power)  $P$  of the sources.  $x$  and  $y$  are transformed axes of  $P$ - $z$  plane. The coordinates  $(P, z)$  of the models are  $[0.1(\log_{10}(P)) - 20, 0.1z]$ . The integration of RLF4 is carried out from  $z = 0$  to  $z = 5$  and over the luminosity  $P = 10^{18} \text{ W Hz}^{-1} \text{ sr}^{-1}$  to  $P = 10^{30} \text{ W Hz}^{-1} \text{ sr}^{-1}$  at 2.7 GHz. The table of RLF expansion coefficients are found in Table C1 and Table C2 of Dunlop & Peacock (1990) [39]. Following the redshift estimation of the sources, the data are distributed into MEAN- $z$  and HIGH- $z$  data.

We obtained from the RLF the observed number densities (in  $\text{Gpc}^{-3}$ ) of radio galaxies and quasars as a function of redshift  $z$  by means of numerical integration using the software *Mathematica*. The results of the integration of RLF4 are given in Tables (4.1), (4.2).

**Table 4.1:** *Space densities of the model RLF<sub>4</sub> MEAN- $z$  as a function of the redshift  $z$ .*

Redshift $z$	Space density (/Gpc <sup>3</sup> )
0.01	2685
0.10	535
0.19	90
0.30	329
0.39	310
0.48	302
0.79	290
1.03	276
1.44	236
1.57	222
1.99	177
2.52	135
2.95	110
3.44	89
4.02	72
4.35	64
4.70	57



**Table 4.2:** Space densities of the model RLF4 HIGH- $z$  as a function of the redshift  $z$ .

Redshift $z$	Space density (/ Gpc <sup>3</sup> )
0.01	2550
0.10	539
0.19	391
0.30	329
0.39	307
0.48	296
0.79	284
1.03	273
1.44	236
1.57	222
1.99	176
2.52	129
2.95	102
3.44	79
4.02	61
4.35	54
4.70	49

### 4.2.2 Model RLF5

The model RLF5 is using the same series expansion as RLF4 but in addition a cut-off at high redshift is enforced such that RLF5 shows a sinusoidal decay from  $z=2$  to a value of zero at  $z>5$ . Hence:

$$\rho \rightarrow \frac{1}{2}\rho (1 + \cos\phi) \quad (4.2)$$

for  $2 < z < 5$  where  $\phi = (z - 2)\frac{\pi}{3}$

and

$$\rho = 0 \quad (4.3)$$

for  $z \geq 5$ .

The results of the integration of RLF5 are given in Tables (4.3) and (4.4).

**Table 4.3:** *Space densities of the model RLF5 MEAN- $z$  as a function of the redshift  $z$ .*

Redshift $z$	Space density (/ Gpc <sup>3</sup> )
0.01	1735
0.10	516
0.19	379
0.30	324
0.39	307
0.48	300
0.79	299
1.03	297
1.44	272
1.57	261
1.99	219
2.52	172
2.95	142
3.44	117
4.02	97
4.35	88
4.70	79

These four models of RLF at 2.7 GHz extrapolated down to the corresponding flux density limit 1 mJy at 1.4 GHz of Waddington et al. (2001) [118] present the best match of the most recent observational radio survey (Brookes et al. (2008) [18]).

The flux density limit considered in our model is 1 mJy. We show in Figure (4.1) the plots of the four models of Dunlop & Peacock (1990) [39].

**Table 4.4:** Space densities of the model RLF5 HIGH- $z$  as a function of the redshift  $z$ .

Redshift $z$	Space density (/ Gpc <sup>3</sup> )
0.01	2621
0.10	522
0.19	370
0.30	309
0.39	289
0.48	280
0.79	278
1.03	276
1.44	249
1.57	236
1.99	189
2.52	139
2.95	109
3.44	85
4.02	65
4.35	61

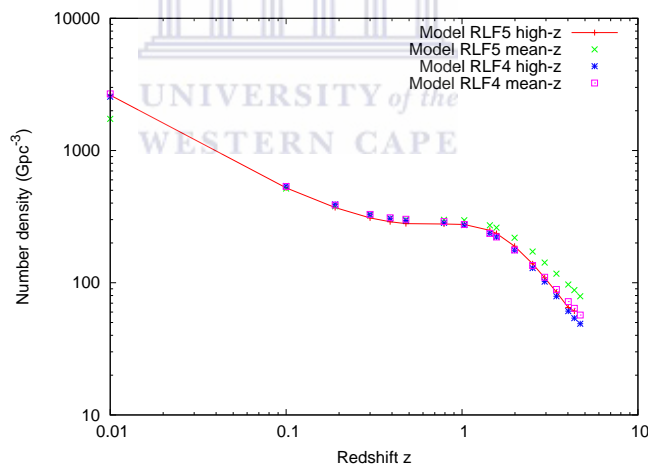


**Figure 4.1:** Model of radio luminosity functions of Dunlop and Peacock (1990) [39]. The model shows the space density of flat spectrum radio galaxies and quasars as a function of redshift with flux density limit 1 mJy at 2.7 GHz. The solid red line is the model RLF5 high- $z$  data that we use for comparison in the present work.

### 4.3 Redshift distribution of radio galaxies and quasars

We present in this section the redshift distribution of radio sources. Our main interest is the flat spectrum radio galaxies and quasars as their jets are close to the line of sight of

the observer who measures the total signals from the radio sources in that direction. They are constituted by BL Lacs and brighter blazars. We compare the redshift distribution with that obtained by Dunlop & Peacock (1990) [39]. The comparison is done with their model of RLF5 high-z data which can be viewed as the average RLF (Figure (4.1)) of the sample of flat spectrum radio sources. We consider RLF5 high-z since we include high redshift blazars in our model.

The number density of flat spectrum BL Lacs and brighter blazars and the corresponding redshift distribution in the simulation are shown respectively in Tables (4.5) and (4.6). This assumes a mean SED of the HBL Mkn 501 for BL Lacs (Section (3.6)) and the average SED of blazars adopted from Fosatti (1998) [43] (mean SED grouped by power).

**Table 4.5:** *Space density of blazars at 2.7 GHz with a flux density limit 1 mJy obtained from our model in the Millennium simulation  $\Lambda$ CDM cosmology.*

	Redshift $z$	Space density $\rho$ ( $\text{Gpc}^{-3}$ )
Radio mode accretion	0.01	1320
	0.10	1409
	0.19	6
	0.30	6
Quasar mode accretion	0.48	297
	0.79	220
	1.03	196
	1.44	113
	1.57	77
	1.99	18
	2.52	18
	2.95	6

**Table 4.6:** Redshift distribution of blazars at 2.7 GHz with a flux density limit 1 mJy obtained from our model. We assume an average SED of HBL Mkn 501 in radio mode accretion and the mean SED of high luminosity blazars from Sparke and Gallagher (2007) [96] for quasar mode accretion.

Redshift $z$	$\frac{dn}{dV}$	$\frac{dV}{dz}$	$(\frac{dn}{dz})_{DeSitter}$
0.41	66	102	6732
0.81	218	265	57770
1.21	160	393	62708
1.61	71	470	33549
2.01	18	510	9171
2.41	18	524	9432
2.81	10	524	5191
3.21	3	514	1448

The redshift distribution of the model RLF5 high- $z$  data of Dunlop & Peacock (1990) [39] is given in Table (4.7). The comoving volume was computed in their adopted De Sitter cosmology ( $\Omega_m = 1$ ). We display the rounded values and the distribution is binned with  $\Delta z = 0.4$ .

**Table 4.7:** Redshift distribution of blazars at 2.7 GHz with a flux density limit 1 mJy obtained from the model RLF5 high- $z$  data of Dunlop and Peacock (1990) [39].

Redshift $z$	$\frac{dn}{dV}$	$\frac{dV}{dz}$	$(\frac{dn}{dz})_{DeSitter}$
0.41	287	71	20380
0.81	278	234	65123
1.21	264	328	86569
1.61	232	365	84597
2.01	187	374	69917
2.41	149	367	54873
2.81	119	354	42058
3.21	96	338	32530
3.61	79	321	25387

We show in Figure (4.2) the redshift distribution  $\frac{dn}{dz}$  as a function of redshift  $z$  for flat spectrum blazars with a flux density limit 1 mJy at 2.7 GHz normalized at  $z = 0.41$ . We did this normalization arbitrarily just for the readability of the figures. The error bars shown correspond to the standard deviation. We can see that the redshift distribution is underestimated especially at high redshift  $z \gtrsim 1$ . This is explained by the choice of the

template SED and a constant accretion efficiency at all  $z \gtrsim 1$ . To improve the model we need more observational constraints on the radiative accretion efficiency which is related to the accretion efficiency.

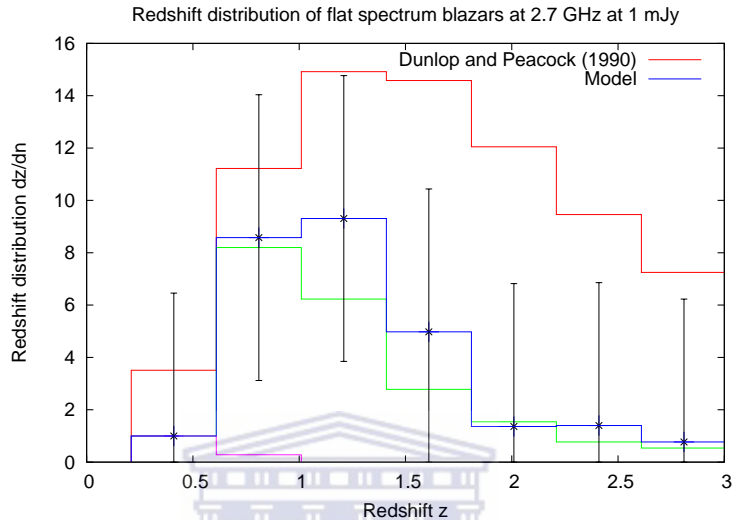


**Figure 4.2:** Redshift distribution of blazars of different luminosities at 2.7 GHz for a flux cut-off 1 mJy normalized at  $z = 0.41$ . The model corresponding to the SED of high luminosity blazars is shown in blue steps and the model of Dunlop and Peacock (1990) [39] derived from RLF5 is displayed in red. The steps in cyan correspond to the SED of the high redshift blazar Swift J1656.3-3302 at  $z \simeq 2.40$ . The green steps show the redshift distribution for the mean SED of blazars adopted in Fossati et al. (1998) [43].

## 4.4 Spatial distribution of radio sources

We show in Figure (4.3) and (4.4) the spatial distribution of radio galaxies and blazars at different redshift in the Millennium box.  $x, y, z$  are the comoving coordinates of the galaxies inside the box. We considered only radio sources inside the sphere (3D) or the circle (2D projection) of radius  $r < 250$  Mpc centred on the box. We can see that radio galaxies are to first order distributed randomly around the centre of the Millennium box. The number of radio sources declines with redshift. We assume that BL Lacs and FRI radio galaxies are triggered by the radio mode accretion for  $z \lesssim 0.5$  (Figure (4.3)) and brighter blazars and FRII radio galaxies are triggered by the quasar mode accretion for  $z \gtrsim 1$  (Figure (4.4)). We



did not include the spatial distribution of blazars for  $0.5 \leq z \leq 1.0$  because we do not have a strong observational constrain on the value of the accretion efficiency parameter (Section (2.7.4)).



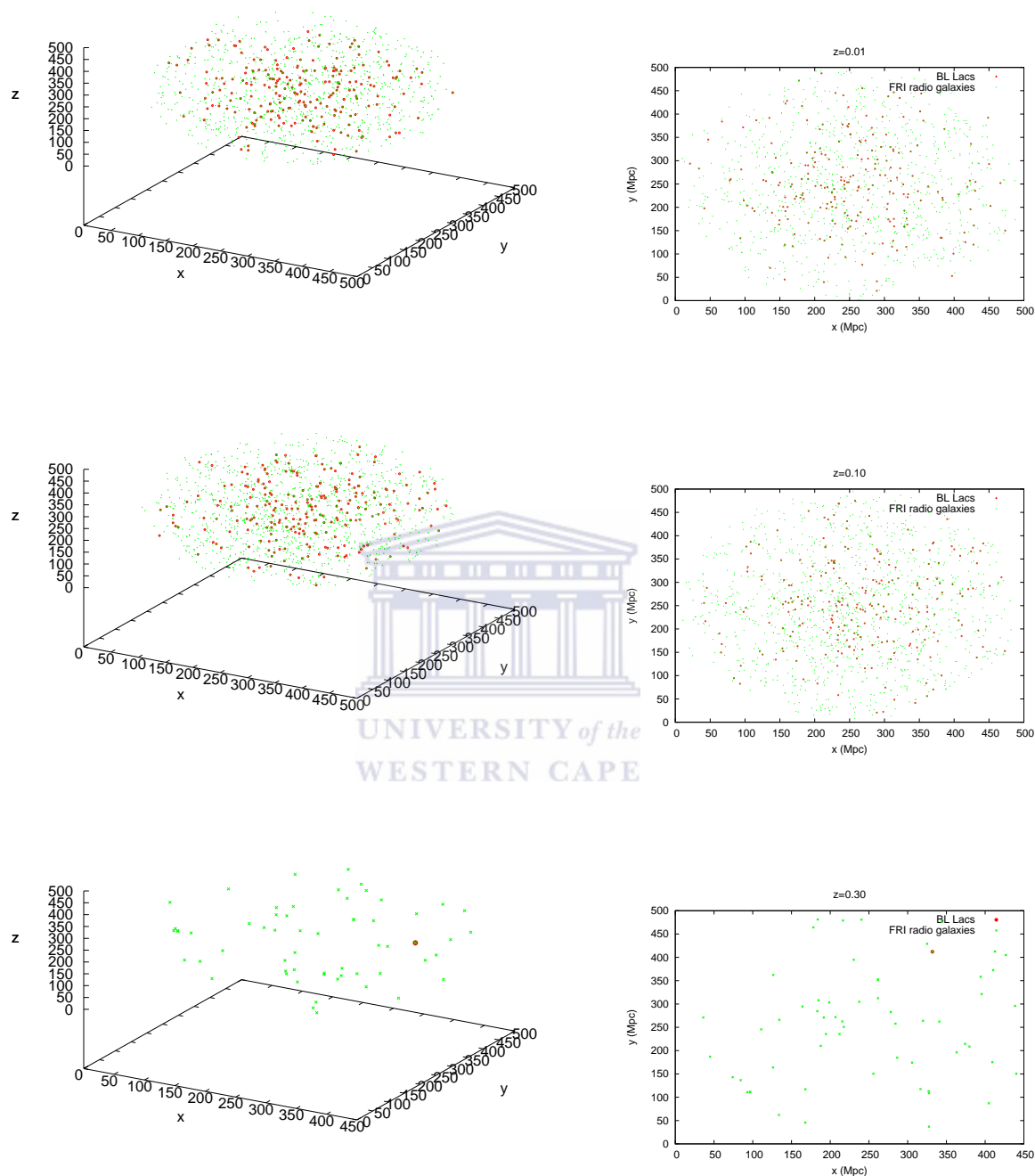


**Figure 4.3:** Spatial distribution of BL Lacs and FRI at different redshift. The left panels are the 3D distributions and the right panels are the corresponding 2D projections. BL Lacs objects are shown as red circles and FRI radio galaxies as green dots.

We show in Figure (4.5) the distribution of the black hole mass accretion  $\Delta M$  for steep and flat spectrum radio sources at different redshift.  $\Delta M$  is the black hole mass change in the

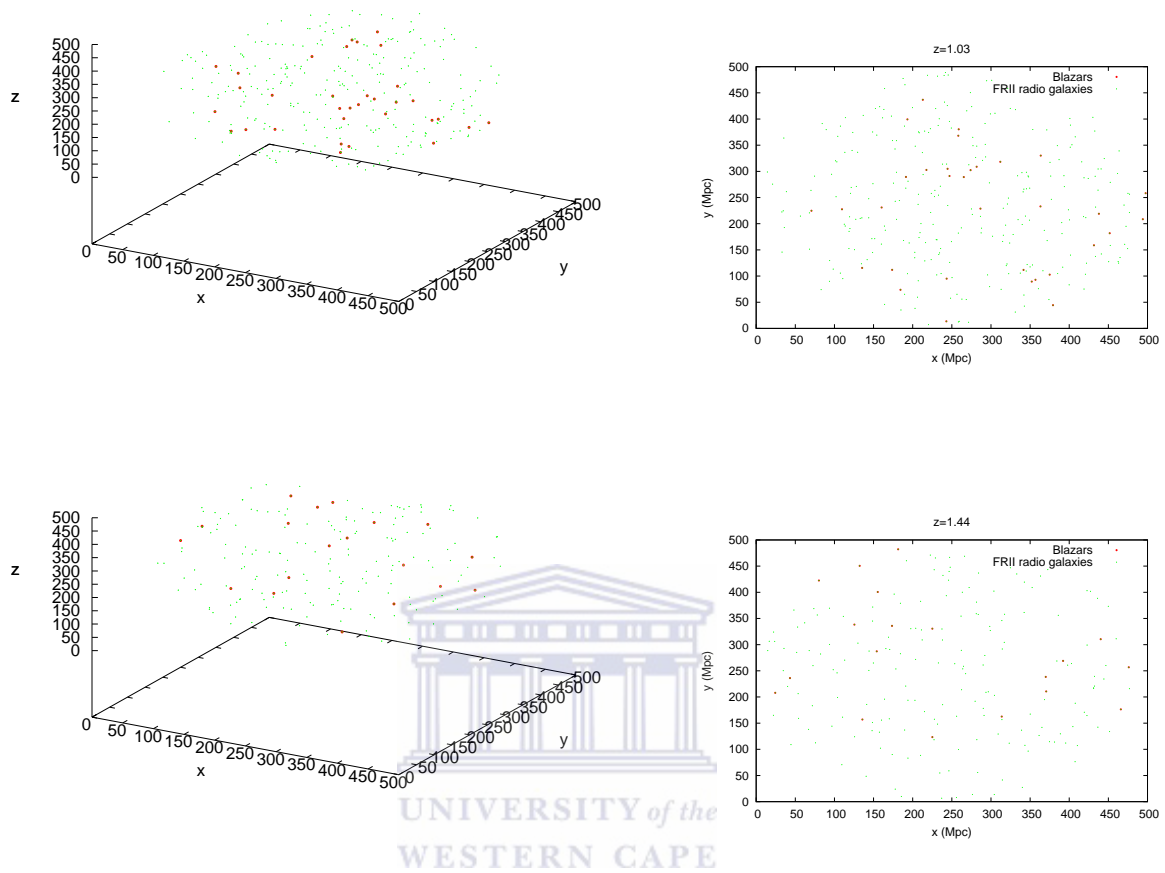


**Figure 4.4:** Spatial distribution of blazars and FR II at different redshift. The left panels are the 3D distributions and the right panels are the corresponding 2D projections. Blazars are shown as red circles and FR II radio galaxies as green dots.

timestep of the simulation which corresponds to the time between one snapshot and the next one. The black hole distribution has the shape of a gaussian distribution for steep spectrum radio sources.

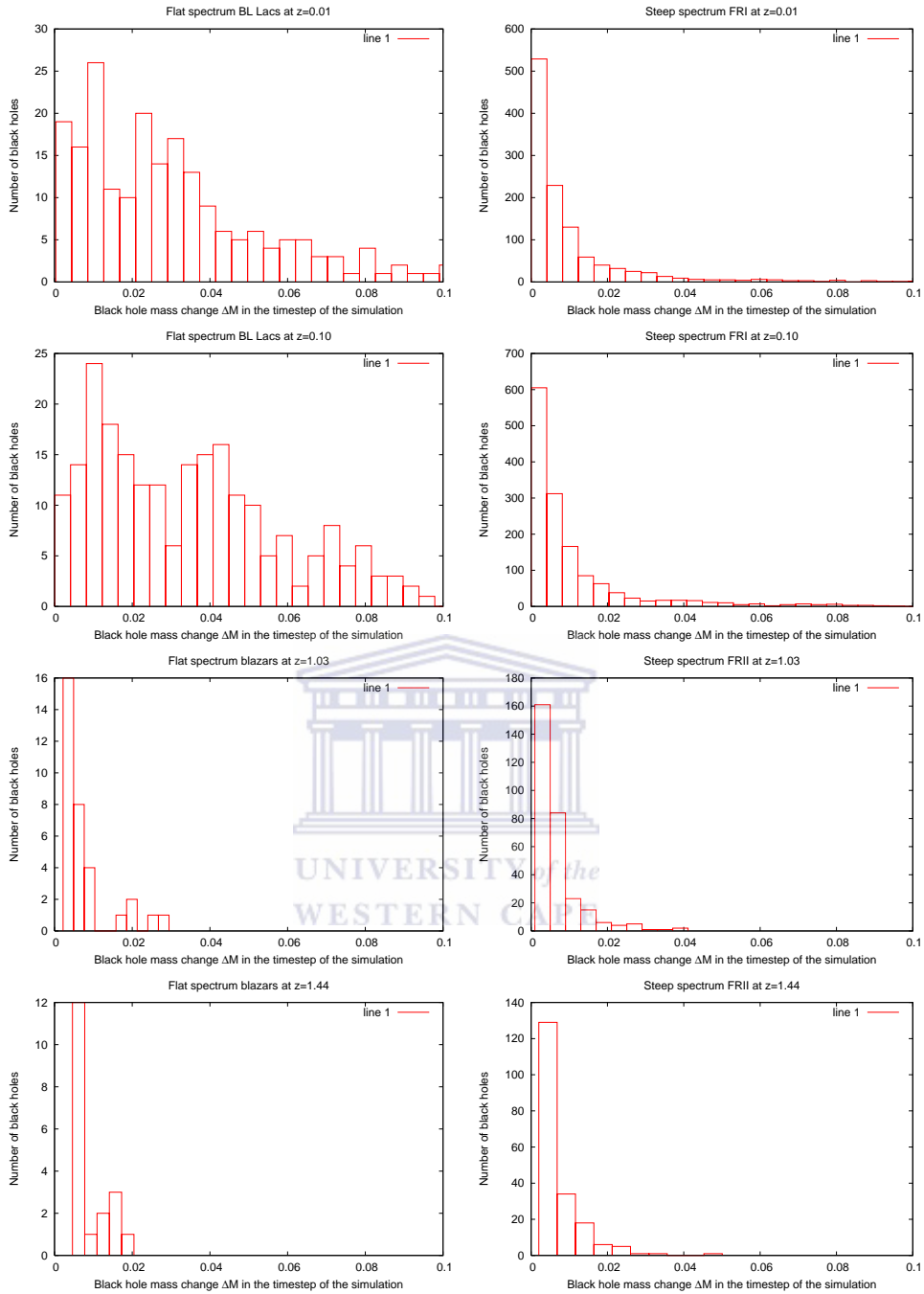


**Figure 4.5:** Distribution of the black hole mass accretion at different redshift respectively for flat spectrum radio sources BL Lacs, blazars (left panels) and steep spectrum radio sources FRI, FRII (right panels). The rows correspond respectively to redshifts  $z = 0.01, 0.10, 1.03, 1.44$ .  $\Delta M$  ( $10^{10}h^{-1}M_{\odot}$ ) is the difference between the descendant black hole mass and the progenitor black hole mass in the timestep of the simulation. The distribution of the black hole mass accretion for FRI and FRII can be approximated by a gaussian.

## 4.5 Radial distribution of radio sources in clusters

Lin and Mohr (2007) [58] did a statistical study of the properties of radio galaxies in nearby clusters ( $z \leq 0.2$ ). We display their results in Figure (4.6) which shows the surface density profile of radio sources in clusters of redshift up to  $z = 0.0647$ . The sample includes 573 clusters detected in the X-ray and observed at the frequency 1.4 GHz in the NRAO VLA Sky Survey (NVSS). The radio sources luminosity is  $P \geq 10^{23} \text{ WHz}^{-1}$  and sources out to  $5r_{200}$  from the cluster centre are shown in the plot. This lower luminosity limit corresponds to  $S \simeq 10 \text{ mJy}$  at  $z = 0.0647$ .

The surface density of the sources in the cluster is composed into a cluster and a background component. Lin and Mohr (2007) [58] consider sources out to  $5r_{200}$  from the centre of the cluster to allow a better determination of the background value. They use the “universal” profile of Navarro et al. (1997) [73] to model the spatial distribution of radio sources in clusters. The best fit models for the cluster and background shown in Figure (4.6) (left panel) are obtained by minimizing the  $\chi^2$ . Lin and Mohr (2007) [58], following Gehrels (1986) [45], estimate the uncertainty in each radial bin by assuming Poisson statistics.

We show in Figure (4.6) the comparison with our model. We use the snapshots 61 ( $z \simeq 0.041$ ) and 60 ( $z \simeq 0.064$ ) that give a mean redshift  $z \simeq 0.053$  for the galaxies in the Millennium volume. After stacking the data we plotted the total surface density against the radius from the cluster centre normalized by  $r_{200}$  (radius within which the density is 200 times the critical density, Section (2.6.4)). The idea is to slice the clusters into a set of concentric shells and use  $r_{200}$  (which is proportional to the virial radius  $r_{\text{vir}}$ ) as a scaling reference in order to make different objects comparable since the clusters are different in size. We calculate the virial radius with the formula given in Section (3.9)

$$r_{\text{vir}} = 259 \left( \frac{M_{\text{vir}}}{10^{12} M_{\odot}} \right)^{\frac{1}{3}} \text{ kpc} \quad (4.4)$$

where  $M_{\text{vir}}$  is the virial mass of the cluster. Following Cupani et al. (2008) [33] we use the average ratios  $\frac{r_{\text{vir}}}{r_{200}}$  and  $\frac{M_{\text{vir}}}{M_{200}}$ <sup>1</sup> of galaxy clusters:

$$\frac{r_{\text{vir}}}{r_{200}} = 1.36 \pm 0.04, \quad (4.5)$$

$$\frac{M_{\text{vir}}}{M_{200}} = 1.26 \pm 0.11 \quad (4.6)$$

since many authors prefer to use  $r_{200}$  and  $M_{200}$  instead of  $r_{\text{vir}}$  and  $M_{\text{vir}}$ . The surface density profile of BL Lacs and FRI radio galaxies with a luminosity limit  $P \geq 10^{23} \text{ W Hz}^{-1}$  at 1.4 GHz and at redshift  $z \simeq 0.053$  is shown on Figure (4.6). Using the scaling relation (4.4) we find a virial radius range from 1.68 Mpc to 3.76 Mpc. We can see in Figure (4.6) that

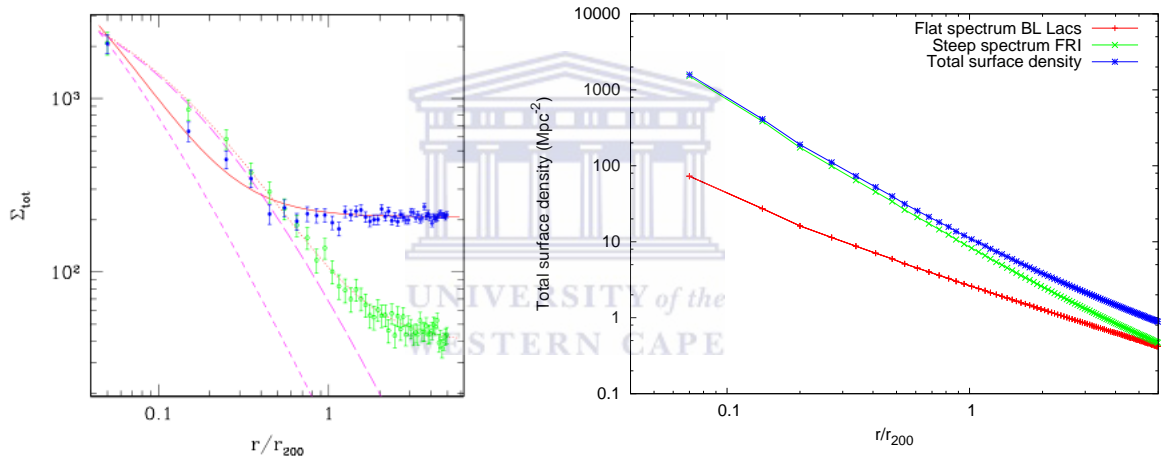


**Figure 4.6:** Surface density profiles of radio sources and galaxies in clusters. The upper limit of clusters redshift is  $z = 0.0647$  and the lower limit of radio sources luminosity at 1.4 GHz is  $P_{\text{min}} = 10^{23} \text{ WHz}^{-1}$ . In the left panel is shown the model of Lin and Mohr (2007) [58]. The blue solid points are the radio sources and the green hollow points are galaxies more luminous than  $M_{\text{K}} = -24$ . The red solid line corresponds to the best-fit total profile that includes the cluster and background. The best-fit cluster model is shown as a cyan short dashed line. The cyan dotted line is the best-fit model for the galaxies (green) total profile and the cyan long dashed line is the best-fit model for the cluster profiles. The right panel shows the surface density profile of BL Lacs modelled using the Mkn 501 template SED in red line and FRI in green line. The total surface density profile of BL Lacs and FRI radio galaxies is shown in blue line.

our model is in good agreement with Lin & Mohr (2007) [58] out to  $0.1r_{200}$ . It shows that radio galaxies are more concentrated near the centre of the cluster with a maximum  $\sim 1500 \text{ Mpc}^{-2}$  at  $0.07r_{200}$ . In the outskirts of the clusters ( $r > 0.1r_{200}$ ) our model underestimates

<sup>1</sup> $M_{200}$  is the mass within the radius  $r_{200}$ .

the number of radio galaxies. We can explain this by the particular choice of the SED of the radio galaxies that we use in the model. In our modelling we take the average luminosity of radio sources to compute the parameters like the number density and surface density. The consequence of this is that the model prediction is only good within uncertainty with that choice. The parameters estimates depend strongly on the luminosity of the radio sources through the accretion efficiency which varies also with the redshift. FRI 3C 338 was chosen as a representative of the steep spectrum radio galaxies (at  $z = 0.0304$  which is a reasonable approximation of the maximum redshift  $z = 0.0647$  of cluster radio sources of Lin & Mohr (2007) [58]) because of its average luminosity while the radio sources probed by Lin & Mohr (2007) [58] have a radio luminosity  $P \geq 10^{23} \text{ W Hz}^{-1}$ . The same applies for the flat spectrum radio sources. This low luminosity blazar at  $z=0.034$  as discussed in Cao (2003) [19] is triggered by low mode accretion and low radiative efficiency with  $\frac{L_{\text{bol}}}{L_{\text{Edd}}} \sim 10^{-4}$ . In addition at the radio-power  $P \geq 10^{23} \text{ W Hz}^{-1}$ , the sample of radio sources in Lin & Mohr (2007) [58] contains more FR II type radio galaxies than there are in our model. Taking in consideration all of this we can expect this difference in the surface density of radio sources due to the smaller number of radio galaxies in our model. We do not include in this model FR II and blazars that are triggered by quasar mode accretion since they are inefficient at low redshift (here  $z_{\text{max}} = 0.0647$ ).

Now we present in Figure (4.7) the surface density profiles for different scaling of the virial radius and for different redshift. For radio mode accretion we did not find BL Lacs and FRIs for redshift  $z \gtrsim 0.48$  using our template SEDs. Some of these radio sources might be triggered by quasar mode accretion but since we do not have enough information about the accretion efficiency at this intermediate redshift we have not included this in the model. One way to improve agreement with observations is to increase the efficiency parameter with redshift or choose a different SED for flat and steep spectrum BL Lacs and FRIs.

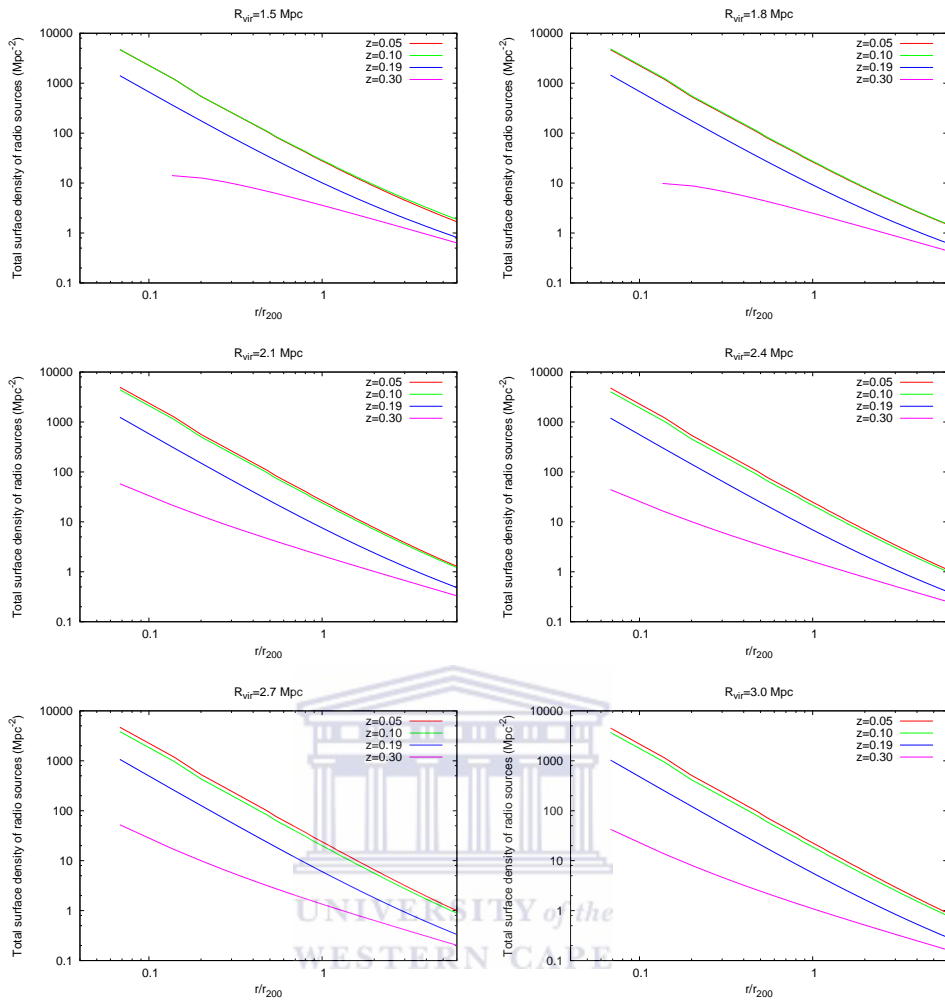


**Figure 4.7:** Total surface density profiles of BL Lacs and FRI radio galaxies with a flux limit  $S = 10$  mJy at 1.4 GHz. Each panel corresponds to clusters with virial radius  $R_{\text{vir}} = 1.5, 1.8, 2.1, 2.4, 2.7, 3.0$  Mpc and the profiles are shown at redshift  $z = 0.05, 0.10, 0.19, 0.30$ . The density of radio sources in clusters observed above a given flux cut-off (10 mJy), is much lower at higher redshift and they are concentrated close to the centre of the cluster at  $r \lesssim 0.1r_{200}$ .

The scaling to massive clusters results in much lower density of the radio sources and this becomes more significant in the outskirts of the cluster ( $r \gtrsim r_{200}$ ) and at higher redshift (Figure (4.8)). We can see in Figure (4.9) that radio sources are more concentrated in low mass clusters and the density is maximum near the centre ( $r \lesssim 0.1r_{200}$ ). For a given cluster mass, radio sources are more concentrated at low redshift.



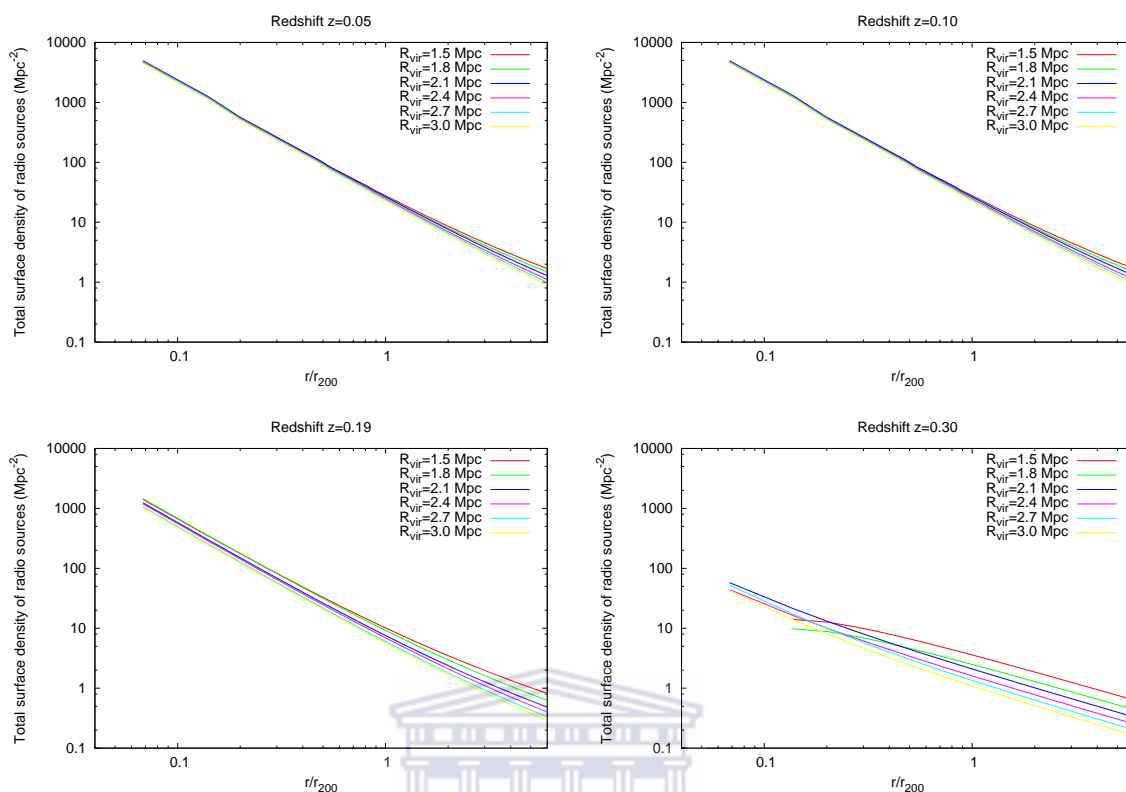


**Figure 4.8:** Total surface density profiles of BL Lacs and FRI radio galaxies with a flux limit  $S = 10$  mJy at 1.4 GHz. Each panel shows the effect of the virial radius scaling at respectively redshift  $z = 0.05, 0.10, 0.19, 0.30$ .

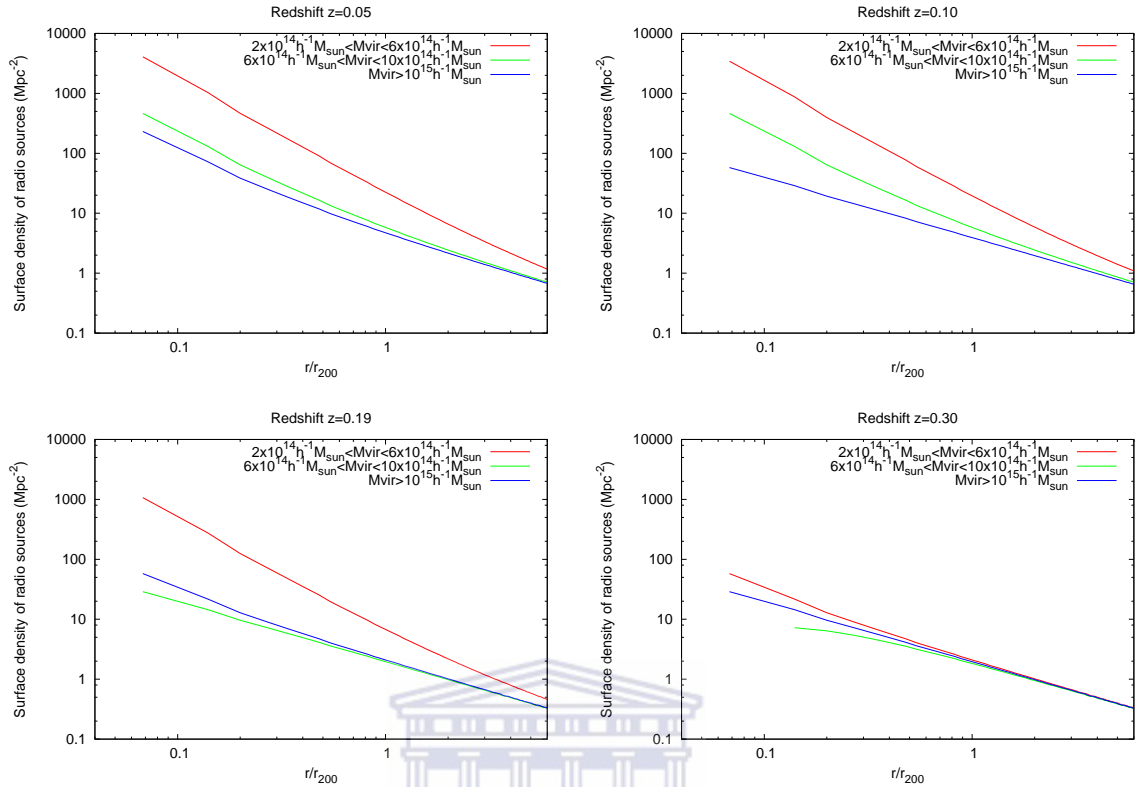


**Figure 4.9:** Surface density profiles of BL Lacs and FRI radio galaxies with a flux limit  $S = 10$  mJy at 1.4 GHz for different virial mass bins of cluster radio sources  $2 \times 10^{14} h^{-1} M_{\odot} < M_{\text{vir}} < 6 \times 10^{14} h^{-1} M_{\odot}$ ,  $6 \times 10^{14} h^{-1} M_{\odot} < M_{\text{vir}} < 10^{15} h^{-1} M_{\odot}$ , and  $M_{\text{vir}} > 10^{15} h^{-1} M_{\odot}$ . Each panel corresponds respectively to the density profiles at redshift  $z = 0.05, 0.10, 0.19, 0.30$  scaled to the mean virial radius  $r_{\text{vir}} = 2.1$  Mpc ( $r_{200} \simeq 1.5$  Mpc) of the clusters in the corresponding snapshot.

## 4.6 Temperature fluctuations and fluxes

We now calculate the average temperature fluctuations and fluxes due to radio sources in clusters. We consider mainly the population of flat spectrum radio sources constituted by blazars. They are mostly triggered by radio mode accretion and therefore we compute their contributions at lower redshifts ( $z < 1$ ). We study the contamination at different redshift and for different clusters mass bins. The frequencies of observations are the three ACT bands of frequencies 145 GHz, 220 GHz and 270 GHz. The corresponding temperature fluctuations and fluxes are shown in Figure (4.10). We divide the virial mass of the clusters into three mass bins  $2 \times 10^{14} h^{-1} M_{\odot} < M_{\text{vir}} < 6 \times 10^{14} h^{-1} M_{\odot}$ ,  $6 \times 10^{14} h^{-1} M_{\odot} < M_{\text{vir}} < 10^{15} h^{-1} M_{\odot}$  and  $M_{\text{vir}} > 10^{15} h^{-1} M_{\odot}$  to see how clusters masses contribute to the fluctuations. As we can see in the Figure (4.10), radio sources contamination is more significant for large mass bins. The

model predicts the maximum fluctuations at redshift  $z = 0.1$ . We assumed that all radio sources have the average SED of the BL Lacs MKn 501. In reality we should consider an appropriate SED for each redshift and a known value of the accretion efficiency constrained by observations and then compute the fluctuation parameters. We can see in Figure (4.11) and Table (B.1) given in the appendix that the temperature fluctuations are increasing with the frequency whereas the fluxes of radio sources are larger for a lower frequency. The displayed values of the virial mass in the first column of Tables (B.1), (4.8) and (4.9) are rounded to three decimal places so that some virial masses are repeated and have different values in other columns. In that case the corresponding temperature fluctuations and fluxes are the mean values.

We show in Table (4.8) the average temperature fluctuations and fluxes at  $z = 0.48$ . As the redshift is increasing the radio mode accretion of BL Lacs becomes less efficient and as our model predicts smaller number density of flat spectrum radio sources at this intermediate redshift we expect smaller fluctuations. The values we obtained here are an underestimation of the contaminations since we expect more FRI radio galaxies at  $z = 0.48$ . This can be explained by the accretion efficiency ( $\varepsilon = 10^{-4}$ ) that we kept constant for all redshifts in the range  $z < 1$ . It means that at  $z = 0.48$  the accretion of hot gas in less luminous blazars should be  $\varepsilon > 10^{-4}$ . We now look at the mean temperature fluctuations and the corresponding fluxes due to brighter blazars. We assume an average SED of high luminosity blazars. As they are triggered by major mergers their mode of growth is the quasar mode accretion which is effective at high redshift  $z \gtrsim 1$ . We show in Table (4.9) the fluctuations due to blazars in clusters with a virial mass  $M_{\text{vir}} \geq 2 \times 10^{14} h^{-1} M_{\odot}$  at the redshift  $z = 1.44$ . At this snapshot there are two massive radio clusters ( $M_{\text{vir}} > 3 \times 10^{14} h^{-1} M_{\odot}$ ) which might contaminate significantly the SZE measurements. Massive clusters are rare at high redshift but Table (4.9) shows that for the most massive of them the contamination is non negligible. In our case the two clusters with a virial mass respectively  $3.257 \times 10^{14} h^{-1} M_{\odot}$  and  $6.125 \times 10^{14} h^{-1} M_{\odot}$  will be lost in the SZ survey as the temperature and fluxes of radio sources are much higher than the expected SZ measurements of these clusters. This assumes that the accretion efficiency at  $z = 1.44$  and with the high luminosity blazars (adopted from the SED) is the standard

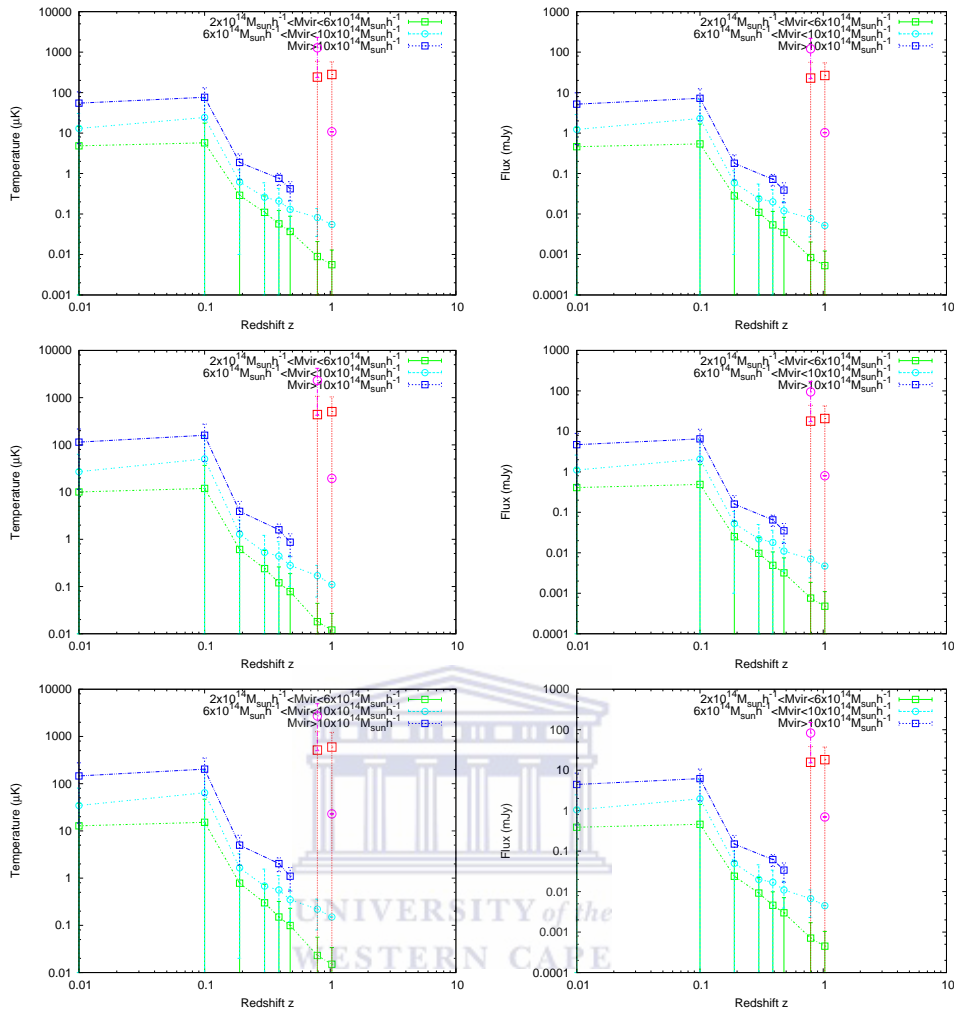


**Figure 4.10:** Average temperatures (left panels) and fluxes (right panels) as a function of redshift for different cluster virial mass bins at respectively from top to bottom panels 145 GHz, 220 GHz and 270 GHz. The temperature fluctuations and fluxes of high luminosity blazars are shown for the redshift  $z = 0.79$  and  $z = 1.03$  where quasar mode accretion is more effective (red squares are for  $2 \times 10^{14} h^{-1} M_{\odot} < M_{\text{vir}} < 6 \times 10^{14} h^{-1} M_{\odot}$  and magenta circles are for  $6 \times 10^{14} h^{-1} M_{\odot} < M_{\text{vir}} < 10^{15} h^{-1} M_{\odot}$ ). Blue, cyan and green circles and squares are the temperature fluctuations and fluxes of low luminosity blazars (BL Lacs) that undergo radio mode accretion. Beyond  $z = 1.03$  the model underestimates the temperature and flux distributions. The errorbars are the deviations from the average temperatures and fluxes of clusters in each mass bin.

value  $\varepsilon = 0.1$ . This result is preliminary and will be explored further in the future.

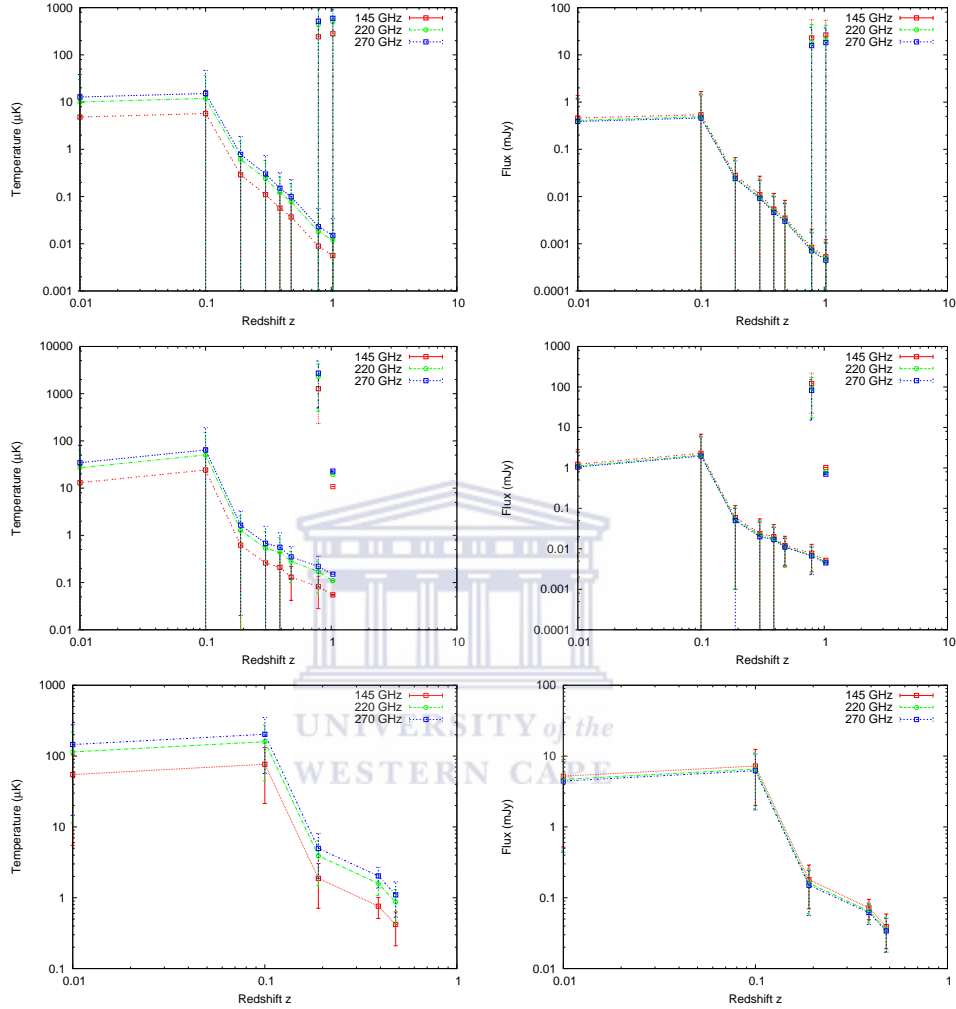


**Figure 4.11:** Average temperatures (left panels) and fluxes (right panels) as a function of the redshift for cluster virial mass bins respectively from top to bottom panels  $2 \times 10^{14} h^{-1} M_{\odot} < M_{\text{vir}} < 6 \times 10^{14} h^{-1} M_{\odot}$ ,  $6 \times 10^{14} h^{-1} M_{\odot} < M_{\text{vir}} < 10^{15} h^{-1} M_{\odot}$  and  $M_{\text{vir}} > 10^{15} h^{-1} M_{\odot}$  at 145 GHz, 220 GHz and 270 GHz. For a given cluster virial mass bin the temperature fluctuations are increasing with the frequency. The deviations from the mean are smaller for the most massive clusters. The squares and circles with no dashed-lines in the top right corner of each plot are the distributions corresponding to high luminosity blazars triggered by quasar mode accretion. They are rare in massive clusters and at high redshift.

**Table 4.8:** *Temperature fluctuations and fluxes caused by BL Lacs low luminosity blazars at redshift  $z = 0.48$  at 145 GHz, 220 GHz and 270 GHz. The clusters virial masses considered here are for clusters with  $M_{\text{vir}} \geq 2 \times 10^{14} h^{-1} M_{\odot}$  and with radio sources temperature fluctuations at least  $0.1 \mu\text{K}$ .*

$M_{\text{vir}} (10^{14} h^{-1} M_{\odot})$	$T_{145\text{GHz}} (\mu\text{K})$	$S_{145\text{GHz}} (\text{mJy})$	$T_{220\text{GHz}}$	$S_{220\text{GHz}}$	$T_{270\text{GHz}}$	$S_{270\text{GHz}}$
2.340	0.1	0.01	0.3	0.01	0.4	0.01
2.400	0.3	0.03	0.6	0.02	0.7	0.02
2.440	0.1	0.01	0.2	0.01	0.2	0.01
2.490	0.1	0.01	0.2	0.01	0.3	0.01
2.630	0.1	0.01	0.2	0.01	0.3	0.01
3.200	0.1	0.01	0.3	0.01	0.3	0.01
3.560	0.1	0.01	0.3	0.01	0.3	0.01
3.690	0.1	0.01	0.3	0.01	0.3	0.01
3.720	0.2	0.02	0.4	0.02	0.5	0.01
3.900	0.1	0.01	0.6	0.02	0.8	0.02
3.900	0.3	0.03	0.6	0.02	0.8	0.02
4.070	0.1	0.01	0.3	0.01	0.3	0.01
4.680	0.1	0.01	0.3	0.01	0.4	0.01
5.040	0.3	0.03	0.7	0.03	0.9	0.03
5.280	0.2	0.02	0.4	0.02	0.5	0.02
6.130	0.3	0.02	0.5	0.02	0.7	0.02
6.420	0.2	0.02	0.4	0.01	0.5	0.01
10.860	0.2	0.02	0.5	0.02	0.6	0.02
11.160	0.7	0.07	1.5	0.06	1.9	0.06
17.240	0.3	0.03	0.6	0.03	0.8	0.03

**Table 4.9:** *Temperature fluctuations and fluxes caused by blazars at redshift  $z = 1.44$  at 145 GHz, 220 GHz and 270 GHz. The clusters virial masses shown here are for clusters with  $M_{\text{vir}} \geq 2 \times 10^{14} h^{-1} M_{\odot}$  and with radio sources temperature fluctuations at least  $0.1 \mu\text{K}$ .*

$M_{\text{vir}} (10^{14} h^{-1} M_{\odot})$	$T_{145\text{GHz}} (\mu\text{K})$	$S_{145\text{GHz}} (\text{mJy})$	$T_{220\text{GHz}}$	$S_{220\text{GHz}}$	$T_{270\text{GHz}}$	$S_{270\text{GHz}}$
2.112	4.04	0.38	7.29	0.3	8.59	0.26
2.187	2.06	0.19	3.71	0.15	4.37	0.13
2.275	2.44	0.23	4.41	0.18	5.2	0.16
3.257	559.6	52.85	1010.27	41.43	1190.17	36.28
6.125	111.92	10.57	202.05	8.29	238.03	7.26

## Chapter 5

### Conclusion

We have used the Millennium simulation (Springel et al. (2005) [106]) outputs to build a model for radio-emitting AGN based on semi-analytic model of galaxy formation and evolution by De Lucia et al. (2004) [37]. Two modes of BH growth are important: radio mode accretion and quasar mode accretion. The quasar mode accretion is the dominant mode of black hole growth and more effective at  $z \gtrsim 1.0$  and for massive black holes  $M \gtrsim 10^8 M_\odot$ , while the radio mode is only effective at low redshifts. We obtained from the model the fraction of the total bolometric luminosity of the black hole which is turned into radio luminosity by assuming an average spectral energy distribution of the radio source. We have separately studied the distribution in cosmic time of low luminosity radio sources (BL Lacs and FRI radio galaxies) and high luminosity radio sources (blazars and FRII radio quasars). We assumed that the former are triggered by the radio mode accretion with radiatively inefficient accretion and the latter are triggered by major mergers, with the standard accretion efficiency  $\varepsilon \simeq 0.1$ . The redshift distribution of the simulated radio sources was compared with that of Dunlop & Peacock (1990) [39] model (Section (4.3)) which is consistent with recent data (CENSORS, Brookes et al. (2008) [18]). Then we reviewed the distribution of radio sources in massive clusters (Section (4.4) and (4.5)) with a minimum virial mass  $2 \times 10^{14} h^{-1} M_\odot$  as this is the mass threshold of the ACT experiment for the SZE galaxy clusters survey. We did an estimation of the temperature fluctuations in CMB caused by the radio point sources and computed the corresponding fluxes (Section (4.6)) at different

## Conclusion

---

redshift and then identified the contaminants for the SZE signature of galaxy clusters.

We found in this work that our extended semi-analytic model is able to reproduce, within the error bars, the shape of the observed redshift distribution which is best described by the model RLF5 of Dunlop & Peacock (1990) [39]. The match is not very good at higher redshift ( $z \gtrsim 1$ ) due to the uncertainty on the value of the accretion efficiency which is not yet well constrained by observations. We can improve the model by assuming an accretion efficiency which increases with redshift as it was suggested in the dynamical model of Croton (2006) [31]. Mo et al. (1998) [71] in addition claimed that disks of galaxies were more centrally concentrated in the past making the feeding of the black hole more efficient in the past. However we did not attempt to follow this prescription since the accretion efficiency depends not only on redshift but also with the black hole mass, the luminosity and its spins (see e. g. Volonteri et al. (2007) [117]) and is beyond the scope of this work.

We found that radio galaxies and blazars are concentrated near the centre of clusters at a distance  $r \lesssim 0.1r_{200}$  and they are more concentrated in low mass clusters. The total surface density profile of radio sources with a luminosity cut-off  $P \geq 10^{23} \text{ W Hz}^{-1}$  at 1.4 GHz at  $r \lesssim 0.1r_{200}$  is in good agreement with the model of Lin & Mohr (2007) [58]. The model underestimates the number of radio sources in the outskirts of clusters. There is a rapid drop off in FRI space density at redshift  $z \gtrsim 0.2$ . Both of these problems may be related to our assumption of a constant accretion efficiency.

Our model predicts a non negligible contamination of clusters SZE signature at redshift  $z \lesssim 0.1$ . The contaminants at this redshift made up with BL Lacs and FRI produce an average fluctuation in CMB temperature of orders  $5 \mu\text{K}$  for lower mass cluster to  $\sim 45 \mu\text{K}$  for massive clusters at 145 GHz. This is at the same or above the level of the kinetic SZE expected for such clusters which is a few tens  $\mu\text{K}$ . At high redshifts  $z \simeq 0.79$  and  $z \simeq 1.03$ , our model suggests that blazars produce fluctuations of  $300 - 350 \mu\text{K}$  for an average cluster mass which is larger than the expected thermal SZE signal of hundreds  $\mu\text{K}$ , but these results are preliminary which need further testing.



## Conclusion

---

The temperature fluctuations and fluxes caused by radio sources in galaxy clusters at the ACT frequencies can be modelled by a power law but before doing this we need to improve the model by adopting different shape of the spectral energy distribution of blazars and radio galaxies and choose an accretion efficiency that is constrained by observation. In future work it is really important to know how the accretion parameter which determines the efficiency of the conversion of mass to radiation varies with the central black hole properties.



# Bibliography

- [1] Alexander P., Leahy J. P. 1987. Ageing and speeds in a representative sample of 21 classical double radio sources. MNRAS 225: 126.
- [2] Allen S. W., Fabian A. C. 1998. The impact of cooling flows on the  $T_x - L_{Bol}$  relation for the most luminous clusters. MNRAS 297: L57 - L62.
- [3] Bagla J. S. 2002. TreePM: a code for cosmological N-body simulations. Journal of Astrophysics and Astronomy 23, 185-196.
- [4] Barnes J., Hut P. 1986. A hierarchical  $O(N \log N)$  force-calculation algorithm. Nature 324, 446-449.
- [5] Bechtold J. et al. 1994. Infrared to X-ray spectral energy distributions of high redshift quasars. The Astronomical Journal, vol. 108, no. 2, p. 374-394.
- [6] Bennett C. et al. 1992. Preliminary separation of the galactic and cosmic microwave background emission for the COBE differential microwave radiometer. ApJ, 396, L7-L12.
- [7] Bennett C. et al. 2003. First-Year Wilkinson Microwave Anisotropy Probe (WMAP) Observations: Foreground Emission. ApJS 148, 97.
- [8] Bertschinger E. 1989. The evolution of cooling flows - Self-similar cooling waves. ApJ, 340, 666.
- [9] Binney J. 1977. The physics of dissipational galaxy formation. ApJ, 215, 483.

## BIBLIOGRAPHY

---

- [10] Bird J. C., Martini P., Kaiser C. R. 2008. The lifetime of FR II sources in groups and clusters: implications for radio mode feedback. *ApJ*, 676, 147.
- [11] Birkinshaw M. 1990. *The CMB: 25 years later*. Ed. N. Mandolesi, N. Vittorio, pp. 77-94, Dordrecht, Kluwer.
- [12] Birkinshaw M. 1999. The Sunyaev-Zeldovich effect. *Physics Reports* 310:97-195.
- [13] Bode P., Ostriker J. P. 2003. Tree-Particle-Mesh: An Adaptive, Efficient, and Parallel Code for Collisionless Cosmological Simulation. *ApJS*, 145, 1.
- [14] Bode P., Ostriker J. P., Xu G. 2000. The Tree Particle-Mesh N-body gravity solver. *Astrophys. J. Suppl.* 128, 561-569.
- [15] Bolton J.G., Stanley G. J., Slee O. B. Positions of Three Discrete Sources of Galactic Radio-Frequency Radiation. *Nature* 164, 101.
- [16] Booth C. M., Schaye J. 2009. Cosmological simulations of the growth of supermassive black holes and feedback from active galactic nuclei: method and tests. arXiv: 0904.2572.
- [17] Boyle B. J., Couch W. J. 1993. The environments of optically selected QSOs at  $0.9 < z < 1.5$ . *MNRAS* 264, 604.
- [18] Brookes M. H., Best P. N., Peacock J. A. et al. 2008. A Combined EIS-NVSS Survey of Radio Sources (CENSORS) III: spectroscopic observations. arXiv: 0802.1158v1.
- [19] Cao X. 2003. Jet formation in BL Lacertae objects with different accretion modes. *The Astrophysical Journal*, 599:147154.
- [20] Cao X., Li F. 2008. Rapidly spinning massive black holes in active galactic nuclei: evidence from the black hole mass function. *MNRAS*, 390, 561.
- [21] Capetti A., Trussoni E. et al., 2000. SEDs of FR I nuclei and FR I/ BL Lac unifying model. *MNRAS* 318, 493-500.

## BIBLIOGRAPHY

---

- [22] Carlstrom J. E., Holder G. P., Reese E. D. 2002. Cosmology with the Sunyaev-Zeldovich effect. astro-ph/0208192v1.
- [23] Colafrancesco S., Giommi P. 2006. Blazars and cosmic backgrounds. *Chin. J. Astron. Astrophys.* Vol 6, Suppl. 1, 47-56.
- [24] Cole S., Aragon-Salamanca A., Frenk C.S., Navarro J.F., Zepf S.E. 1994. A recipe for galaxy formation. *MNRAS*, 271, 781.
- [25] Cole S., Lacey C. G., Baugh C. M., Frenk C. S. 2000. Hierarchical galaxy formation. *MNRAS*, 319, 168.
- [26] Coles P., Lucchin F. 2002. *Cosmology: the Origin and Evolution of Cosmic Structure*. Wiley, Chichester, 2nd edition.
- [27] Collin S., Huré J. 2001. Size-Mass-luminosity relations in AGN and the role of the accretion disc. astro-ph/0109513v1.
- [28] Conway J. E. 2002. Compact symmetric objects - newborn radio galaxies? *New Astronomy Reviews* 46: 263271.
- [29] Costamante L., Ghisellini G. 2002. TeV candidate BL Lacs objects. *A & A* 384, 5671.
- [30] Croom S.M., Boyle B.J., Shanks T., Smith R.J., Miller L., Outram P.J., Loaring N.S., Hoyle F., Da Angela J. 2005. The 2dF QSO Redshift Survey - XIV. Structure and evolution from the two-point correlation function. *MNRAS*, 356, 415.
- [31] Croton D. J. 2006. Evolution in the black hole mass-bulge mass relation: a theoretical perspective. *MNRAS*, 369, 1808.
- [32] Croton D. J., Springel V., White S. D. M., De Lucia G., Frenk C. S., Gao L., Jenkins A., Kauffmann G., Navarro J. F., Yoshida N. 2005. The many lives of AGN: cooling flows, black holes and the luminosities and colours of galaxies. *MNRAS*, 365, 11.
- [33] Cupani G., Mezzetti M., Mardirossian F., 2008. Mass estimation in the outer non-equilibrium region of galaxy clusters. arXiv: 0807.3239v1.

## BIBLIOGRAPHY

---

- [34] Davies R. et al. 2007. Nearby Active Galactic Nuclei. Max-Planck-Institut für extraterrestrische Physik.
- [35] Davis M., Efstathiou G., Frenk C. S., White S. D. M. 1985. The Evolution of Large-Scale Structure in a Universe Dominated by Cold Dark Matter. *ApJ*, 292, 371.
- [36] De Lucia G., Blaizot J. 2006. The hierarchical formation of the brightest cluster galaxies. *MNRAS*, 375, 2.
- [37] De Lucia G., Kauffmann G., White S. D. M. 2004. Chemical enrichment of the intracluster and intergalactic medium in a hierarchical galaxy formation model. *MNRAS*, 349, 1101.
- [38] Di Matteo T., Springel V. and Hernquist L. 2005. Energy input from quasars regulates the growth and activity of black holes and their host galaxies. *Nature*, 433, 604.
- [39] Dunlop J. S., Peacock J. A. 1990. The redshift cut-off in the luminosity function of radio galaxies and quasars. *MNRAS* 247, 19-42.
- [40] Elvis M., Risaliti G., Zamorani G. 2002. Most supermassive black holes must be rapidly rotating. *ApJ*, 565, L75.
- [41] Feroz F., Hobson M. P et al. 2008. Bayesian modelling of clusters of galaxies from multi-frequency pointed Sunyaev-Zeldovich observations. arXiv: 0811.1199v1.
- [42] Field G. B., Hitchcock J. L. 1966. Cosmic black body radiation at  $\lambda = 2.6$  mm. *Phys. Rev. Lett.* 16, 817.
- [43] Fossati G., Maraschi L., Celotti A., Comastri A., Ghisellini G. 1998. A unifying view of the spectral energy distributions of blazars. *MNRAS*, 299, 433.
- [44] Fujita Y., Takahara F. 1999. Cosmological implications of the fundamental relations of X-ray clusters. *The Astrophysical Journal*, 519:L55-L58.
- [45] Gehrels N., 1986. Confidence limits for small numbers of events in astrophysical data. *ApJ*, 303, 336.

## BIBLIOGRAPHY

---

- [46] Heckman T. M. 1980. An optical and radio survey of the nuclei of bright galaxies- Activity in normal galactic nuclei. *Astronomy and Astrophysics* 87: 152-164.
- [47] Hockney R. W., Eastwood 1981. *Computer simulation using particles*. McGraw-Hill.
- [48] Hopkins P. F., Hernquist L., Cox T. J., Di Matteo T., Robertson B., Springel V. 2005. A unified, merger-driven model for the origin of starbursts, quasars, the cosmic X-ray background, supermassive black holes and galaxy spheroids. astro-ph/0506398v3.
- [49] Howell T. F., Shakeshaft J. R. 1966. Measurement of the minimum cosmic background radiation at 20.7 cm wavelength. *Nature*, 210, 1318.
- [50] Jackson C. A., Wall J. V. 1999. Extragalactic radio-source evolution under the dual-population unification scheme. *MNRAS*, 304, 160.
- [51] Jansky K. G. 1933. Radio waves from outside the solar system. *Nature*, 132, p66.
- [52] Kaiser C. R. 2000. The environments and ages of extragalactic radio sources inferred from multi-frequency radio maps. *A & A* 362: 447464.
- [53] Kauffmann G., Colberg J. M., Diaferio A., White S. D. M. 1999. Clustering of galaxies in a hierarchical Universe: I. Methods and results at  $z = 0$ . *MNRAS*, 303, 188.
- [54] Kellermann K. I., Owen F. N. 1988. *Radio galaxies and quasars. Galactic and Extragalactic Radio Astronomy*, 2nd edition.
- [55] Kosowsky A. 2004. *The Atacama Cosmology Telescope*. astro-ph/0402234v1.
- [56] Kurosawa R., Proga D., Nagamine K. 2009. On the feedback efficiency of active galactic nuclei. arXiv: 0906.3739v1.
- [57] Liddle A. 2003. *An introduction to modern cosmology*. Wiley, Chichester, 2nd edition.
- [58] Lin Y. T., Mohr J. J. 2007. Radio sources in galaxy clusters: radial distribution, and 1.4 GHz and K-band bivariate luminosity function. astro-ph/0612521v2.
- [59] Mack K. H., Klein U., O' Dea C. P., Willis A. G., Saripalli L. 1998. Spectral indices, particle ages, and the ambient medium of giant radio galaxies. *A& A* 329: 431442.

## BIBLIOGRAPHY

---

- [60] Magorrian J., Tremaine S., Richstone D., et al. 1998. The demography of massive dark objects in galaxy centers. *AJ*, 115, 2285.
- [61] Maraschi L. 2001. High energy phenomena in blazars. *astro-ph/0107565v1*.
- [62] Marconi A., Hunt L. K. 2003. The relation between black hole mass, bulge mass, and near-infrared luminosity. *ApJL*, 589, L21.
- [63] Martínez-Sansigre A., Taylor A.M. 2009. The cosmological consequence of an obscured AGN population on the radiation efficiency. *ApJ*, 692, 964.
- [64] Marulli F., Bonoli S., Branchini E., Moscardini L., Springel V. 2007. Modeling the cosmological co-evolution of supermassive black holes and galaxies: I. BH scaling relations and the AGN luminosity function. *astro-ph/0711.2053v1*.
- [65] Marulli F., Bonoli S., Branchini E., Moscardini L., Springel V. 2008. The cosmological co-evolution of supermassive black holes, AGN and galaxies. *arXiv: 0809.0640v1*.
- [66] Masetti N., Mason E., Landi R., Giommi P. et al. 2008. High-redshift blazar identification for Swift J1656.3-3302. *arXiv:0801.2976v1*.
- [67] Mather J. C., Cheng E. S., Cottingham D. A. et al. 1994. Measurement of the cosmic microwave background spectrum by the COBE FIRAS instrument. *Ap. J.* 420:4391.
- [68] Merloni A., Heinz S. 2008. A synthesis model for AGN evolution: supermassive black holes growth and feedback modes. *arXiv: 0805.2499v1*.
- [69] Meszaros P. 1975. Radiation from spherical accretion onto black holes. *A & A*, 44, 59.
- [70] Miller C. J., Nichol R. C., Gomez P. L., Hopkins A. M., & Bernardi M. 2003. The environment of AGNs in the Sloan Digital Sky Survey. *ApJ*, 597, 142156.
- [71] Mo H. J., Mao S., White S. D. M. 1998. The formation of galactic disks. *MNRAS*, 295, 319.
- [72] Mushotzky R. F., Scharf C. A. 1997. The luminosity-temperature relation at  $z = 0.4$  for clusters of galaxies. *ApJ*, 482: L13-L16.

## BIBLIOGRAPHY

---

- [73] Navarro J. F., Frenk C. S., White S. D. M. 1997. A universal density profile from hierarchical clustering. *ApJ*, 490, 493.
- [74] Nordberg H. P., Smoot G. F. 1998. The cosmic microwave background spectrum: an analysis of observations. *astro-ph/9805123*.
- [75] Novikov I. D., Thorne K. S. 1973. In *Black Holes*. Eds C. De Witt, B. S. De Witt, New York: Gordon and Breach, 343.
- [76] O' Dea C. P. 1998. The compact steep-spectrum and gigahertz peaked-spectrum radio sources. *PASP* 110: 493532.
- [77] Padovani P. 2007. Gamma-ray emitting AGN and GLAST. *arXiv: 0704.0184v1*.
- [78] Padovani P., Giommi P. 1995. The connexion between X-ray and radio selected BL Lacertae objects. *Astrophysical Journal* 444, 567-581.
- [79] Page, L. A. 2000. The Wilkinson Microwave Anisotropy Probe. In *Freedman, W. L., Measuring and Modelling the Universe* (Cambridge: Cambridge University Press), p. 330.
- [80] Parma P., Murgia M., De Ruiter H. R., Fanti R. 1999. The lives of FRI radio galaxies. *astro-ph/9910254v1*.
- [81] Peacock J. A., 1999. *Cosmological Physics*. Cambridge University Press.
- [82] Peck A. B., Taylor G. B. 2002. New VLBA identifications of compact symmetric objects. *New Astronomy Reviews*, Volume 46, Issues 2-7, 295-298.
- [83] Peebles P. J. E. 1980. *The Large-Scale Structure of the Universe*. Princeton: Princeton University.
- [84] Peebles P. J. E. 1993. *Principles of physical cosmology*. Princeton: Princeton University Press.
- [85] Penzias A. A., Wilson R. W. 1965. A measurement of excess antenna temperature at 4080 Mc/s. *ApJ* 142, 419.



## BIBLIOGRAPHY

---

- [86] Phillips P. R. 1995. Calculation of the kinetic Sunyaev-Zeldovich effect from the Boltzmann equation. *ApJ* 455:419-20.
- [87] Planck Collaboration 2006. The scientific programme of Planck. European Space Agency.
- [88] Reber G. 1949. Galactic Radio Waves. *Sky and Telescope*, vol.8, p.139.
- [89] Rees M. J., Ostriker J. P. 1977. Cooling, dynamics and fragmentation of massive gas clouds - Clues to the masses and radii of galaxies and clusters. *MNRAS*, 179, 541.
- [90] Rephaeli Y. 1995. Comptonization of the cosmic microwave background: the Sunyaev-Zeldovich effect. *ARA&A* 33:541-80.
- [91] Reviglio P. M., Helfand D. J. 2009. Active Galaxies in the Sloan Digital Sky Survey III: from quasars to radio galaxies? [astro-ph/0904.0190v1](https://arxiv.org/abs/astro-ph/0904.0190v1).
- [92] Roll P. G., Wilkinson D. T. 1966. Cosmic background radiation at 3.2 cm- Support for cosmic black body radiation. *Phys. Rev. Lett.* 16, 405.
- [93] Rybicki G. B., Lightman A. P. 1979. Radiation processes in astrophysics. Wiley-Interscience, New York.
- [94] Scannapieco E., Thacker R. J., Couchman H. M. P. 2008. Measuring AGN feedback with the Sunyaev-Zeldovich effect. [arXiv: 0709.0952v1](https://arxiv.org/abs/0709.0952v1).
- [95] Scott D., White M. 1999. Implications of SCUBA observations for the Planck Surveyor. *Astron. Astrophys.*, 346, 1, 1999.
- [96] Sparke L. S., Gallagher III J. S. 2007. *Galaxies in the Universe: An introduction*. Second edition, Cambridge University Press.
- [97] Sehgal N., Bode P., Das S. et al. 2009. Simulations of the microwave sky. [arXiv: 0908.0540v2](https://arxiv.org/abs/0908.0540v2).
- [98] Shakura N. I., Sunyaev R. A. 1973. Black holes in binary systems. Observational appearance. *A & A*, 24, 337.

## BIBLIOGRAPHY

---

- [99] Shapiro S. L. 1973. Accretion onto black holes: the emergent radiation spectrum. *ApJ*, 180, 531.
- [100] Silk J., 1977. On the fragmentation of cosmic gas clouds. I - The formation of galaxies and the first generation of stars. *Ap J.*, 211, 638.
- [101] Smoot G. F. et al. 1992. Structure in the COBE differential microwave radiometer first year maps. *ApJ*, 396, L1-L5.
- [102] Soltan A. 1982. Masses of quasars. *MNRAS*, 200, 115.
- [103] Somerville R. S., Primack J. R. 1999. Semi-analytic modelling of galaxy formation: the local Universe. *MNRAS*, 310, 1087.
- [104] Springel V. 2005. The cosmological simulation code GADGET-2. *MNRAS*, 364, 1105.
- [105] Springel V., Di Matteo T., Hernquist L. 2005. Modelling feedback from stars and black holes in galaxy mergers. *MNRAS*, 361, 776.
- [106] Springel V., White S. D. M., Jenkins A. et al. 2005. Simulations of the formation, evolution and clustering of galaxies and quasars. *Nature*, 435, 629.
- [107] Springel V., White S. D. M., Jenkins A. et al. 2005. Simulating the joint evolution of quasars, galaxies and their large-scale distribution. *astro-ph/0504097v2*.
- [108] Springel V., White S. D. M., Tormen G., Kauffmann G. 2001. Populating a cluster of galaxies-I. Results at  $z = 0$ . *MNRAS*, 328, 726.
- [109] Stanghellini C., ODea C. P., Dallacasa D., Cassaro P., Baum S. A., Fanti R., Fanti C. 2005. Extended emission around GPS radio sources. *A & A* 443: 891902.
- [110] Sunyaev R. A., Zeldovich Ya. B. 1970. The spectrum of primordial radiation, its distortions and their significance. *Comments Astrophys. Space Phys.* 2:66-74.
- [111] Sunyaev R. A., Zeldovich Ya. B. 1972. The observations of relic radiation as a test of the nature of X-ray radiation from the clusters of galaxies. *Comments Astrophys. Space Phys.* 4:173-78.

## BIBLIOGRAPHY

---

- [112] Sunyaev R. A., Zeldovich Ya. B. 1980. The velocity of clusters of galaxies relative to the microwave background - The possibility of its measurement. *MNRAS*, 190, 413.
- [113] Tegmark M., Efstathiou G. 1996. A method for subtracting foregrounds from multi-frequency CMB sky maps. *MNRAS*, 281, 1297.
- [114] Thorne K. S. 1974. Disk-Accretion onto a Black Hole. II. Evolution of the Hole. *ApJ*, 191, 507.
- [115] Trussoni E., Capetti A., Celotti A., Chiaberge M. 2002. SED of low power radio galaxies: test for FR I/ BL Lac unification. *Issues in Unification of AGNs*, ASP conference series, Vol. 258, 177.
- [116] Urry C. M., Padovani P. 1995. Unified schemes for radio-loud active galactic nuclei. *Publications of the Astronomical Society of the Pacific* 107, 803-845.
- [117] Volonteri M., Sikora M., Lasota J. P. 2007. Black-Hole Spin and Galactic Morphology. *astro-ph/0706.3900*, 706.
- [118] Waddington I., Dunlop J. S., Peacock J. A., Windhorst R. A. 2001. The LBDS Hercules sample of mJy radio sources at 1.4 GHz - II. Redshift distribution, radio luminosity function, and the high-redshift cut-off. *MNRAS*, 328, 882.
- [119] Wang J. M., Chen Y. M., Ho L. C., McLure R. J. 2006. Evidence for rapidly spinning black holes in quasars. *ApJ*, 642, L111.
- [120] White M., Majumdar S. 2004. Point sources in the context of future SZ surveys. *Astrophysical Journal*. 602: 565570.
- [121] White S. D. M., Frenk C.S. 1991. Galaxy formation through hierarchical clustering. *Astrophysical Journal*, 379, 52.
- [122] White S. D. M., Rees M. J. 1978. Core condensation in heavy halos - A two-stage theory for galaxy formation and clustering. *MNRAS*, 183, 341.

## BIBLIOGRAPHY

---

- [123] Wilkes B. J., Hooper E. J., McLeod K. K., Elvis M. S., Impey C. D., Lonsdale C. J., Malkan M. A., McDowell J. C. 1999. The far-infrared continuum of quasars. *astro-ph/9902084v1*.
- [124] Willott C. J., Rawlings S., Blundell K. M., Lacy M., Eales S. A. 2000. The radio luminosity function from the low-frequency 3CRR, 6CE & 7CRS complete samples. *astro-ph/0010419v1*.
- [125] Wilman R. J., Miller L., Jarvis M. J., Mauch T., Levrier F., Abdallah F. B., Rawlings S., Klöckner H. R., Obreschkow D., Olteanu D., Young S. 2008. A semi-empirical simulation of the extragalactic radio continuum sky for next generation radio telescopes. *MNRAS*. Press. p 291. arXiv: *astro-ph/0305591*.
- [126] Worrall D. M., 2008. The X-ray jets of active galaxies. arXiv: 0812.3401v1.
- [127] Wright E. L. et al. 1992. Interpretation of the CMBR anisotropy detected by the COBE differential microwave radiometer. *ApJ*, 396, L7-L12.
- [128] Wright E. L. 2004. Theoretical overview of cosmic microwave background anisotropy. in W. L. Freedman. *Measuring and modeling the Universe*. Carnegie Observatories Astrophysics Series. Cambridge University.
- [129] Xu G. 1995. A new parallel N-body gravity solver: TPM. *Astrophys. J. Suppl.* 98, 355-366.
- [130] Yates M. G., Miller L., Peacock J. A. 1989. The cluster environments of powerful, high-redshift radio galaxies. *MNRAS*, 240, 129.
- [131] Yoshida N., Stoehr F., Springel V., White S. D. M. 2002. Gas cooling in simulations of the formation of the galaxy population. *MNRAS*, 335, 762.
- [132] Yu Q., Lu Y. 2008. Toward precise constraints on the growth of massive black holes. *ApJ*, 689, 732.
- [133] Yu Q., Tremaine S. 2002. Observational constraints on growth of massive black holes. *MNRAS*, 335, 965.

# Appendix A

## Spectral distribution of the scattered CMB

We use the Kompaneets equation to describe the rate of change of the number of photons scattered by a hot electron gas assuming a Maxwellian distribution in the non relativistic approximation. This equation is a Fokker-Planck approximation of the kinetic equation given by (see Peebles (1993) [84] for the derivations):

$$\frac{\partial n}{\partial t} = \frac{kT}{mc} \frac{\sigma_T n_e}{x^2} \frac{\partial}{\partial x} \left[ x^4 \left( \frac{T_e}{T} \frac{\partial n}{\partial x} + n + n^2 \right) \right] \quad (\text{A.1})$$

where  $\sigma_T$  is the Thomson cross section ( $h\nu \ll mc^2$ ),  $n_e$  the density of electrons,  $T_e$  the electrons temperature and  $x = \frac{h\nu}{kT}$  the nondimensional frequency.  $k$  is the Boltzmann constant and  $T$  the temperature of the photons. Since  $T_e \gg T$  (hot electrons) we can neglect the second and third terms in the parenthesis. Then we obtain

$$\frac{\partial n}{\partial t} = \frac{kT}{mc} \frac{\sigma_T n_e}{x^2} \frac{\partial}{\partial x} \left[ x^4 \left( \frac{T_e}{T} \frac{\partial n}{\partial x} \right) \right]. \quad (\text{A.2})$$

The expression of the occupation number of a Planckian photon radiation is (Rephaeli (1995) [90]):

$$n_p(x) = \frac{1}{e^x - 1}. \quad (\text{A.3})$$

If the scattering of the incident radiation is weak we can obtain an approximate solution of the equation (A.2) by substituting (A.3) on the right-hand side of the equation. The

## Spectral distribution of the scattered CMB

---

expression of the intensity of radiation is given by:

$$I = i_o x^3 n \quad (\text{A.4})$$

where  $i_o = 2 \frac{(kT_o)^3}{(hc)^2}$ . The spectral intensity change is obtained by integrating (A.2) along the path length through the cluster:

$$\Delta I = i_o y g(x) \quad (\text{A.5})$$

where

$$g(x) = \frac{x^4 e^x}{(e^x - 1)^2} \left[ \frac{x(e^x + 1)}{e^x - 1} - 4 \right] \quad (\text{A.6})$$

is the spectral form of the thermal SZ effect and

$$y = \int \left( \frac{kT_e}{mc^2} \right) n_e \sigma_T dl \quad (\text{A.7})$$

the *Comptonization parameter* which characterises the spatial dependence of the effect. The function  $g(x) = 0$  at  $x_o = \frac{h\nu_o}{kT} = 3.83$  or at the frequency  $\nu_o \simeq 218$  GHz if we assume  $T_o = 2.726$  K (COBE/FIRAS, Mather et al. (1994) [67]). The temperature change caused by the scattering is given by

$$\Delta T = \left[ \frac{x(e^x + 1)}{e^x - 1} - 4 \right] T_o y. \quad (\text{A.8})$$

For the Rayleigh-Jeans (R-J) part of the spectrum  $x \ll 1$ . Hence

$$\frac{\Delta I}{I_o} \simeq \frac{\Delta T}{T_o} \quad (\text{A.9})$$

$$\simeq -2 \left( 1 + \frac{x}{2} \right) y \quad (\text{A.10})$$

$$\frac{\Delta T}{T_o} \simeq -2 \left( 1 - \frac{x^2}{4} \right) y \quad (\text{A.11})$$

to second order in  $x$  (Rephaeli (1995) [90]).

# Appendix B

## Table of temperature fluctuations and fluxes of radio sources

**Table B.1:** *Temperature fluctuations and fluxes caused by BL Lacs low luminosity blazars at redshift  $z = 0.10$  at 145 GHz, 220 GHz and 270 GHz. The clusters virial masses shown here are for  $M_{\text{vir}} \geq 2 \times 10^{14} h^{-1} M_{\odot}$  and with radio sources temperature fluctuations greater than  $0.1 \mu\text{K}$ .*

$M_{\text{vir}} (10^{14} h^{-1} M_{\odot})$	$T_{145\text{GHz}} (\mu\text{K})$	$S_{145\text{GHz}} (\text{mJy})$	$T_{220\text{GHz}}$	$S_{220\text{GHz}}$	$T_{270\text{GHz}}$	$S_{270\text{GHz}}$
2.038	1.7	0.16	3.5	0.14	4.5	0.14
2.044	8.3	0.78	17.2	0.71	21.9	0.67
2.052	2.5	0.23	5.2	0.21	6.6	0.20
2.060	0.1	0.01	0.3	0.01	0.3	0.01
2.065	0.3	0.03	0.6	0.02	0.8	0.02
2.068	1.6	0.15	3.4	0.14	4.3	0.13
2.074	6.9	0.65	14.3	0.59	18.3	0.56
2.089	0.6	0.06	0.1	0.00	0.1	0.00
2.094	0.1	0.01	0.3	0.01	0.3	0.01
2.094	1.0	0.10	0.3	0.01	0.3	0.01
2.097	4.7	0.44	9.8	0.40	12.4	0.38
2.099	16.3	1.54	33.9	1.39	43.2	1.32
2.100	30.6	2.89	63.7	2.61	81.2	2.48
2.104	9.4	0.89	19.6	0.81	25.0	0.76
2.106	4.4	0.42	9.2	0.38	11.7	0.36
2.106	3.2	0.30	9.2	0.38	11.7	0.36
2.109	20.3	1.92	0.1	0.00	0.1	0.00
2.110	0.4	0.04	0.8	0.03	1.0	0.03
2.112	0.2	0.02	0.1	0.00	0.1	0.00
2.115	15.1	1.42	31.4	1.29	40.0	1.22
2.125	1.4	0.14	3.0	0.12	3.8	0.12
2.132	4.9	0.46	10.2	0.42	13.0	0.40
2.143	0.4	0.04	0.9	0.04	1.1	0.03

Table of temperature fluctuations and fluxes of radio sources

Table B.1 – continued.

$M_{\text{vir}}$ ( $10^{14}h^{-1}M_{\odot}$ )	$T_{145\text{GHz}}$ ( $\mu\text{K}$ )	$S_{145\text{GHz}}$ (mJy)	$T_{220\text{GHz}}$	$S_{220\text{GHz}}$	$T_{270\text{GHz}}$	$S_{270\text{GHz}}$
2.156	0.2	0.02	0.5	0.02	0.6	0.02
2.163	0.1	0.01	0.2	0.01	0.3	0.01
2.171	2.9	0.27	6.0	0.24	7.6	0.23
2.173	0.7	0.07	1.5	0.06	1.9	0.06
2.174	6.9	0.65	1.5	0.06	1.9	0.06
2.208	8.6	0.82	18.0	0.74	22.9	0.70
2.210	12.8	1.21	26.7	1.10	34.1	1.04
2.212	4.3	0.41	9.0	0.37	11.5	0.35
2.214	0.1	0.01	0.2	0.01	0.3	0.01
2.214	0.3	0.03	0.2	0.01	0.3	0.01
2.228	0.2	0.02	0.2	0.01	0.5	0.01
2.228	0.1	0.01	0.27	0.01	0.5	0.01
2.229	0.5	0.05	1.1	0.04	1.4	0.04
2.232	4.8	0.45	9.9	0.41	12.7	0.39
2.248	0.2	0.02	0.5	0.02	0.6	0.02
2.253	0.3	0.03	0.6	0.02	0.8	0.02
2.295	5.6	0.53	11.6	0.48	14.8	0.45
2.300	0.1	0.01	0.3	0.01	0.4	0.01
2.306	5.5	0.52	11.4	0.47	14.6	0.44
2.319	2.0	0.18	4.1	0.17	5.2	0.16
2.322	3.2	0.30	6.7	0.28	8.6	0.26
2.329	0.1	0.01	0.3	0.01	0.3	0.01
2.335	0.6	0.05	1.2	0.05	1.5	0.05
2.345	4.1	0.39	8.6	0.35	10.9	0.33
2.348	1.1	0.11	2.4	0.10	3.0	0.09
2.362	3.0	0.28	6.2	0.25	7.9	0.24
2.368	6.4	0.60	13.2	0.54	16.9	0.51
2.382	0.1	0.01	0.2	0.01	0.3	0.01
2.383	13.4	1.26	27.8	1.14	35.4	1.08
2.386	0.2	0.01	0.3	0.01	0.4	0.01
2.387	1.2	0.12	0.1	0.01	0.2	0.01
2.394	0.5	0.05	1.1	0.04	1.4	0.04
2.395	0.3	0.03	0.6	0.02	0.7	0.02
2.403	25.9	2.45	53.9	2.21	68.7	2.10
2.415	0.5	0.05	1.0	0.04	1.3	0.04
2.417	2.1	0.20	4.4	0.18	5.6	0.17
2.418	0.1	0.01	0.3	0.01	0.3	0.01
2.420	24.9	2.35	51.9	2.13	66.1	2.01
2.436	0.8	0.07	1.6	0.07	2.0	0.06
2.439	4.2	0.40	8.8	0.36	11.3	0.34
2.439	0.1	0.01	8.8	0.36	11.3	0.34
2.445	7.0	0.66	14.6	0.60	18.6	0.57
2.465	26.4	2.50	55.0	2.26	70.2	2.14
2.468	5.5	0.52	0.2	0.01	0.2	0.01
2.469	15.0	1.41	31.2	1.28	39.7	1.21
2.488	0.6	0.06	1.3	0.05	1.7	0.05



Table of temperature fluctuations and fluxes of radio sources

Table B.1 – continued.

$M_{\text{vir}}$ ( $10^{14}h^{-1}M_{\odot}$ )	$T_{145\text{GHz}}$ ( $\mu\text{K}$ )	$S_{145\text{GHz}}$ (mJy)	$T_{220\text{GHz}}$	$S_{220\text{GHz}}$	$T_{270\text{GHz}}$	$S_{270\text{GHz}}$
2.497	11.8	1.11	24.6	1.01	31.3	0.95
2.497	0.1	0.01	24.6	1.01	31.3	0.95
2.503	0.2	0.02	0.4	0.02	0.5	0.01
2.504	2.0	0.19	4.1	0.17	5.3	0.16
2.528	30.2	2.86	62.9	2.58	80.2	2.45
2.536	3.5	0.33	7.3	0.30	9.3	0.28
2.539	5.2	0.49	10.8	0.44	13.7	0.42
2.554	0.3	0.03	0.6	0.02	0.8	0.02
2.556	11.2	1.06	23.4	0.96	29.8	0.91
2.563	2.7	0.25	5.5	0.23	7.1	0.22
2.566	0.2	0.02	0.4	0.01	0.5	0.01
2.578	7.1	0.67	14.8	0.61	18.9	0.58
2.589	1.4	0.13	2.9	0.12	3.7	0.11
2.603	2.1	0.20	4.5	0.18	5.7	0.17
2.627	2.3	0.22	4.9	0.20	6.2	0.19
2.627	0.2	0.01	4.9	0.20	6.2	0.19
2.634	2.5	0.24	5.2	0.21	6.7	0.20
2.662	3.1	0.29	6.4	0.26	8.1	0.25
2.663	5.2	0.49	10.9	0.45	13.9	0.42
2.672	4.3	0.41	9.0	0.37	11.4	0.35
2.672	4.7	0.45	9.0	0.37	11.4	0.35
2.681	12.4	1.17	25.8	1.06	32.9	1.00
2.685	1.9	0.18	3.9	0.16	4.9	0.15
2.692	4.2	0.40	8.7	0.36	11.1	0.34
2.703	17.7	1.67	36.8	1.51	46.9	1.43
2.709	6.1	0.58	12.8	0.52	16.3	0.50
2.710	2.6	0.24	12.8	0.52	16.3	0.50
2.713	0.7	0.06	1.4	0.06	1.8	0.05
2.714	2.6	0.25	1.4	0.06	1.8	0.05
2.717	0.2	0.02	0.3	0.01	0.4	0.01
2.735	0.7	0.07	1.5	0.06	1.9	0.06
2.740	8.6	0.81	17.9	0.73	22.8	0.70
2.745	0.1	0.01	0.3	0.01	0.3	0.01
2.752	0.1	0.01	0.3	0.01	0.4	0.01
2.757	5.8	0.55	0.2	0.01	0.2	0.00
2.766	2.1	0.20	4.5	0.18	5.7	0.17
2.789	0.3	0.03	0.7	0.03	0.9	0.03
2.790	4.9	0.46	10.2	0.42	13.0	0.40
2.794	0.1	0.01	0.3	0.01	0.4	0.01
2.796	6.4	0.61	13.4	0.55	17.1	0.52
2.829	0.2	0.01	0.3	0.01	0.4	0.01
2.830	1.1	0.10	2.3	0.09	2.9	0.09
2.836	3.2	0.30	6.7	0.27	8.5	0.26
2.838	14.8	1.40	30.9	1.27	39.3	1.20
2.883	0.6	0.06	1.3	0.05	1.6	0.05
2.920	1.7	0.16	3.6	0.15	4.5	0.14

Table of temperature fluctuations and fluxes of radio sources

Table B.1 – continued.

$M_{\text{vir}}$ ( $10^{14}h^{-1}M_{\odot}$ )	$T_{145\text{GHz}}$ ( $\mu\text{K}$ )	$S_{145\text{GHz}}$ (mJy)	$T_{220\text{GHz}}$	$S_{220\text{GHz}}$	$T_{270\text{GHz}}$	$S_{270\text{GHz}}$
2.922	0.1	0.01	0.3	0.01	0.3	0.01
2.931	2.6	0.24	5.3	0.22	6.8	0.21
2.955	0.6	0.06	1.3	0.05	1.6	0.05
2.955	8.8	0.83	1.3	0.05	1.6	0.05
2.963	3.5	0.33	7.2	0.29	9.2	0.28
2.971	6.3	0.59	13.0	0.53	16.6	0.51
2.972	1.2	0.12	13.0	0.53	16.6	0.51
2.989	2.7	0.26	5.7	0.23	7.2	0.22
3.006	7.5	0.71	15.6	0.64	19.9	0.61
3.010	0.5	0.05	1.0	0.04	1.3	0.04
3.013	4.5	0.43	9.4	0.39	12.0	0.37
3.062	2.1	0.19	4.3	0.18	5.4	0.17
3.107	3.3	0.31	6.8	0.28	8.7	0.27
3.127	28.5	2.69	59.4	2.43	75.7	2.31
3.143	0.2	0.02	0.4	0.02	0.5	0.02
3.151	0.1	0.01	0.3	0.01	0.3	0.01
3.156	6.3	0.60	13.2	0.54	16.8	0.51
3.160	4.6	0.43	9.5	0.39	12.2	0.37
3.169	0.8	0.07	1.6	0.07	2.0	0.06
3.170	1.2	0.12	1.6	0.07	2.0	0.06
3.171	0.8	0.08	1.7	0.07	2.1	0.06
3.173	0.5	0.05	1.1	0.05	1.4	0.04
3.177	8.1	0.76	16.8	0.69	21.5	0.65
3.182	15.8	1.49	32.9	1.35	41.9	1.28
3.186	0.1	0.01	0.3	0.01	0.4	0.01
3.193	7.6	0.71	15.7	0.65	20.1	0.61
3.204	4.3	0.41	9.0	0.37	11.5	0.35
3.263	0.1	0.01	0.3	0.01	0.4	0.01
3.289	1.2	0.11	2.4	0.10	3.1	0.09
3.317	9.7	0.92	20.3	0.83	25.9	0.79
3.351	0.4	0.04	0.8	0.03	1.0	0.03
3.367	9.1	0.86	18.9	0.78	24.1	0.74
3.378	0.1	0.01	0.3	0.01	0.4	0.01
3.400	114.6	10.82	238.4	9.78	303.9	9.26
3.421	10.1	0.95	20.9	0.86	26.7	0.81
3.423	7.7	0.73	16.1	0.66	20.5	0.62
3.440	4.7	0.44	9.7	0.40	12.4	0.38
3.455	5.6	0.53	11.7	0.48	14.9	0.45
3.481	0.2	0.02	0.5	0.02	0.6	0.02
3.489	4.4	0.42	9.3	0.38	11.8	0.36
3.513	0.1	0.01	0.2	0.01	0.3	0.01
3.524	0.3	0.03	0.7	0.03	0.9	0.03
3.539	4.5	0.42	9.3	0.38	11.9	0.36
3.544	7.5	0.71	15.6	0.64	19.9	0.61
3.547	5.5	0.52	11.4	0.47	14.6	0.44
3.558	0.7	0.06	1.4	0.06	1.8	0.05

Table of temperature fluctuations and fluxes of radio sources

Table B.1 – continued.

$M_{\text{vir}}$ ( $10^{14}h^{-1}M_{\odot}$ )	$T_{145\text{GHz}}$ ( $\mu\text{K}$ )	$S_{145\text{GHz}}$ (mJy)	$T_{220\text{GHz}}$	$S_{220\text{GHz}}$	$T_{270\text{GHz}}$	$S_{270\text{GHz}}$
3.561	0.5	0.04	0.9	0.04	1.2	0.04
3.613	0.4	0.04	0.9	0.04	1.2	0.04
3.642	1.7	0.16	3.5	0.14	4.5	0.14
3.650	0.4	0.04	0.8	0.03	1.0	0.03
3.680	0.1	0.01	0.2	0.01	0.3	0.01
3.696	67.0	6.33	139.5	5.72	177.7	5.42
3.704	8.0	0.76	16.6	0.68	21.2	0.65
3.767	9.1	0.86	18.9	0.78	24.1	0.74
3.776	14.6	1.38	30.4	1.25	38.8	1.18
3.845	0.2	0.01	0.3	0.01	0.4	0.01
3.887	10.9	1.03	22.7	0.93	29.07	0.88
3.889	7.8	0.73	16.1	0.66	20.6	0.63
3.914	8.4	0.80	17.6	0.72	22.4	0.68
3.923	8.3	0.78	17.2	0.71	21.9	0.67
3.937	2.3	0.21	4.7	0.19	6.0	0.18
3.938	0.2	0.01	0.3	0.01	0.4	0.01
3.942	7.4	0.70	15.4	0.63	19.6	0.60
3.950	0.1	0.01	0.3	0.01	0.3	0.01
3.950	4.7	0.44	0.3	0.01	0.3	0.01
3.969	0.9	0.09	1.9	0.08	2.5	0.08
3.995	0.2	0.02	0.5	0.02	0.6	0.02
4.005	17.9	1.69	37.2	1.53	47.4	1.45
4.021	5.8	0.55	12.0	0.49	15.3	0.47
4.031	77.8	7.34	161.9	6.64	206.3	6.29
4.033	19.9	1.88	41.5	1.70	52.9	1.61
4.095	30.8	2.90	64.0	2.63	81.6	2.49
4.101	1.2	0.12	2.6	0.11	3.3	0.10
4.147	2.6	0.24	5.4	0.22	6.9	0.21
4.165	0.7	0.07	1.5	0.06	1.9	0.06
4.217	1.2	0.12	2.5	0.10	3.2	0.10
4.220	0.1	0.01	0.3	0.01	0.3	0.01
4.232	31.6	2.98	65.7	2.70	83.8	2.55
4.243	6.2	0.58	12.9	0.53	16.4	0.50
4.268	54.2	5.12	112.9	4.63	143.9	4.39
4.294	5.7	0.54	11.8	0.49	15.1	0.46
4.316	2.6	0.25	5.5	0.22	7.0	0.21
4.336	0.2	0.02	0.5	0.02	0.6	0.02
4.343	11.5	1.08	23.9	0.98	30.4	0.93
4.368	31.8	3.01	66.2	2.72	84.4	2.57
4.386	0.5	0.04	0.9	0.04	1.2	0.04
4.390	20.1	1.90	41.8	1.71	53.2	1.62
4.401	0.1	0.01	0.2	0.01	0.3	0.01
4.452	2.1	0.20	4.5	0.18	5.7	0.17
4.495	14.8	1.40	30.8	1.26	39.2	1.19
4.532	15.8	1.49	32.9	1.35	41.9	1.28
4.550	0.5	0.05	1.1	0.05	1.4	0.04

Table of temperature fluctuations and fluxes of radio sources

Table B.1 – continued.

$M_{\text{vir}}$ ( $10^{14}h^{-1}M_{\odot}$ )	$T_{145\text{GHz}}$ ( $\mu\text{K}$ )	$S_{145\text{GHz}}$ (mJy)	$T_{220\text{GHz}}$	$S_{220\text{GHz}}$	$T_{270\text{GHz}}$	$S_{270\text{GHz}}$
4.558	12.6	1.19	26.3	1.08	33.5	1.02
4.733	1.0	0.09	2.0	0.08	2.6	0.08
4.935	30.8	2.91	64.1	2.63	81.7	2.49
4.961	0.9	0.09	2.0	0.08	2.5	0.08
5.012	51.2	4.84	106.6	4.37	135.9	4.14
5.106	1.4	0.13	3.0	0.12	3.8	0.11
5.311	0.3	0.03	0.6	0.03	0.8	0.02
5.406	0.5	0.04	1.0	0.04	1.3	0.04
5.411	8.7	0.82	18.1	0.74	23.0	0.70
5.476	22.0	2.08	45.8	1.88	58.3	1.78
5.481	16.4	1.55	34.2	1.40	43.6	1.33
5.768	1.4	0.13	2.9	0.12	3.7	0.11
5.939	1.4	0.13	3.0	0.12	3.8	0.11
5.985	13.1	1.23	27.2	1.12	34.7	1.06
6.077	3.1	0.29	6.4	0.26	8.1	0.25
6.237	9.5	0.90	19.8	0.81	25.2	0.77
6.314	138.4	13.07	288.1	11.81	367.1	11.19
6.447	18.9	1.79	39.4	1.62	50.2	1.53
6.684	1.3	0.13	2.8	0.11	3.5	0.11
6.707	1.1	0.10	2.3	0.09	2.9	0.09
6.725	1.0	0.09	2.1	0.08	2.6	0.08
6.742	2.7	0.25	5.6	0.23	7.1	0.22
6.882	0.6	0.05	1.1	0.05	1.5	0.04
6.902	25.9	2.45	54.0	2.21	68.8	2.10
8.092	1.4	0.13	2.8	0.12	3.6	0.11
8.268	16.1	1.52	33.4	1.37	42.6	1.30
8.664	11.8	1.12	24.6	1.01	31.4	0.96
8.973	17.0	1.61	35.4	1.45	45.2	1.38
9.010	0.9	0.09	2.0	0.08	2.5	0.08
9.104	12.1	1.14	25.2	1.03	32.1	0.98
9.988	174.2	16.45	362.6	14.87	462.1	14.09
10.229	118.3	11.17	246.3	10.10	313.8	9.57
10.254	54.0	5.10	112.3	4.60	143.1	4.36
11.197	3.0	0.28	6.2	0.25	7.8	0.24
12.697	48.9	4.61	101.7	4.17	129.6	3.95
21.141	159.3	15.04	331.4	13.59	422.4	12.88